Behavior of some metallic impurities in germanium : investigation by transient spectroscopy methods - Deep Level Transient Spectroscopy-Minority Carrier Transient Spectroscopy - Laplace Deep Level Transient Spectroscopy

Yana Gurimskaya

UNIVERSITÉ DE STRASBOURG

N° d'ordre : 76849

École Doctorale Mathématiques, Sciences de l'Information et de l'Ingénieur

UdS – INSA – ENGEES

THÈSE

présentée pour obtenir le grade de

Docteur de l'Université de Strasbourg

Discipline: Electronique, micro-électronique et photonique

Spécialité : Physique des semi-conducteurs

par

Yana Gurimskaya

COMPORTEMENT DE QUELQUES IMPURETES METALLIQUES DANS LE GERMANIUM: UNE ETUDE PAR LES TECHNIQUES CAPACITIVES DLTS-MCTS-LAPLACE DLTS

Soutenue publiquement le 31 Mai 2012

Membres du jury

Directeur de thèse:	M. Abdelmadjid Mesli, Directeur de recherche, IM2NP, CNRS
Co-Directeur de thèse:	M. Daniel Mathiot, Professeur, InESS, UdS
Rapporteur externe:	Mme. Gabrielle Regula, Associate professor, IM2NP
Rapporteur externe:	M. Georges Bremond, Professeur, INL, INSA Lyon
Examinateur:	M. Thomas Heiser, Professeur, InESS, UdS
Examinateur:	M. Piotr Kruszewski, Docteur, IFPAN Poland, IM2NP

InESS **UMR – 7163**

"Research is the art of seeing what everyone else has seen,
and doing what no-one else has done."

Albert Einstein

ACKNOWLEDGMENTS

First of all, I would like to express my sincere gratitude to Abdelmadjid Mesli, my scientific advisor, for his continuous support, guidance, patience and optimism during my doctoral research and to Daniel Mathiot, co-director of the thesis, for his guidance, invaluable help, time and passion during thesis writing and of course for providing me with the financial support.

I would like to express my gratitude to Professors Georges Bremond, Thomas Heiser, Gabriella Regula and Doctor Piotr Kruszewski for acting as referees for my thesis work.

I am extremely grateful to Professor Leszek Dobaczewski from the Institute of Physics, Polish Academy of Sciences, for his abundant and invaluable help and extraordinary support within our fruitful collaboration.

Also I would like to thank Sébastien Schmitt, Nicolas Zimmermann and Jérémy Bartringer for their technical assistance. My sincere appreciation goes also to Yann Le Gall for his work on the implantation processes.

Lastly, I express my sincere gratitude to my dear parents, sister and niece, to my wonderful beloved husband and to my magnificent friends, who supported me during these years and who made my life brighter. Мама и папа, спасибо вам огромное за безграничную любовь и терпение! Я достигла многого, благодаря вашей заботе и поддержке.

Yana Gurimskaya

May 2012

COMPORTEMENT DE QUELQUES IMPURETES METALLIQUES DANS LE GERMANIUM: UNE ETUDE PAR LES TECHNIQUES CAPACITIVES DLTS-MCTS-LAPLACE DLTS

(Résumé de la thèse en français)

INTRODUCTION ET OBJECTIFS

Les niveaux profonds introduits par les défauts et les impuretés dans les semi-conducteurs, même à l'état de trace, ont des conséquences néfastes au bon fonctionnement des composants, comme par exemple l'augmentation des courants de fuite ou la détérioration des durées de vie des porteurs minoritaires. En conséquence, la connaissance des propriétés électroniques associées, position du niveau dans le gap (E_T) et section de capture (σ), est primordiale pour l'optimisation des composants [1].

Les impuretés métalliques font partie des contaminants majeurs des semi-conducteurs de la colonne IV (Si, Ge et SiGe). Ce sont des diffuseurs rapides, très réactifs, qui introduisent des niveaux multiples dans la bande interdite et affectent donc fortement le comportement des dispositifs. Cependant les données existantes sur les propriétés des impuretés métalliques dans le germanium, souvent dispersées, sont loin d'être aussi complètes que dans le cas du silicium, ce qui nécessite de les réexaminer de près [2-12].

À une température donnée, la solubilité et la diffusivité des impuretés métalliques sont supérieures dans le germanium que dans le silicium [13, 14]. Il est généralement admis que dans le germanium les métaux de transitions sont des impuretés substitutionnelles, agissant comme des accepteurs multiples introduisant plusieurs niveaux dans la bande interdite, en accord avec un simple modèle de liaisons de valence. Ceci constitue une différence fondamentale avec le cas du silicium où ces impuretés métalliques sont essentiellement interstielles.

Le germanium est de plus en considéré comme une alternative au silicium pour des composants avancés, ce qui a suscité ces dernières années un net regain d'intérêt pour l'étude des défauts et des impuretés dans ce matériau, à l'aide de la DLTS et ses dérivées, techniques plus élaborées que celles utilisées dans les études initiales (effet Hall ou mesure de durée de vie).

Dans ce travail, nous nous focalisons sur l'étude de Fe, Cr, Ni, et Au. Des études détaillées par DLTS, MCTS et Laplace DLTS sont effectuées pour réexaminer les propriétés électroniques des états introduits par ces quatre métaux de transition dans le germanium. Parmi les paramètres étudiés, on peut citer en particulier les barrières de capture des porteurs, les vraies sections efficaces de capture des

porteurs majoritaires (déterminées directement par la méthode de variation du pulse de remplissage) ainsi que la possible existence d'un effet Pool-Frenkel (en lien avec la détermination de l'état de charge du niveau concerné). Ceci permet de déterminer avec précision la position exacte des niveaux dans la bande interdite. Par ailleurs nous avons obtenu de nouvelles informations sur le comportement microscopiques de ces impuretés, comme la mise en évidence de leur interaction avec l'hydrogène conduisant à des défauts complexes introduisant d'autres niveaux dans la bande interdite. Dans le cas de Fe, à cause de la très grande proximité des deux niveaux introduits, nous soulevons également la question de la possibilité d'un comportement "U-négatif".

DETAILS EXPERIMENTAUX

Afin d'étudier les niveaux introduits par Fe, Cr ou Ni, des substrats de germanium (*Umicore*) de type *n*, dopés à l'antimoine à une concentration de l'ordre de 10^{15} cm^{-3}, ont été implantés en face arrière avec l'impureté désirée à une dose de $5\times10^{14}cm^{-2}$. Les échantillons ont ensuite été recuits à 500°C pendant 15 minutes et refroidis lentement. Afin de réaliser des contacts Schottky semi-transparents, les échantillons sont tout d'abord nettoyés par gravure chimique dans un mélange HNO_3:*HF* (3:1) pendant 5 à 10 s. Des plots d'or d'épaisseur 150 Å sont ensuite évaporés en face avant, et le contact face arrière est effectué par une évaporation d'un film de 500 Å d'aluminium.

Les contaminations par Au ont été effectuées par simple diffusion thermique. Un film de 1000 Å d'or est évaporé sur la face arrière du substrat de Ge, puis l'échantillon est recuit pendant 6 heures à 700°C dans un tube de quartz, sous une pression de 300 mbar d'argon. Les diodes Schottky sont finalement réalisées comme décrit précédemment.

Par ailleurs nous avons pu étudier avec succès le comportement de Ni dans Ge de type p, grâce à des diodes mésa n^+p gracieusement fournies par l'Institute of Physics and Astronomy de l'Université de Aarhus. Nous avons réalisé le contact face arrière par évaporation d'or (500 Å).

Finalement les niveaux introduits dans la bande interdite ont été étudiés par DLTS (Deep Level Transient Spectoscopy), MCTS (Minority Carrier Transient Spectroscopy) et Laplace DLTS.

RESULTATS ET DISCUSSION

Des spectres distincts de DLTS, Laplace DLTS et MCTS ont pu être obtenus dans Ge de type n pour chacun des métaux de transition (TM) étudié (Fe, Cr, Ni ou Au),

tandis que des spectres dans Ge de type p ont également pu être obtenus dans le cas de Ni. Les principaux résultats pour Fe et Cr ont fait l'objet d'une publication [15].

Les spectres de DLTS conventionnelle obtenus dans *n*-Ge contaminé avec Fe, Ni ou Cr, conformément aux derniers résultats de la littérature [2-12], montrent clairement une asymétrie du pic principal, ce qui suggère l'existence d'un deuxième niveau, très proche du niveau principal, se manifestant par un épaulement de ce pic du côté des basses températures.

Nous avons donc pratiqué des analyses par Laplace DLTS [16], technique offrant une bien meilleure résolution. Les résultats, montrés sur les **Figures S.1 (a)**, **(b)** et **(c)**, mettent clairement en évidence l'existence de 2 niveaux distincts, notés TM-E1 et TMX-E.

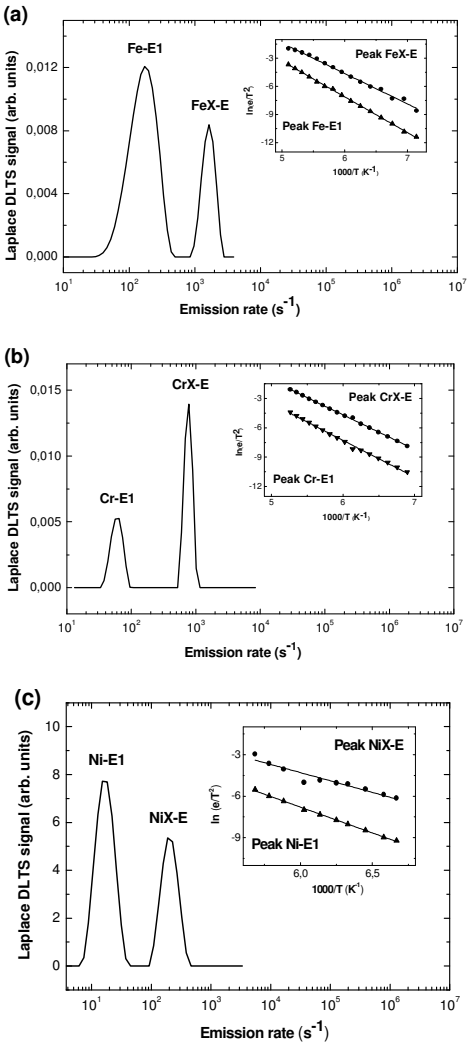

Fig. S.1. Spectres de Laplace DLTS enregistrés dans *n*-Ge contaminés avec Fe (a), Cr (b) ou Ni (c). Les paramètres d'analyse sont les suivant : t_F = 200 µs pour tous les, (a) séquence de pulse (−4V, −2V) et T = 180K; (b) séquence de pulse (−4V, −1.5V) et T = 175K; (c) séquence de pulse (−5V, −2V) et T = 180K. L'encart montre les signatures des niveaux TM-E1 and TMX-E.

Les encarts de ces figures montrent les tracés d'Arrhenius des vitesses d'émission des porteurs pour chacun des niveaux, après correction usuelle du facteur T^2. Les enthalpies d'ionisation correspondantes (E_{na},), ainsi que les sections de capture (σ) et si possible les barrières de capture (E_σ) sont reportées dans la **Table S.1**.

Nos résultats établissent sans doute possible que le pic principal (TM-E1) observé par DLTS dans tous ces échantillons est associé à une configuration caractérisée par l'existence d'une barrière pour la capture des porteurs majoritaires. Cette propriété, généralement associée à un centre répulsif, est cohérente avec ce qui est généralement admis depuis les travaux pionniers de *Woodbury and Tyler* [9, 12] dans les années 50 et rediscuté plus récemment par *Clauws et al.* [17] : dans Ge, les métaux de transitions sont stables en site substitutionnel, induisant des états accepteurs car ils ne sont pas tétravalents. D'après ce modèle simple, Fe et Ni, ayant une couche électronique externe comportant seulement 2 électrons (configuration $4s^2$), sont des accepteurs doubles, introduisant donc deux niveaux dans la bande interdite, correspondant aux transitions $Fe^{0/-}$ ou $Ni^{0/-}$ (1er niveau accepteur) et $Fe^{-/2-}$ou $Ni^{-/2-}$ (2ème niveau accepteur). Si ces états de charges sont distribués normalement, le niveau double accepteur est situé au dessus du niveau simple accepteur, et on s'attend à le trouver dans la moitié supérieure de la bande interdite. Le pic TM-E1 correspond donc très probablement à ce 2ème niveau accepteur pour Fe et Ni.

La même analyse est valable pour Cr. Cependant, pour cette impureté, la configuration électronique de la couche externe est $4s^1$ (un seul électron de valence), et on s'attend donc à un caractère triplement accepteur, avec 3 niveaux dans la bande interdite du germanium. Le pic de DLTS de la **Figure S.1(b)** correspond à la transition $Cr^{2-/3-}$.

La dépendance en température des sections de capture des pièges associés aux différents niveaux TM-E1 est montrée sur la **Figure S.2** pour chacune des impuretés. On trouve ainsi pour Fe une énergie de barrière E_σ = 0,043 eV et une section de capture extrapolée à température infinie σ_∞ = 5,0×10^{-15} cm^2, E_σ et σ_∞ =4,1×10^{-15} cm^2 pour Ni, et E_σ et σ_∞ = 4,6×10^{-15} cm^2 pour Cr.

Les niveaux TM-E1 associés aux 3 métaux Fe, Ni et Cr ont donc des faibles sections efficaces de capture des porteurs majoritaires, thermiquement activées. Nous considérons que cette observation est l'indication d'un mécanisme de capture, assistée par phonons multiples, au dessus d'une barrière répulsive, comme attendu pour la capture d'un électron par un centre chargé négativement [18], en parfaite cohérence avec le caractère accepteur multiple de ces niveaux. L'attribution de ces pièges à des niveaux accepteurs est également confortée par l'absence d'effet du champ électrique sur la position des niveaux TM-E1.

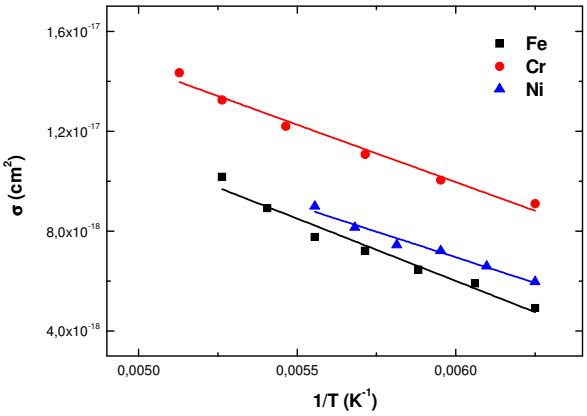

Fig. S.2. Dépendance en température des section de capture des niveaux associés à Fe, Ni et Cr dans *n*-Ge.

Le cas de Au est loin d'être aussi clair. Fondamentalement, l'or est un défaut amphotère avec deux niveaux couplés, un accepteur triple plus un niveau donneur profond. Les pics principaux Au-E1 et Au-E2 observés par DLTS (**Figure S.3**) sont associés à l'or substitutionnel.

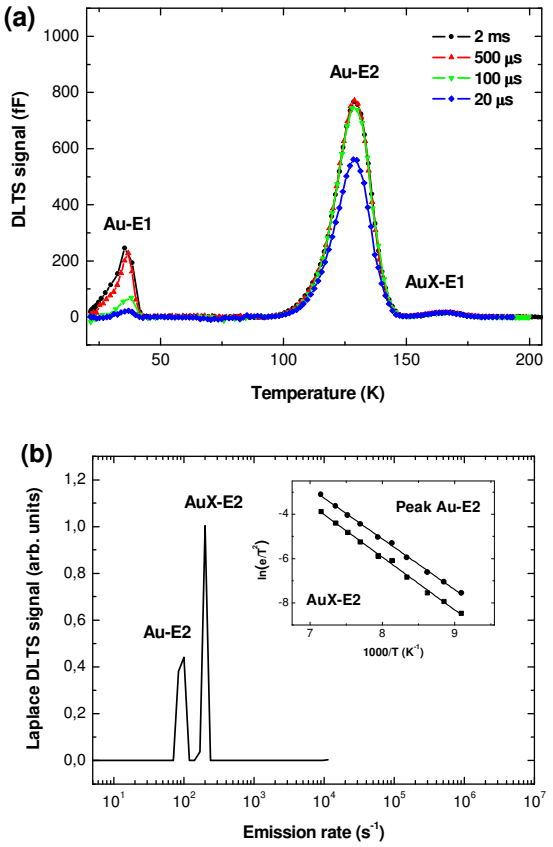

Fig. S.3. Spectre de DLTS (a) et de Laplace DLTS (b) des échantillons *n*-Ge contaminés avec Au. Les paramètres d'analyse sont les suivant : t_F = 200 µs, séquence de pulse (−5V, −2V), (a) avec une fenêtre de 100 s^{-1} et (b) à T = 130K. L'encart montre la signature des niveaux Au-E2 and AuX-E2.

Les spectres DLTS montrent également 2 pics de moindre importance, non directement corrélés aux pics principaux. Le pic AuX-E1 apparaissant vers 165 K sur le spectre DLTS pourrait faire penser à un niveau cité dans la littérature, associé au cuivre ($Cu_s^{(3-/2-)}$) [19], mais sa forte section efficace de capture n'est pas cohérente avec un centre répulsif, ce qui nous incite à rejeter cette hypothèse. Nous l'attribuons à un possible complexe AuSb. Ce point nécessitera de plus amples recherches dans des travaux futurs pour être élucidé. Le pic AuX-E2, apparaissant comme un épaulement du pic DLTS Au-E2, et clairement isolé sur le spectre de Lapalce DLTS, pourrait être associé à un complexe avec l'hydrogène, comme les pics TMX-E observés pour Fe, Ni et Cr.

Les enthalpies d'ionisation correspondant de ces pièges TMX-E (épaulements des pics principaux pour Fe, Ni et Cr dans *n*-Ge) sont également reportés dans la **Table S.1**.

Nous avons pu établir que le facteur clé contrôlant la formation de ces pics est associé au mode de préparation des diodes Schottky nécessaires à la caractérisation DLTS. En effet la préparation de surface inclut nécessairement un traitement à l'aide d'un mélange d'acide nitrique et fluorhydrique, de composition *3:1* dans notre cas. Les variations dans la composition exacte de ce mélange de gravure pourraient expliquer les différences observées dans la littérature. Le point important est que ces solutions contiennent toutes des ions d'hydrogène. L'étape de gravure est donc très probablement responsable d'une injection non négligeable d'hydrogène atomique dans les premiers microns des échantillons, c'est à dire dans la zone analysée par DLTS. L'hydrogène injecté peut ensuite très probablement se lier aux atomes métalliques pour former des défauts complexes introduisant de nouveaux niveaux dans la bande interdite.

Afin de tester cette hypothèse, nous avons effectué un test particulier sur des échantillons saturés en impureté métallique (recuit long de 5 heures à 500°C après l'implantation ionique) pour garantir une concentration constante (profil plat) de métal. Ces échantillons ont été délibérément traités plus longuement (2 minutes) dans la solution HNO_3:HF pour forcer l'injection d'hydrogène, avant la réalisation finale des diodes Schottky. Le spectre DLTS correspondant (dans le cas de Cr) est montré sur la **Figure S.4 (a)**, qui met clairement en évidence une très forte augmentation du pic CrX-E1, comparé à la procédure habituelle. La **Figure S.4 (b)** montre le spectre obtenu sur le même échantillon ayant subit un recuit supplémentaire (450°C, 30 min.) pendant lequel l'hydrogène exodiffuse de l'échantillon. La disparition du pic CrX-E1 confirme son lien avec l'hydrogène.

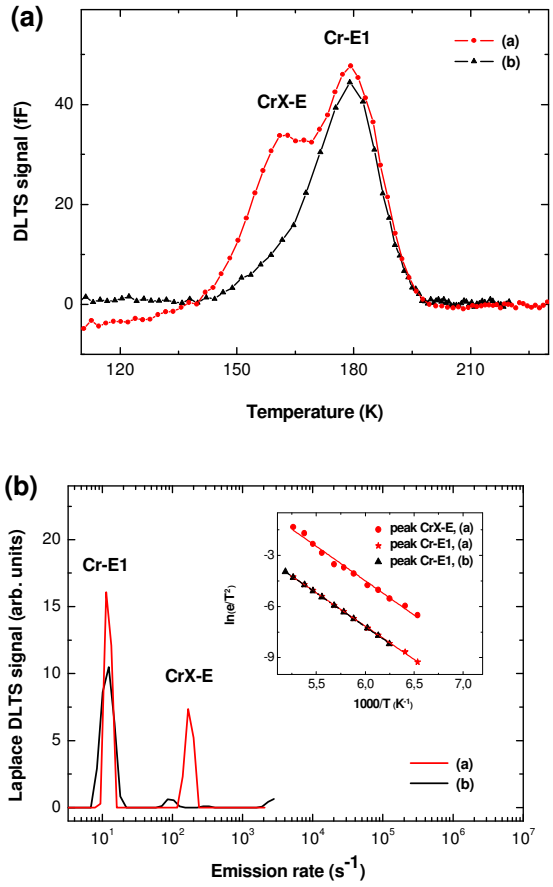

Fig. S.4. Spectres DLTS (a) et Laplace DLTS (b) des échanitllons n-Ge samples contaminés avec Cr et immergés pendant 2 min dans HNO_3 , avant (rouge) et après (noir) un recuit supplémentaire de 30 min à 450°C. les spectres on été enregistrés avec une fenêtre 100 s^{-1} et une durée d'impulsion de t_F = 200 µs avec une séquence de pulse de (-10V;-5V).

Par ailleurs, les spectres DLTS obtenus après les mêmes expériences d'injection d'hydrogène dans du germanium pur (non contaminé avec une impureté métallique) ne montrent aucun pic, ce qui renforce notre hypothèse que les niveaux TMX-E (pour Fe, Ni et Cr) et AuX-E2 (pour l'or) sont associés à des défauts complexes impliquant le métal et l'hydrogène. Le défaut le plus simple est une paire TM-H, mais des défauts plus complexes impliquant plusieurs atomes d'hydrogène (TM-H_n) ne peuvent pas être exclus, comme c'est le cas dans le silicium [20].

Les valeurs "intermédiaires" que nous obtenons pour les sections de capture de ces centres TMX-E (reportées dans la **Table S.2**) laissent penser que la capture du trou a lieu sur un défaut neutre., ce qui est cohérent avec l'image simple de la neutralisation des liaisons par l'hydrogène. Les complexes introduiraient donc un niveau donneur agissant comme un piège à trous, correspondant à la transition TMX-$E^{0/+}$.

Nous avons étudié les niveaux introduits dans la moitié inférieure de la bande interdite du germanium par la technique MCTS (Minority Carrier Transient Spectroscopy) à l'aide des mêmes contacts Schottky sur *n*-Ge. Pour ces analyses, la

polarisation inverse de la diode est maintenue constante et des impulsions lumineuses d'énergie supérieure à la bande interdite sont utilisées pour générer optiquement les porteurs minoritaires dans la zone de déplétion. Dans ce travail ces impulsions ont été effectuées à l'aide d'une diode laser émettant à 850 nm, à des puissances variables jusqu'à 200 mW.

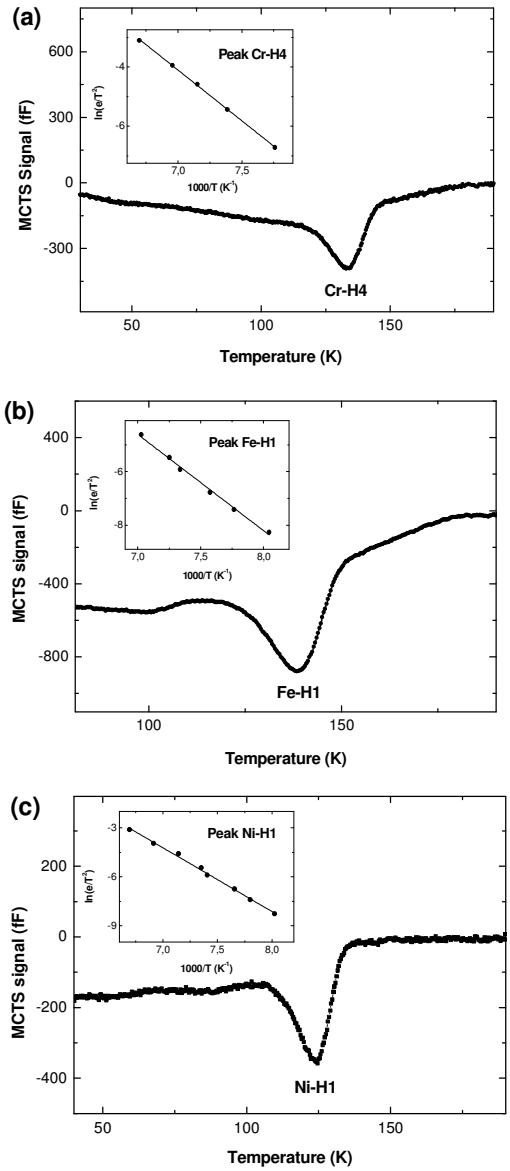

Fig.S.5. Spectres MCTS d'échantillons *n*-Ge contaminés (a) Cr, (b) Fe, ou (c) Ni. Les mesures ont été effectuées à une polarisation de -5V, durée de pulse optique de 5 ms et une fenêtre de 80 s^{-1}. L'encart montre la signature du niveau TM-H1.

La **Figure S.5** montre les spectres MCTS caractéristiques obtenus pour des échantillons de *n*-Ge contaminés avec Fe **(a)**, Ni **(b)** et Cr **(c)** respectivement. Pour chaque impureté, un seul pic significatif émerge d'un fond continu correspondant à une distribution d'états. Ce pic correspond à un piège à trou, désigné par TM-H1. Les enthalpies d'ionisation correspondantes sont données dans la **Table S.1**. Par contre

il n'a pas été possible de mesurer directement les valeurs des sections de capture des porteurs minoritaires par la méthode de la variation de longueur des impulsions. Leurs valeurs sont estimées à quelques 10^{13} cm^2 ou plus. De telles valeurs sont une indication du fait que les trous sont probablement capturés par des défauts chargés négativement [18].

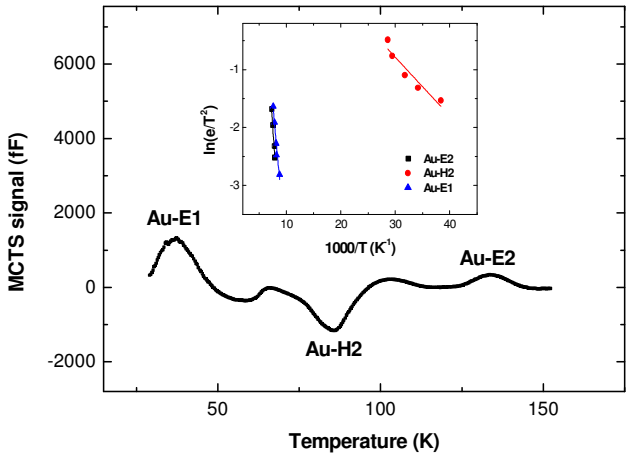

Fig. S.6. Spectres MCTS d'échantillons *n*-Ge contaminés avec Au. Les mesures ont été effectuées à une polarisation de -5V, durée de pulse optique de 5 ms et une fenêtre de 200 s^{-1}. L'encart montre la signature des différents niveaux.

Comme on peut le constater sur le **Figure S.6**, deux types de pièges sont mis en évidence par MCTS dans le cas de l'or : un piège à porteurs minoritaires (Au-H1) et deux pièges à porteurs majoritaires (Au-E1 et Au-E2). Ce comportement inhabituel pourrait s'expliquer en supposant que le niveau accepteur de l'or ($Au^{-/0}$), situé proche du milieu de la bande interdite, se comporte comme un centre de génération - recombinaison interagissant à la fois avec la bande de conduction et la bande de valence, lui conférant un caractère dual de piège à électron et de piège à trous [21].

Nous avons également mis en évidence, pour la première fois, que les vitesses d'émission des niveaux Fe-H1 et Ni-H1 dépendent fortement du champ électrique. La **Figure S.7** montre la variation de l'énergie d'activation apparente en fonction de du champ électrique. Conformément au modèle de Poole-Frenkel, attendu pour un centre attractif, on observe une variation linéaire avec la racine carrée du champ [22]. L'existence de l'effet Poole-Frenkel est une forte indication que les niveaux Fe-H1 et Ni-H1 sont dus à des défauts attractifs pour les trous (états accepteurs), ce qui est totalement cohérent avec leur très forte section de captures. Les valeurs corrigées (extrapolées à champ nul) des énergies d'ionisation ΔH sont reportées dans la **Table S.1**.

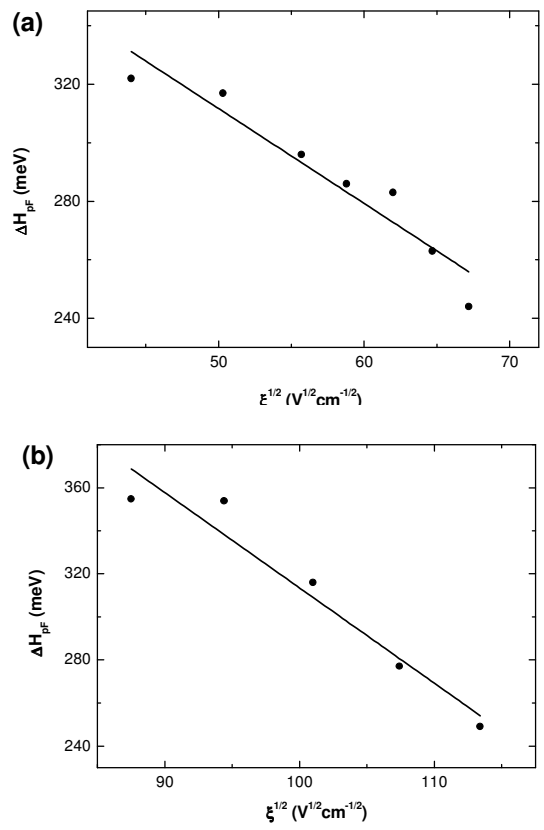

Fig.S.7. Mise en évidence de l'effet Poole-Frenkel (diminution de l'enthalpie d'ionisation en fonction du champ électrique) observé par MCTS pour les niveaux associés à Fe (a) et Ni (b).

Grâce à l'utilisation des diodes mésa n^+p, nous avons pu, pour la première fois, utiliser la technique de Laplace DLTS pour sonder la moitié inférieure de la bande interdite dans des échantillons de p-Ge contaminés par Ni. Le résultat est présenté sur la **Figure S.8** qui met en évidence un piège à tous (Ni-H1*) dont les éléments de signature sont reportés dans **Table S.1**.

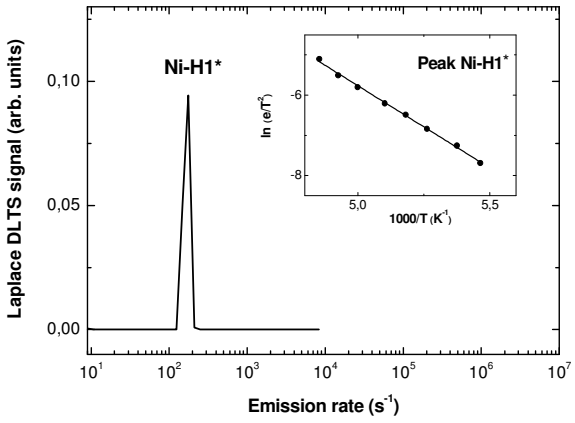

Fig.S.8. Spectre de Laplace DLTS pour un échantillon de p-Ge. Les paramètres d'analyse sont : t_F = 200 µs, polarisation (−5V, −2V) et T = 200 K. L'encart montre la signature du piège à trou Ni-H1*.

CONCLUSION

Dans ce travail nous avons étudié quelques particularités associées aux espèces métalliques Fe, Cr, Ni et Au dans le germanium de type *n* à l'aide de la DLTS conventionnelle et de la Laplace DLTS. L'utilisation de barrières Schottky limite l'étude aux niveaux introduits dans la moitié supérieure de la bande interdite.

L'utilisation de jonctions n^+p pour étudier la moitié inférieure de la bande interdite (utilisées pourtant avec succès pour l'étude des défauts d'irradiation) s'est avérée inefficace pour la plupart des impuretés métalliques étudiées. Nous pensons que ceci est du à une détérioration de la jonction pendant le recuit de 500°C permettant la contamination métallique. Des diodes exploitables ont néanmoins pu être obtenues dans le cas de Ni, ce qui a permis, pour la première fois, de caractériser des pièges à porteurs minoritaires à l'aide de la technique très sensible de Laplace DLTS. Pour les autres métaux, le problème a été contourné par l'utilisation d'excitations optiques pour générer les porteurs minoritaires dans les diodes Schottky sur n-Ge, nous permettant l'étude de la moitié inférieure de la bande interdite.

Nos travaux confirment les résultats majeurs déjà obtenus par d'autres auteurs, tout en apportant des précisions sur les paramètres fondamentaux contrôlant l'émission et la capture des porteurs. Par ailleurs, nous avons pu mettre en évidence de nouvelles informations concernant le comportement microscopique des impuretés étudiées (Fe, Ni, Cr et Au), comme leur interaction avec l'hydrogène donnant lieu à la formation de défauts complexes, induisant des défauts profonds passé inaperçus jusqu'à présent.

Dans le cas particulier de l'or, nous avons mis en évidence de nouveaux niveaux que nous attribuons tentativement à des complexes AuH_n et AuSb. Par ailleurs l'origine de l'observation concomitante par MCTS de pièges à majoritaires et à minoritaires reste à être élucidée par des études complémentaires.

Pour ce qui concerne le fer, la très faible différence d'énergie entre les 2 niveaux observés pose la question d'un possible caractère "U-négatif" : même si les niveaux, bien que très proches, sont dans l'ordre normal aux températures cryogéniques de mesure DLTS, on peut légitimement s'interroger sur une possible inversion aux températures proche de l'ambiante, si chacun des niveaux reste "épinglé" au bord de bande avec lequel il interagit.

En conclusion, la synthèse de tous nos résultats, comparés à ceux de la littérature, est donnée sur la **Figure S.9**.

Table S.1:

Synthèse des propriétés des différents niveaux associés aux impuretés métalliques dans Ge.

Level label	K_T ($s^{-1}K^{-2}$)	$\Delta E_{na/pa}$ (eV)	$\sigma_{na/pa}$ (cm^2)	σ_∞ (cm^2)	E_σ(eV)	$\Delta S_n/k_B$	ΔH_n(eV)
Fe-E1	7.1×10^{6}	0.327±0.002	$(2.3\pm0.4)\times10^{-16}$	$(4.98\pm0.39)\times10^{-15}$	0.043	3.08	0.284
Cr-E1	4.2×10^{6}	0.325±0.005	$(1.4\pm0.5)\times10^{-16}$	$(4.59\pm0.36)\times10^{-15}$	0.046	3.49	0.279
Ni-E1	5.5×10^{6}	0.321±0.005	$(1.8\pm0.6)\times10^{-16}$	$(4.09\pm0.32)\times10^{-15}$	0.035	3.12	0.286
Au-E1	3.3×10^{5}	0.047±0.002	$(1.1\pm0.9)\times10^{-17}$	$(3.37\pm0.54)\times10^{-14}$	0.019	8.03	0.028
Au-E2	1.3×10^{6}	0.212±0.001	$(4.2\pm1.6)\times10^{-15}$	$(2.99\pm0.34)\times10^{-13}$	0.033	4.27	0.179
CrX-E	1.5×10^{7}	0.305±0.002	$(4.7\pm0.7)\times10^{-16}$				
FeX-E	4.1×10^{6}	0.287±0.006	$(1.3\pm0.6)\times10^{-16}$				
NiX-E	1.4×10^{5}	0.233±0.009	$(1.2\pm2.2)\times10^{-17}$				
AuX-E1	3.1×10^{8}	0.359±0.006	$(1.0\pm0.5)\times10^{-14}$				
AuX-E2	6.5×10^{5}	0.169±0.004	$(2.1\pm0.6)\times10^{-17}$				
Ni- H1*	2.4×10^{6}	0.354±0.006	$(2.1\pm0.4)\times10^{-15}$				
Cr-H4	4.2×10^{8}	0.294±0.008	$(3.7\pm0.3)\times10^{-12}$				
Fe-H1	2.8×10^{8}	0.310±0.008	$(3.3\pm0.3)\times10^{-12}$				0.374
Ni-H1	3.6×10^{9}	0.336±0.020	$(4.2\pm0.8)\times10^{-12}$				0.378
Au- H2	1.3×10^{7}	0.280±0.005	$(1.1\pm0.8)\times10^{-13}$				

Les niveaux TM-H sont des pièges à trou. Leurs caractéristiques relatives à la bande de valence.

Table S.2:

Level label	K_T ($s^{-1}K^{-2}$)	E_T (eV)	σ_{na} (cm^2)
Cr-E1 (annealed)	1.1×10^{7}	0.336±0.002	$(3.6\pm0.2)\times10^{-14}$
CrX-E1 (not annealed)	4.1×10^{8}	0.350±0.010	$(1.3\pm1.0)\times10^{-14}$
Cr-E1 (not annealed)	1.1×10^{7}	0.337±0.007	$(3.6\pm0.5)\times10^{-14}$

Signatures des niveaux associés aux complexes TM-H.

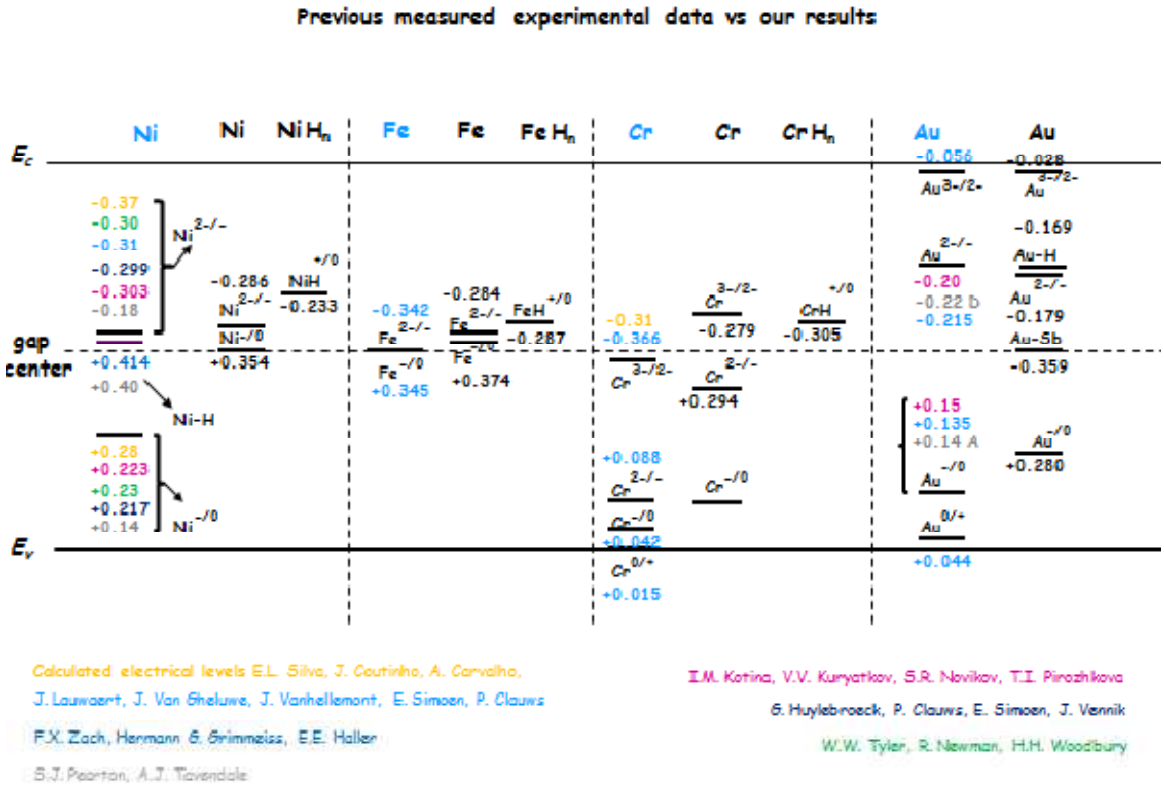

Fig. S.9. Paramètres et identification des pièges à électrons et à trou associés à Fe-, Cr-, Ni- et Au-dans Ge implanté [2-5, 7-10, 12, 17, 23-27].

BEHAVIOUR OF SOME METALLIC IMPURITIES IN GERMANIUM: INVESTIGATION BY TRANSIENT SPECTROSCOPY METHODS - DLTS, MCTS AND LAPLACE DLTS

(Thesis resume in English)

INTRODUCTION AND OBJECTIVES

Deep levels in semiconductors can generate leakage current and can operate as lifetime killers even at trace concentrations. Therefore the knowledge of electrical properties of deep levels like energy levels (E_T) and capture cross sections (σ) is very important [1].

Transition metals are among the most unwanted contaminants in the group IV semiconductors (Si, Ge and SiGe). They are fast diffusers and highly reactive, introducing deep levels in the band gap, affecting the life time of minority carriers and thereby the device yield. The collected data of the properties of metals in germanium are by far much less complete than in silicon, and still exhibit some scattering, requiring often a re-examination [2-12].

Fe, Cr, Ni and Au impurities are particular subject of this PhD thesis. The solubility and diffusivity of metals in Ge is higher at the same temperatures than in Si [13, 14]. A general picture, that emerged, is that transition metals in Ge predominantly form multiple-acceptor centres, introducing several deep levels in the band gap, which according to a simple valence bond model is in agreement with a preferential occurrence of the impurities on substitutional sites. This is in marked contrast with Si, where metallic impurities have been found to prefer interstitial sites.

Due to the perspective to apply germanium in advanced electronic devices, a renewed interest in the properties of defects and impurities in germanium has appeared in the last few years. Since the early studies by Hall effect and lifetime measurements, Deep Level Transient Spectroscopy (DLTS) and its variations have become the preferential technique to study deep level centres in semiconductors.

In this work we focus on Fe and Cr, Ni and Au in Ge and present extensive DLTS, MCTS and Laplace DLTS results to investigate the electronic properties of the multi-acceptor states, induced by these four transition metals. Among the studied parameters we may cite the barrier for carrier capture, the true majority carrier capture cross section directly measured by the variable pulse length method, the Poole-Frenkel effect related to the assignment of the charge states - all these parameters are important to locate the level positions in the band gap. New insight is revealed on the microscopic behavior of these two chemical species such as their

interactions with hydrogen giving rise to the generation of complex-related levels in the band gap. For the Fe case, the small difference in energy of its two levels raises the question as to the possibility of negative-U character.

EXPERIMENTAL DETAILS

To study the transition metal specific levels within the bandgap, Ge *n*-type crystal wafers supplied by *Umicore*, doped with Sb shallow donor at concentration of 10^{13} cm^{-3}, have been implanted with one of the transition metals - Fe, Cr and Ni. For each metal a dose of $5\times10^{14}cm^{-2}$ was used before the sample has received a 15 min post implantation thermal annealing at 500°C. Slow cooling followed before the samples were etched in HNO_3:HF (3:1) during 5-10 sec. Then as a last step, Au dots were evaporated (150 Å) on front side to form semi-transparent Schottky contacts; Al (500 Å) was evaporated on the back side to form ohmic contact.

Au-doped samples were prepared in the following way. Firstly, the 1000 Å layer of Au was evaporated on the back side of n-type Ge wafer. Annealing in a quartz tube under 300 mbar of Argon for about 6 hours at 700 °C was followed before usual etching and contact evaporation is realized as is described above. Average Au concentration, obtained by C-V measurements, is found to be equal 0.9×10^{14} cm^{-3}.

n^+p-mesa diodes were prepared in the Institute of Physics and Astronomy, at the University of Aarhus, Denmark. We have a success in mesa diode doped by Ni preparation. To form an ohmic contact Au layer was evaporated (500 Å) on the back side.

Deep-level transient spectroscopy (DLTS), minority carrier transient spectroscopy (MCTS) and Laplace DLTS techniques were used to investigate the band gap of germanium.

RESULTS AND DISCUSSION

Distinct DLTS, Laplace DLTS and MCTS spectra were observed in *n*-type samples implanted with one of the TMs – Fe, Cr, Ni or Au- and *p*-type Ge sample doped by Ni. Summary of the results for Fe and Cr may be found in Ref. [15].

Concerning Fe, Ni and Cr a careful analysis of the state-of-the-art [2-12] show a clear asymmetry in conventional DLTS spectra of Fe and Cr-implanted n-type Ge samples, suggesting the presence of a nearby level revealed as a shoulder on the low temperature side of the major peak.

Consequently we use Laplace DLTS method [16] which offers a more efficient resolution as mentioned above. The results evidence clearly two separated levels as shown on **Figures S.1 (a)**, **(b)** and **(c)**. The insets of the figures display the

Arrhenius plots of the emission rates, corrected by factor of T^2. The enthalpies of ionization E_{na}, the capture cross sections σ and whenever possible the barriers for capture E_σ are summarized in **Table S.1**.

There is a doubt that in all samples the major peaks TM-E1 are related to configurations characterized by a barrier for capture. This property, generally found for repulsive centres, is coherent with our above expectations, based on statements, already discussed by *Clauws et al.* [17] and pioneered by *Woodbury and Tyler* [9, 12] in the mid fifties, stating that in Ge metallic species stabilize in substitutional sites, inducing acceptor levels as they are not tetravalent. According to this simple model Fe and Ni with their $4s^2$ external shell introduces in the band gap a double acceptor ($Fe^{-/2-}$, $Ni^{-/2-}$) and a single acceptor ($Fe^{0/-}$, $Ni^{0/-}$). If these charge states distribute normally, the double acceptor state can be detected in the upper half of the band gap.

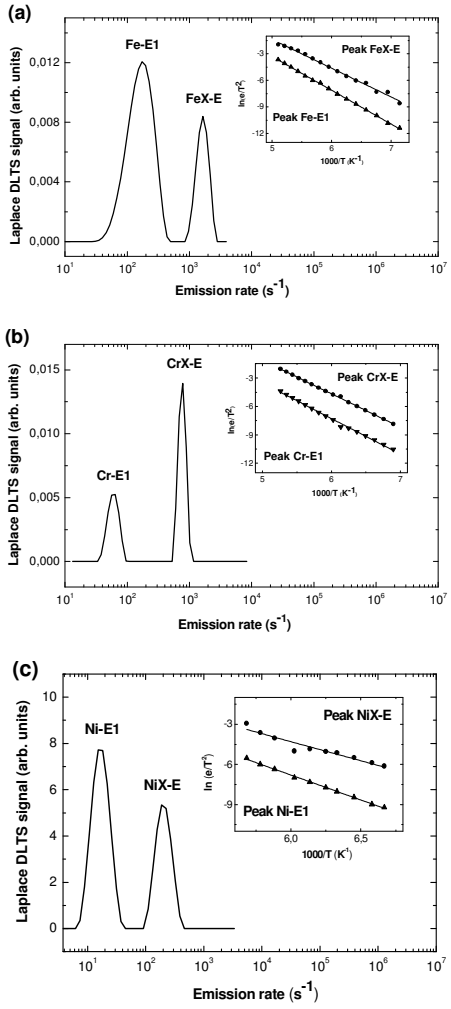

Fig. S.1. Laplace DLTS spectrum recorded in the Fe (a), Cr (b) and Ni (c) diffused *n*-type Ge sample. The analytical parameters are as follows: t_F = 200 µs for all spectra, (a) pulse sequence (−4V, −2V) and T = 180K; (b) pulse sequence (−4V, −1.5V) and T = 175K; (c) pulse sequence (−5V, −2V) and T = 180K. The inset shows the Arrhenius plots of the emission rates for levels labelled TM-E1 and TMX-E.

The same trend holds for Cr, except that the external shell of this metal has one single electron ($4s^1$). Therefore, a triple, double and single acceptor states are expected to show up in the Ge band gap. The DLTS signal (**Figure S.1(b)**) corresponds to the configuration $Cr^{2-/3-}$.

The quantitative determination of the capture cross sections for levels labelled TM-E1 and displayed in **Figure S.1** led to the following barriers for capture: $E_\sigma = 0.043\ eV$ with a capture cross section at infinite temperature of $\sigma_\infty = 5.0 \times 10^{-15}\text{cm}^2$ for Fe, $E_\sigma = 0.035\ eV$ and $\sigma_\infty = 4.1 \times 10^{-15}\text{cm}^2$ for Ni and $E_\sigma = 0.046\ eV$ with a capture cross section $\sigma_\infty = 4.6 \times 10^{-15}\text{cm}^2$ for Cr. The temperature dependent capture cross sections as a function of temperature are presented on the **Figure S.2**.

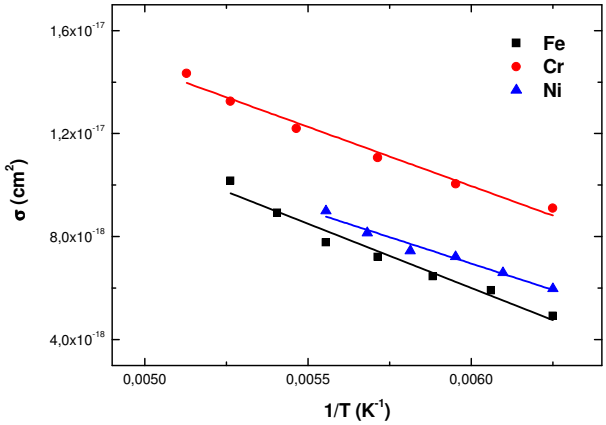

Fig. S.2. The temperature dependent capture cross sections of Fe, Ni and Cr diffused n-type Ge.

For mentioned metals the TM-E1 level corresponds with a low value of the electron capture cross section, which is thermally activated. This observation may be considered as an indication that we are dealing with multiphonon-assisted capture against a repulsive barrier, as would be the case for electron capture into a negative charge state of the defect [18]. These levels are attributed to the double acceptors in case of Fe and Ni and triple acceptor in case of Cr, so that electron capture occurs in the doubly negative or triply negative charge states, respectively. The assignment to acceptor levels is supported by the absence of an electric field enhanced shift of the TM-E1 levels.

In case of Au the situation is far from to be clear. Basically, gold is an amphoteric defect with two coupled levels, i.e. a triple acceptor with an additional deep donor level. The main bands Au-E1, Au-E2 (**Figure S.3**) belong to substitutional gold. Other observed levels seem to be produced by possible interaction of gold with other impurities forming the complexes with H, appearing as a shoulder in Au-E2 peak family, and with shallow Sb, appearing around 165 K in DLTS and Laplace DLTS measurements, labeled AuX-E2 and AuX-E1, respectively. These levels seem to be

uncorrelated with the main Au-related levels. Speaking of permanently observed AuX-E1level, we should mention the band, which has already been observed and referred in the literature, attributed to the $Cu_s^{(3-/2-)}$ [19]. But large capture cross section of AuX-E1 reject the possible presence of a repulsive center, such as Cu_s is. This point is deserving consideration in a further work.

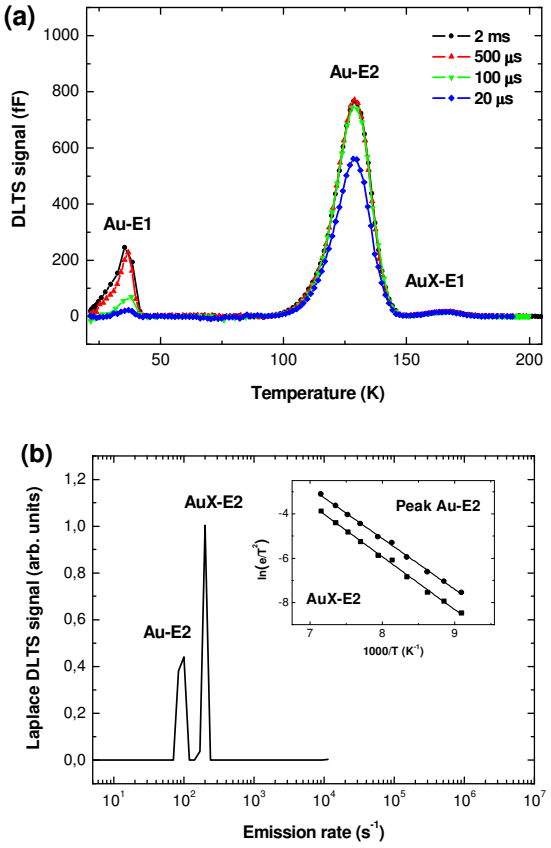

Fig. S.3. (a) DLTS and (b) Laplace DLTS spectrum recorded in the Au-doped *n*-type Ge sample. The analytical parameters are as follows: t_F = 200 µs, pulse sequence (−5V, −2V), (a) at a rate window of 100 s^{-1} and (b) at T = 130 K. The inset shows the Arrhenius plots of the emission rates for levels labelled Au-E2 and AuX-E2.

As to the shoulder-related peaks TMX-E, their enthalpies of ionization as extracted from the Arrhenius plots of the insets for Fe, Cr and Ni are also presented in **Table S.1**.

The key issue regarding the shoulders TMX-E in case of Fe-, Cr-, Ni-diffused *n*-type Ge samples, is related to the way the samples were prepared before their characterization. The chemical treatment cannot be avoided, so the difference between state-of-the-art and our results is related to the nature and composition of the chemical solutions, which all contain ionic hydrogen. Before evaporating the electrical contacts our samples were etched during a few seconds in a mixture of nitric and hydrofluoric acid, in the proportions *3:1*. Such a treatment is certainly

responsible for hydrogen injection into the first few microns forming the observation area. Hydrogen is expected to get bound with Fe, Ni, Au and Cr.

Figure S.4 displays two (a) DLTS and (b) Laplace DLTS spectra recorded on the Cr-contaminated samples before and after a significant annealing, following a dip during 2 min in the above mentioned chemical solution – *HNO_3:HF* – in the proportion *3:1*. Samples were annealed 5 hours at 500°C before hydrogen treatment to fulfil the requirement for a uniform diffusion of the metal after its implantation.

As can be seen from **Figure S.4** this H-related complex disappears after an annealing during 5 hours at 500°C, a temperature required to release and out diffuse hydrogen from the observation area.

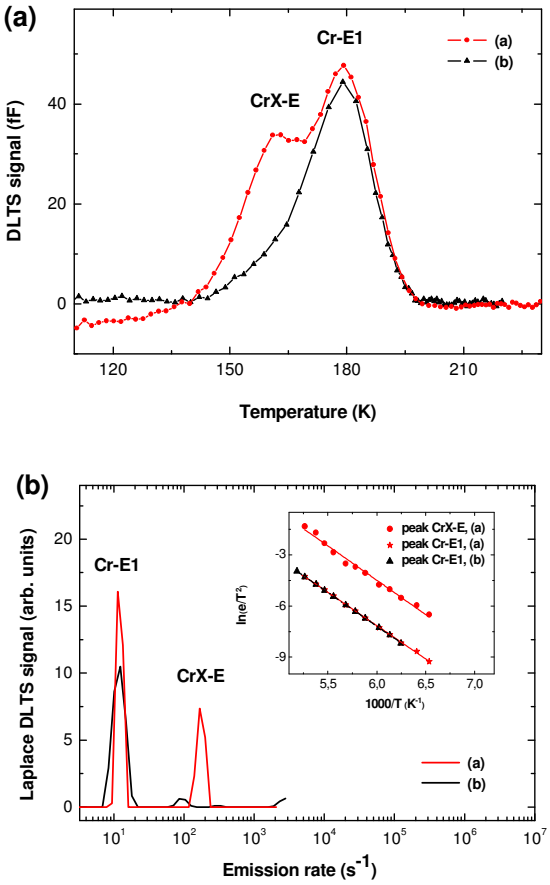

Fig. S.4. (a) DLTS and (b) Laplace DLTS spectra of Cr-contaminated n-type Ge samples, dipped during 2 min in *HNO_3* and (black) not annealed or (red) annealed 30 min at 450°C, recorded at a rate window of 100 s^{-1} with pulse duration t_F = 200 µs and the pulse sequence (-10V;-5V).

The simplest defect involving hydrogen could be the pairs TMH, where TM stands for the metal. However higher orders such as TM-H_n, where *n* used for the number of hydrogen atoms, involved in the complex cannot be excluded. Examples of such complex molecules are numerous in silicon [20]. We suggest that observed TM-H_n complexes are responsible for the donor action, emphasizing the active role hydrogen plays in complexing with other impurities in Ge. Such hydrogen-related

deep donor levels should capture holes into neutral charge state. Expected intermediate values for capture cross sections σ_n were found and are presented in **Table S.2**.

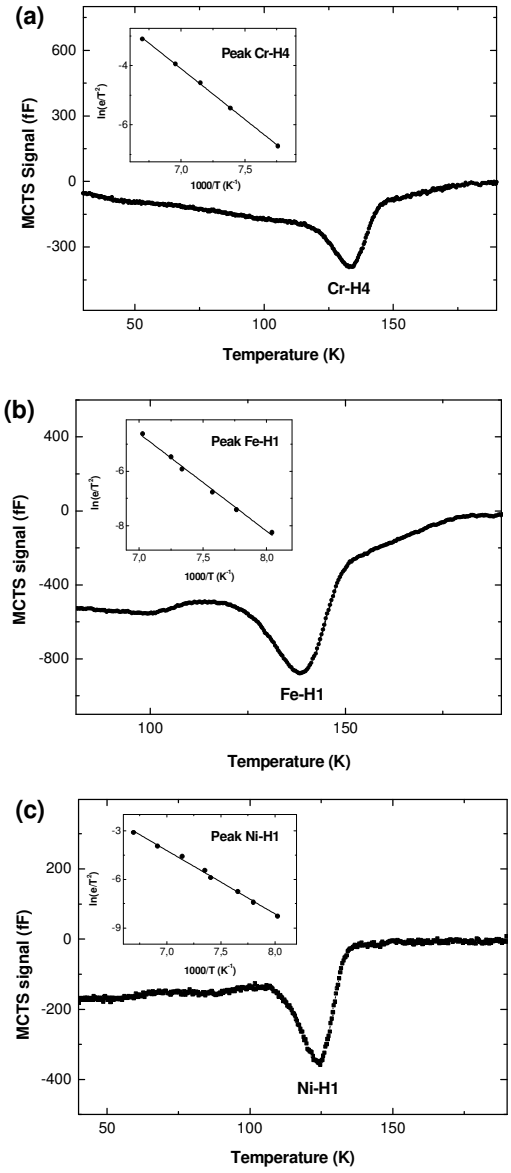

Fig.S.5. MCTS scan for (a) Cr-, (b) Fe- and (c) Ni –contaminated *n*-type Ge at -5V with an optical pulse duration of 5 ms and rate window of 80 s^{-1}. The inset displays the Arrhenius plot of the hole trap TM-H1.

It is also important to report that hydrogen alone in pure germanium treated in the same conditions does not show any hydrogen related DLTS signal. This strengthens the argument that the shoulders are complexes involving both hydrogen and the metallic species. Thus in this work a new insight is revealed on the microscopic behavior of the investigated chemical species through their unavoidable interactions with hydrogen giving rise to the generation of complex-related levels in the band gap. We suggest the presence of complexes formed by Fe, Cr, Ni (peak TMX-

E1 in DLTS and Laplace DLTS spectra) and Au (peak AuX-E2 in DLTS and Laplace DLTS spectra) impurities and hydrogen during the sample preparation.

For lower part of Ge bandgap investigation the Minority Carrier Transient Spectroscopy (MCTS) was applied to *n*-type Schottky barriers. In this procedure we keep the reverse bias constant and use above band gap light to generate optically the minority carriers in the depletion region. In the present work we use a laser diode emitting at 850 nm with a variable power up to 200 mW.

Figure S.5 displays a typical MCTS spectrum for **(a)** Fe-, **(b)** Ni- and **(c)** Cr-doped *n*-type Ge, showing a single level peaking above a continuum distribution of states. Light is absorbed exponentially from the surface. Under the experimental conditions given for **Figure S.5**, we obtained enthalpy of ionization for all impurities, listed in **Table S.1**.

The capture cross section of the hole traps labeled TM-H1 could not be measured by the pulse length method, so that values are estimated to be in order of 10^{13} cm^2 or higher. Such high cross sections indicate that the holes are probably captured into negative charge state of the defects [18].

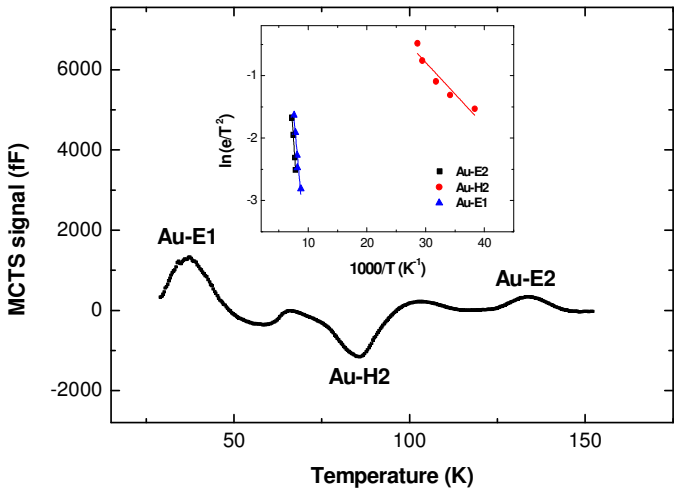

Fig. S.6. MCTS scan recorded in the Au-diffused sample at -5V with an optical pulse duration of 5 ms and rate window of 200 s^{-1}.

As can be seen from **Figure S.6**, in MCTS investigation two types of deep carrier traps can be observed – both minority (Au-H2) and majority (Au-E1 and Au-E2). This unusual phenomenon might be explained if we assume the gold acceptor level as a recombination-generation center, interacting with both the conduction and the valence bands. We cannot exclude the pinning of the acceptor level to the conduction band, thus the acceptor level $Au^{-/0}$, marked as Au-H2, being a midgap level, seem to interact simultaneously with both the conduction and valence band, which leads to presence of both electron and hole trap character in MCTS investigation [21].

For Fe-H1 and Ni-H1 levels show a distinct electric field enhanced emission, which was observed for the first time. In **Figure S.7** the field dependence of the apparent activation energy has been plotted according to a simple Poole-Frenkel model for attractive centers [22].

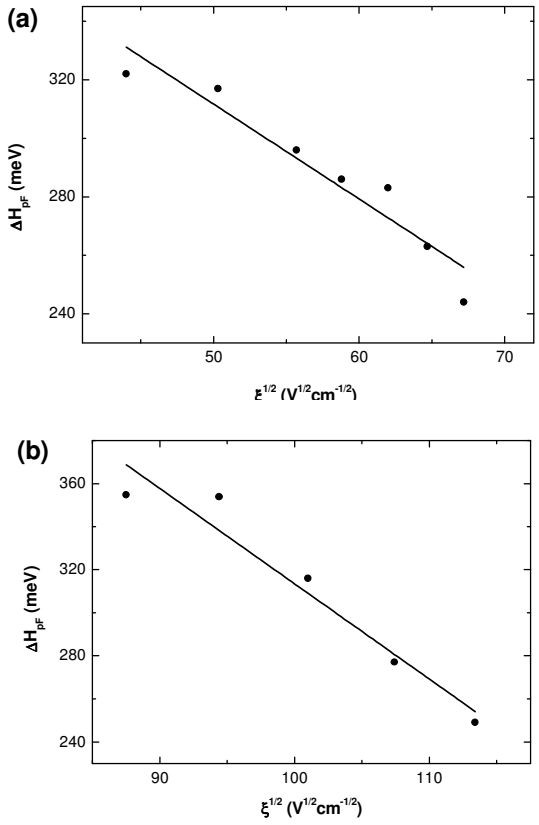

Fig.S.7. Poole-Frenkel effect observed in MCTS analysis of (a) Fe and (b) Ni-doped *p*-type Ge, showing the reduction of the enthalpy of ionization ΔH_{pF} as a function of $\xi^{1/2}$.

In this work we have studied the effect of the electric field on the hole emission from the single acceptor states of Fe and Ni impurity atom in *n*-type Ge. The experimental results (**Figure S.7**) indicate that Poole-Frenkel model can be considered as the mechanism for the electric-field-induced minority carrier emission from the single acceptor states of Fe and Ni centers in the range of electric fields from $2 \times 10^3\ V/cm$ to $1.3 \times 10^4\ V/cm$. Extrapolating of the apparent activation energy to zero field results in the corrected values of ΔH presented in **Table S.1**. Observed field enhancement of the hole emission is a strong indication that peaks Fe-H1 and Ni-H1 are due to the states attractive for holes, i.e. the acceptor states, which is also in agreement with high values of the capture cross sections.

The success in n^+p mesa diode preparation gives us possibility to investigate lower part of the bandgap of *p*-type Ge doped by Ni using Laplace DLTS method at the first time. Observed hole trap labeled as Ni-H1* is presented in **Figure S.8** with the corresponding signature listing in **Table S.1**.

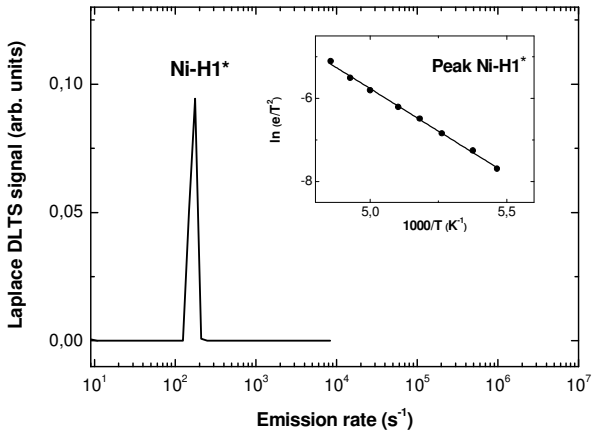

Fig.S.8. Laplace DLTS spectrum recorded in the Ni-diffused p-type Ge sample. The analytical parameters are: t_F = 200 µs, bias (−5V, −2V) and T = 200 K. The inset displays the Arrhenius plot of the hole trap Ni-H1*.

CONCLUSIONS AND PERSPECTIVES

This work is an attempt to examine some peculiar features related to metallic species of Fe, Cr, Ni and Au in *n*-type germanium studied, using conventional and Laplace DLTS techniques. Schottky barriers usage restricts the studies to levels located in the upper half of the band gap.

The n^+p junctions, which turned out to be very helpful in studying irradiation induced hole traps located in the lower half of the bandgap, turned out to be inefficient in the present study. The necessity of annealing the samples at 500 °C after implanting the metallic impurities seems to be harmful to the device characteristics. Only the case of Ni-doped n^+p mesa diode preparation turned out to be prosperous. This gives us possibility to characterize minority carrier trap by means of high sensitive Laplace DLTS method for the first time. However, by applying external optical excitation to generate minority carriers the investigation is extended to the lower half of the band gap.

Major findings already published by other authors are in several cases confirmed. However, new insight is revealed on the microscopic behavior of these four chemical species such as their interactions with hydrogen giving rise to the generation of complex-related levels in the band gap.

In case of Au new levels attributed to conjectural Au-H_n and Au-Sb complexes are observed. In addition development of both majority and minority carriers in MCTS analysis still is under consideration.

For the Fe case, the small difference in energy of its two levels raises the question as to the possibility of *negative-U* character. The single and double acceptors induced by Fe being very close to each other raises the legitimate and challenging

question of their ordering at about room temperature, with a possible inversion if they are both pinned to their respective allowed bands.

These mentioned points should be treated more thoroughly in a future work.

The previously published experimental data and data obtained in the given thesis lead to the results displayed in **Figure S.9**. Results obtained in the frame of the present work are presented by black color.

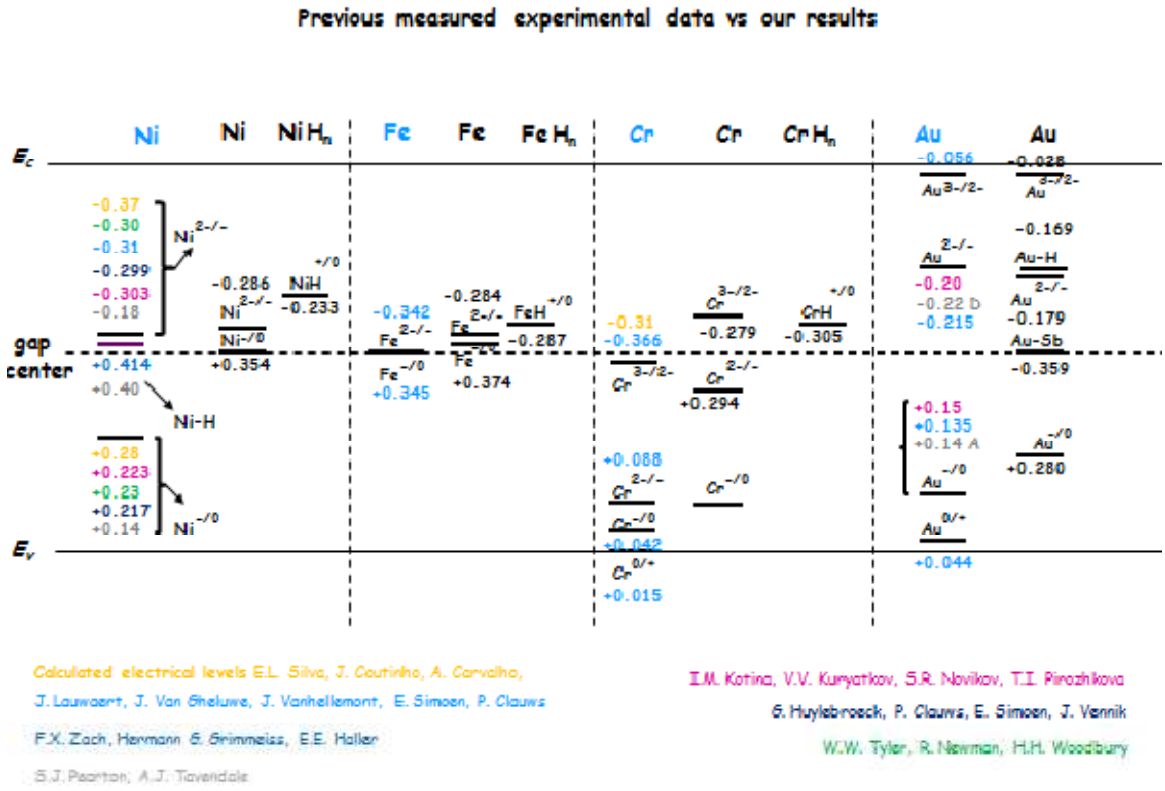

Fig. S.9. Deep-level parameters and assignments of electron and hole traps in Fe-, Cr-, Ni- and Au-implanted Ge [2-5, 7-10, 12, 17, 23-27].

Table S.1:

Overview of deep-level parameters obtained for TM impurity traps in Ge.

Level label	K_T ($s^{-1}K^{-2}$)	$\Delta E_{na/pa}$ (eV)	$\sigma_{na/pa}$ (cm^2)	σ_∞ (cm^2)	E_σ(eV)	$\Delta S_n/k_B$	ΔH_n(eV)
Fe-E1	7.1×10^{6}	0.327±0.002	$(2.3\pm0.4)\times10^{-16}$	$(4.98\pm0.39)\times10^{-15}$	0.043	3.08	0.284
Cr-E1	4.2×10^{6}	0.325±0.005	$(1.4\pm0.5)\times10^{-16}$	$(4.59\pm0.36)\times10^{-15}$	0.046	3.49	0.279
Ni-E1	5.5×10^{6}	0.321±0.005	$(1.8\pm0.6)\times10^{-16}$	$(4.09\pm0.32)\times10^{-15}$	0.035	3.12	0.286
Au-E1	3.3×10^{5}	0.047±0.002	$(1.1\pm0.9)\times10^{-17}$	$(3.37\pm0.54)\times10^{-14}$	0.019	8.03	0.028
Au-E2	1.3×10^{6}	0.212±0.001	$(4.2\pm1.6)\times10^{-15}$	$(2.99\pm0.34)\times10^{-13}$	0.033	4.27	0.179
CrX-E	1.5×10^{7}	0.305±0.002	$(4.7\pm0.7)\times10^{-16}$				
FeX-E	4.1×10^{6}	0.287±0.006	$(1.3\pm0.6)\times10^{-16}$				
NiX-E	1.4×10^{5}	0.233±0.009	$(1.2\pm2.2)\times10^{-17}$				
AuX-E1	3.1×10^{8}	0.359±0.006	$(1.0\pm0.5)\times10^{-14}$				
AuX-E2	6.5×10^{5}	0.169±0.004	$(2.1\pm0.6)\times10^{-17}$				
Ni- H1*	2.4×10^{6}	0.354±0.006	$(2.1\pm0.4)\times10^{-15}$				
Cr-H4	4.2×10^{8}	0.294±0.008	$(3.7\pm0.3)\times10^{-12}$				
Fe-H1	2.8×10^{8}	0.310±0.008	$(3.3\pm0.3)\times10^{-12}$				0.374
Ni-H1	3.6×10^{9}	0.336±0.020	$(4.2\pm0.8)\times10^{-12}$				0.378
Au- H2	1.3×10^{7}	0.280±0.005	$(1.1\pm0.8)\times10^{-13}$				

Peaks TM-H are related to hole trap. Thus, their characteristics are relative to the valence band.

Table S.2:

The signatures (E_{na}, K_T) and extrapolated capture cross sections σ_{na} derived from Arrhenius diagram in Laplace DLTS spectrum of Cr-contaminated *n*-type Ge, demonstrating the hydrogen presence.

Level label	K_T ($s^{-1}K^{-2}$)	E_T (eV)	σ_{na} (cm^2)
Cr-E1 (annealed)	1.1×10^{7}	0.336±0.002	$(3.6\pm0.2)\times10^{-14}$
CrX-E1 (not annealed)	4.1×10^{8}	0.350±0.010	$(1.3\pm1.0)\times10^{-14}$
Cr-E1 (not annealed)	1.1×10^{7}	0.337±0.007	$(3.6\pm0.5)\times10^{-14}$

BIBLIOGRAPHY

1. Blood, P. and J.W. Orton, *The Electrical Characterization of Semiconductors: Majority Carriers and Electron States*. 1992, London: Academic Press.
2. Clauws, P. and E. Simoen, *Metals in germanium.* Materials Science in Semiconductor Processing, 2006. **9**(4-5): p. 546-553.
3. Clauws, P., et al., *Deep level transient spectroscopy of transition metal impurities in germanium.* Physica B: Condensed Matter, 2007. **401-402**(0): p. 188-191.
4. Forment, S., et al., *A deep-level transient spectroscopy study of transition metals in n-type germanium.* Materials Science in Semiconductor Processing, 2006. **9**(4-5): p. 559-563.
5. Huylebroeck, G., et al., *DLTS of nickel impurities in germanium.* Solid State Communications, 1992. **82**(5): p. 367-369.
6. Lauwaert, J. and P. Clauws, *Majority carrier capture rates for transition metal impurities in germanium.* Thin Solid Films, 2010. **518**(9): p. 2330-2333.
7. Lauwaert, J., et al., *Electronic properties of titanium and chromium impurity centers in germanium.* Journal of Applied Physics, 2009. **105**(7): p. 073707-6.
8. Simoen, E., et al., *DLTS of gold impurities in germanium.* Semiconductor Science and Technology, 1987. **2**(8): p. 507.
9. Tyler, W.W., *Deep level impurities in germanium.* Journal of Physics and Chemistry of Solids, 1959. **8**(0): p. 59-65.
10. Tyler, W.W., R. Newman, and H.H. Woodbury, *Properties of Germanium Doped with Nickel.* Physical Review, 1955. **98**(2): p. 461-465.
11. Tyler, W.W. and H.H. Woodbury, *Properties of Germanium Doped with Iron. I. Electrical Conductivity.* Physical Review, 1954. **96**(4): p. 874-882.
12. Woodbury, H.H. and W.W. Tyler, *Triple Acceptors in Germanium.* Physical Review, 1957. **105**(1): p. 84-92.
13. Simoen, E. and C. Claeys, *Chapter 3 - Diffusion and solubility of dopants in germanium*, in *Germanium-Based Technologies*. 2007, Elsevier: Oxford. p. 67-96.
14. Vanhellemont, J., et al., *On the solubility and diffusivity of the intrinsic point defects in germanium.* Journal of Applied Physics, 2007. **101**(3): p. 036103-3.
15. Gurimskaya, Y., et al., *Spectroscopic studies of iron and chromium in germanium.* Journal of Applied Physics, 2011. **110**(11): p. 113707-7.
16. Dobaczewski, L., A.R. Peaker, and K.B. Nielsen, *Laplace-transform deep-level spectroscopy: The technique and its applications to the study of point defects in semiconductors.* Journal of Applied Physics, 2004. **96**(9): p. 4689-4728.
17. Simoen, E. and C. Claeys, *Chapter 5 - Metals in germanium*, in *Germanium-Based Technologies*. 2007, Elsevier: Oxford. p. 131-185.
18. Milnes, A.G., *Deep impurities in semiconductors*. 1973, New York: Wiley.

19. Simoen, E., et al., *Signature and capture cross section of copper-related hole traps in p-type high-purity germanium.* Semiconductor Science and Technology, 1986. **1**(1): p. 55-57.

20. Sachse, J.U., J. Weber, and H. Lemke, *Deep-level transient spectroscopy of Pd-H complexes in silicon.* Physical Review B, 2000. **61**(3): p. 1924-1934.

21. Mesli, A., P. Kringhøj, and A. Nylandsted Larsen, *Pinning behavior of gold-related levels in Si using Si_{1-x}Ge_{x} alloy layers.* Physical Review B, 1997. **56**(20): p. 13202-13217.

22. Frenkel, J., *On Pre-Breakdown Phenomena in Insulators and Electronic Semi-Conductors.* Physical Review, 1938. **54**(8): p. 647-648.

23. Zach, F.X., Hermann G. Grimmeiss, and E.E. Haller, *Nickel Related Deep Levels in Germanium.* Materials Science Forum (Volumes 83 - 87), 1992. **Defects in Semiconductors 16**: p. 245-250.

24. S.J, P., *Deep metal-related centres in germanium.* Solid-State Electronics, 1982. **25**(4): p. 305-311.

25. S.J, P., *A study of deep metal-related centres in germanium by capacitance spectroscopy.* Solid-State Electronics, 1982. **25**(6): p. 499-503.

26. Kotina, I.M., et al., *Capacitance spectroscopy of deep Cu, Au, Ag, and Ni centers in germanium.* Soviet physics semiconductors, 1987. **21**(6): p. 635.

27. Silva, E.L., et al., *Electronic structure of Zn, Cu and Ni impurities in germanium.* Journal of Physics: Condensed Matter, 2011. **23**(6): p. 065802.

LIST OF ABBREVIATION AND ACRONYMS

CMOS	Complementary Metal-Oxide Semiconductor
C-V	Capacitance-Voltage Characterization
DLTS	Deep Level Transient Spectroscopy
DOS	Density Of States
ESR	Electron Spin Resonance
IT	Information Technologies
I-V	Current-Voltage Characterization
Ge	Germanium
GeOI	Germanium-On-Insulator
GGA	Generalized Gradient Approximation
LDLTS	Laplace Deep Level Transient Spectroscopy
MCTS	Minority Carrier Transient Spectroscopy
MOSFET	Metal Oxide Semiconductor Field Effect Transistor
PF effect	Poole-Frenkel Effect
SCR	Space Charge Region in Schottky contact
Si	Silicon
SRIM	Stopping and Range of Ion in Matter
TM	Transition Metal

LIST OF PHYSICAL CONSTANTS

h	Plank constant	$4.135667516(91)\times10^{-15}$	eV·s
$\hbar$	$h/2\pi$	$6.58211928(15)\times10^{-16}$	eV·s
k_B	Boltzmann constant	$8.6173324(78)\cdot10^{-5}$	eV/K
e	Elementary charge	1.60219×10^{-19}	C
m_0	Electron rest mass	9.109382×10^{-31}	kg
ε_0	Vacuum permittivity	8.85418×10^{-12}	F/m

LIST OF USED SYMBOLS

ε_0	Permittivity of free space
ε_s	Relative dielectric constant
ξ	Electric field
μ	Carrier mobility
σ_{na}	Apparent carrier capture cross section extracted from the Arrhenius plot
σ_n, σ_p	Capture cross section for electrons, holes
σ_∞	Capture cross section at $T = \infty$
τ	Minority carrier lifetime
τ_r	Relaxation time
τ_{tr}	Time constant of deep state charge transient
τ_{ref}	Reference time constant of DLTS or rate window
φ_b	Barrier height [eV]
φ_m	Work function of metal
χ_s	Electron affinity of semiconductor
a_0	Lattice constant
A	Area of diode
C	Depletion capacitance
C_{Ge}	Concentration of germanium lattice atoms
C_I^*	Thermal equilibrium self-interstitial concentration
$c_{n,p}$	Capture rate for electrons and holes
ΔC	Amplitude of capacitance transient
C_∞	Steady state capacitance
C_v^*	Thermal equilibrium vacancy concentration
$C_{V,I}$	Vacancies and self-interstitials concentration [cm^{-3}]
$C_{v^-}^*$	The concentration of single negatively charged vacancy

D_{Ge}	Self-diffusion coefficient
$D_{Ge}^{(V)}$	Germanium tracer diffusion coefficient
$D_{n,p}$	Electron, hole diffusion constant
$D_{V,I}$	Diffusivity of vacancies and self-interstitials [cm^2s^{-1}]
E_t	Energy level of a deep center
E_{na}	Ionisation enthalpy, determined by Arrhenius plot
E_c, E_v	Conduction, valance band edge energy
E_F	Fermi-level
E_g	Semiconductor bandgap energy
E_f	Formation energy of defect
E_σ	Activation energy of trap capture cross section
e	Electron charge
e_n, e_p	Emission rate of electrons, holes from deep states
ΔG	Gibbs free energy
g_0, g_1	Degeneracy factors
ΔH	Enthalpy
h	Planck's constant, $\hbar = h/2\,\pi$
I	Current
$_I$	Interstitial site
I_s	Diode saturation current
k	Boltzmann's constant
L_D	Debye length
m_0	Free electron mass
m^*	Carrier effective mass
N_c, N_v	Effective density of states at conduction, valance band edge
N	Doping density obtained from C-V profiling
N_a, N_d	Acceptor, donor density

n_i	Intrinsic free electron density
N_t	Deep state (trap) density
n	Free electron density
n_0	Free electron density in neutral material
n_t	Density of electrons on deep states
p	Free hole density
p_t	Density of holes on deep states
S	Output signal from DLTS system
s	Substitutional site
ΔS	Entropy associated with emission or capture of carrier at electron state
t	Time
t_F	Filling pulse duration
T	Temperature [K]
T_M	Melt temperature
T_m	Temperature of the peak at maximum
X	Impurity
V	Voltage
V_0	Filling voltage
V_a	Applied voltage
V_b	Built-in voltage
V_f, V_r	Forward, reverse applied bias
v	Carrier drift velocity
$\langle v_n \rangle$, $\langle v_p \rangle$	Average thermal velocity of electrons, holes
x_d	Depletion width
x_0	Depletion width at low bias (during trap filling)

TABLE OF CONTENTS

STATE-OF-THE-ART. GENERAL CONCEPTS

INTRODUCTION

GENERAL BACKGROUND

All hardware aspects of mankind's technologies are based on and limited by materials. Modern scientific and technological challenges and the transition from industrial to information society are largely driven by higher performance of intellectual work through Information Technology (IT), built-up on semiconductor based devices.

The old story about the most promising nowadays material to replace silicon in semiconductor applications started in 1947 on Christmas Eve by *John Bardeen*, *Walter Brattain* and *William Shockley* at Bell Labs, who had used elemental polycrystalline germanium (Ge), to co-invent the first transistor. For their discovery of the transistor effect all three scientists were awarded the 1956 Nobel Prize in Physics.

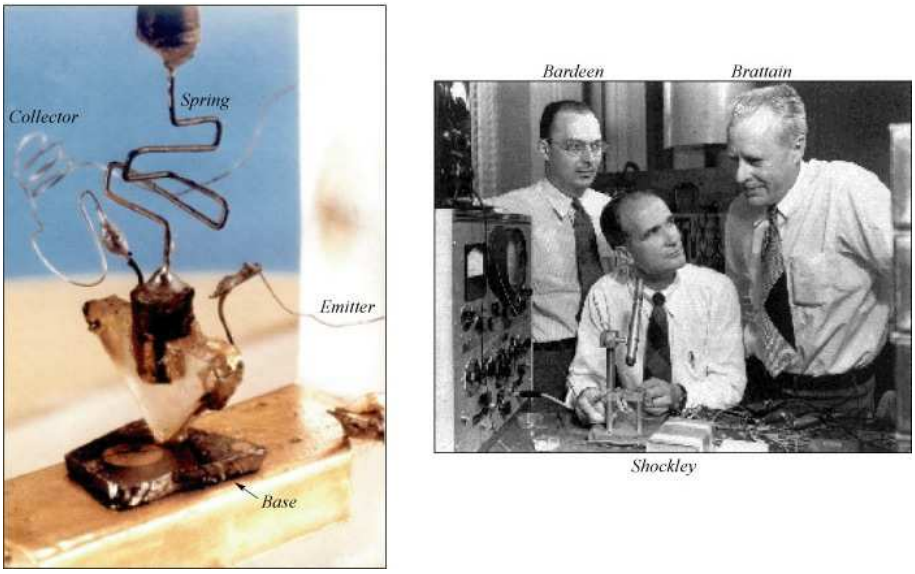

Fig.I.1. The first point contact transistor. *John Bardeen*, *Walter Brattain* and *William Shockley*, Bell laboratories, Murray hill, New Jersey, 1947.

In spite of the fact that elemental group IV semiconductor – Ge – was an ancestor of all modern devices, silicon (Si) quickly took over as the main semiconductor material, used in electronic technology still today, because of several important advantages such as:

- Greater natural abundance - the major raw material for Si wafer fabrication is *sand* (SiO_2), which means low production price;

- A larger bandgap (1.1 eV), allows Si devices to operate at higher temperatures;
- Thermal oxide, SiO_2, stability, playing the role of surface dielectric;
- Excellent SiO_2-Si interface with a very low surface state density ($\sim 10^{10}$ cm^{-2} eV^{-1}).

After introducing Si as a substantially single crystalline substrate material, the interest in Ge gradually declined for about thirty years, although it remained in nuclear physics as one of the best material for detectors with a good energy resolution. Today applications change and develop and so does the requirement. The search of higher carrier mobilities and lower post-implant thermal budgets is making Ge-based technology attractive and is expected to boost the driven current of field-effect transistors and their response frequency limit. Additionally, because of high crystallographic perfection and mechanical strength, germanium becomes a key material in multi-junctions technology to adapt various III-V compounds layers of different band gaps with minimal generation of dislocations to convert the largest part of the solar spectrum with the highest possible efficiency.

For a straightforward comparison **Table I.1** lists the fundamental properties of silicon and germanium at room temperature (RT, 300 K).

Given its advantageous physical and chemical properties, germanium offers five important fields of application: infrared detectors, optical lenses and optical fibers for infrared application, and, more recently germanium is playing major role in electronic and solar cells applications.

Since the early days of semiconductor processing, it was realized that great care has to be taken to avoid inadvertent contamination by fast diffusing metals during the numerous thermal steps in device processing. The solubility and diffusivity of metals in Ge might be as high as in silicon thus detrimental. Due to the perspective of applying Ge in advanced electronic devices (*MOSFET*[1], *CMOS*[2] circuits, *GeOI*[3] substrates), a remarkable revival of the interest in the electronic properties of impurities and defects in Ge has occurred in the past few years. Today, the data collected on germanium scatter more or less, depending on their nature, requiring often a re-examination and this task is undertaken by different groups belonging to the defect community. *Clauws et al.* [1-4] are of no doubt undertaking the most thorough studies on metallic impurities in germanium mainly via the very well known Deep Level Transient Spectroscopy technique (DLTS).

[1] MOSFET – Metal Oxide Semiconductor Field Effect Transistor

[2] CMOS – Complementary Metal-Oxide Semiconductor

[3] GeOI – Germanium-On-Insulator

	Symbol	Ge	Si	Unit
Crystal structure		Diamond	Diamond	–
Group of symmetry		*Fd3m*	*Fd3m*	–
Gap		Indirect	Indirect	–
Lattice constant	a_0	5.65791	5.43110	Å
Density		5.3267	2.3280	g/cm^3
Bandgap energy	E_g	0.661	1.12	eV
Intrinsic carrier concentration	n_i	2.4×10^{13}	1.5×10^{10}	cm^{-3}
Effective DOS at CB edge	N_c	1×10^{19}	2.8×10^{19}	cm^{-3}
Effective DOS at VB edge	N_v	6×10^{18}	1×10^{19}	cm^{-3}
Electron mobility	μ_n	3900	1500	cm^2/V·s
Hole mobility	μ_p	1900	475	cm^2/V·s
Electron diffusion constant	D_n	101	39	cm^2/s
Hole diffusion constant	D_p	49	12	cm^2/s
Electron affinity	χ_s	4.0	4.05	V
Minority carrier lifetime	τ	$\approx10^{-3}$	2.5×10^{-3}	s
Electron effective mass	m_e^*	1.64 m_e	0.98 m_e	–
Heavy hole effective mass	m_{hh}^*	0.28 m_e	0.49 m_e	–
Light hole effective mass	m_{lh}^*	0.44 m_e	0.16 m_e	–
Dielectric constant	ε_s	16.2	11.9	–

Table I.1: Properties of Ge and Si at room temperature.

This PhD thesis focuses on Fe, Ni, Au and Cr in Ge and presents extensive DLTS, MCTS and Laplace DLTS results aiming at re-examining various properties of the multi-acceptor states, induced by these transition metals. Among these properties one may cite barriers for capture of electrons and holes, the number and positions of the relative states introduced in the band gap and their distribution, the effect of the electric field in the capture-emission processes (also called Poole-Frenkel effect). All these properties are important to understand the behavior of the impurities and the host material. We also bring new insights into the microscopic behavior of these chemical species such as their interactions with hydrogen present as an unwanted contaminant giving rise to the generation of complex related levels in the band gap. For the Fe case, the tiny difference in energy of its two levels raises the question

about the possibility of negative-U character which has also been addressed in this work.

This report is organized as follows. Firstly, **Chapter I** contains an overview of current knowledge of transition metal impurities in germanium, and in particular of Au, Ni, Fe and Cr. In **Chapter II** the principles of the most extensively used techniques, such as DLTS, MCTS and Laplace DLTS to investigate electrically active defects in semiconductor bandgap, are introduced after having recalled the principle of Schottky barrier. Relevant information about sample preparation and experimental setup used in this work are described in **Chapter III**. **Chapter IV** is focused on experimental results in details**.** Finally, **Chapter V** contains summary and discussion of the main results obtained within the framework of this research.

CHAPTER I. STATE-OF-THE-ART. GENERAL CONCEPTS.

1.1. GERMANIUM. CURRENT KNOWLEDGE.

1.1.1. Fundamental properties of germanium

The lattice location of metals is known to play a major role regarding their electrical activity. Therefore, it is worth to recall the main properties of an ideal germanium crystal. Elemental germanium crystallizes in the diamond lattice like silicon, which means in the perfect crystal all Ge atoms are tetrahedrally bonded like as displayed in **Figure 1.1**.

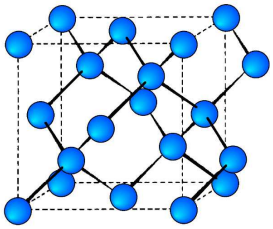

Fig. 1.1. Unit cell structure of a diamond cubic lattice.

The understanding and accurate description of energy band structures is fundamental in the development of electronic devices. Ge is a prototypical semiconductor with an experimentally determined indirect band gap of 0.742 eV at zero Kelvin and 0.66 eV at RT, which is the energy difference between the minimum of the conduction band at point *L* in reciprocal space and the top of the valence band at *Γ* [5]. The direct band gap at the center of the Brillouin zone is measured to be 0.9 eV. **Figure 1.2(a)** and **(b)** compare the band structure of Ge and Si.

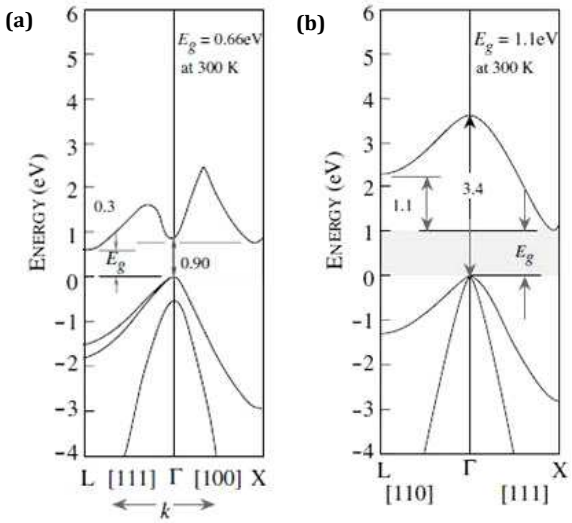

Fig.1.2. The electronic band structure of (a) Ge and (b) Si.

At RT the size of the band gap is 0.662 eV while it increases to 0.742 eV with decreasing temperature [6]. The temperature dependence of the energy gap in Ge is expressed by the following equation

$$E_g(T) = 0.742 - 4.8 \cdot 10^{-4} \cdot \frac{T^2}{(T+235)} (eV)\,, \qquad (1.1)$$

which is illustrated in **Figure 1.3** [5].

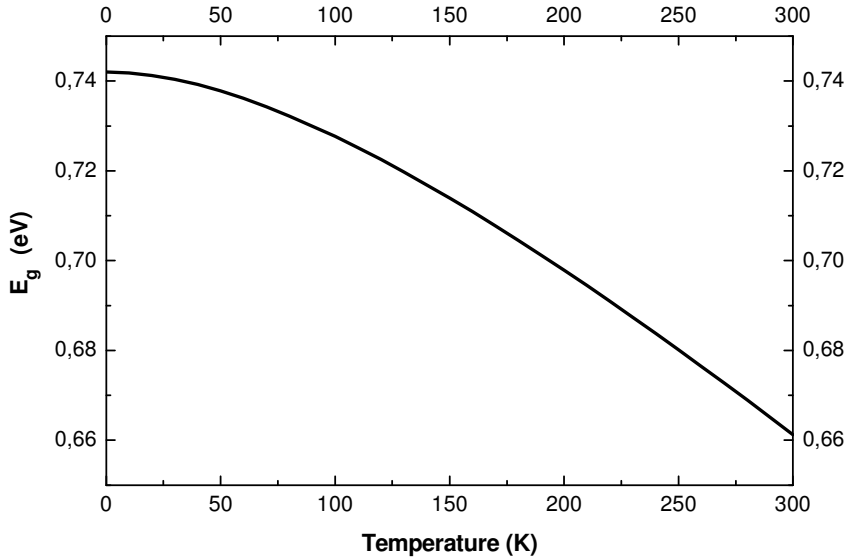

Fig.1.3. Temperature dependence of Ge bandgap.

1.1.2. Intrinsic point defects in germanium

Point defects exist in small concentration in all semiconductor materials including Ge, but they can also be introduced intentionally by various means such as irradiation, implantation or during thermal processes. Due to its technological importance, knowledge of the energy required to form intrinsic point defects in a semiconductor is necessary for understanding and controlling the electrical properties, self-diffusion and dopant diffusion processes. Hence, we report below some of the few information available on the properties of the vacancy and the self-interstitial in Ge and supported by *ab initio* calculations.

Self-diffusion in Ge is the slowest process and provides direct evidence of the existence of an equilibrium concentration of intrinsic point defects. Recent experiments of Cu and Ni diffusion in Ge crystals of *Giese et al.* [7] and radioactive tracer diffusion measurements [8, 9] showed that in contrast to Si, the self-diffusion coefficient D_{Ge} is dominated by vacancies, whereas self-interstitials do not play a

major role, except possibly after ion implantation. Strong experimental evidence based on tracer diffusion led to the coefficient $D_{Ge}^{(V)}$ [10]

$$D_{Ge}^{(V)} = \frac{0.5\, C_V^* D_V}{C_{Ge}} \tag{1.2}$$

which is very close to self-diffusion coefficient

$$D_{Ge} = \frac{0.5 C_V^* D_V}{C_{Ge}} + \frac{0.73 C_I^* D_I}{C_{Ge}}, \tag{1.3}$$

where C_V^* and C_I^* are the thermal equilibrium vacancy and self-interstitial concentrations, respectively; C_{Ge} is the concentration of germanium lattice atoms, $C_{V,I}$ (in cm^{-3}) and $D_{V,I}$ (in $cm^2 s^{-1}$) are the solubilities and diffusivities of vacancies and self-interstitials, respectively. **Relation (1.2)** matches with **relation (1.3)** if we consider inequality.

$$C_I^* D_I \ll C_V^* D_V. \tag{1.4}$$

Concerning thermal equilibrium vacancy concentrationC_V^*, the results based on annealing experiments on acceptors quenched into germanium were obtained by *Mayburg* [11]

$$C_{V^-}^* = 3 \times 10^{23} e^{-2.01\, eV/kT}\ cm^{-3}, \tag{1.5}$$

where $C_{V^-}^*$ is the single negatively charged vacancy concentration.

This relation predicts an equilibrium vacancy concentration of $1.3 \times 10^{15} cm^{-3}$ at the melting temperature T_M. This is in good agreement with the estimate $2.9 - 3.9 \times 10^{15} cm^{-3}$ obtained by *Tweet* [12] from Cu precipitation and diffusion experiments. **Table 1.1** lists the available experimental data for the single negatively charged vacancy in Ge. No experimental data are available on the formation energy of self-interstitial in Ge.

$E_f^{V^-}$ (eV)	$C_{V^-}^0$ (site fraction)	Reference
2.01	6.8	*Mayburg* [11]
1.79	1.3	*Tweet* [12]
2.09	-	*Giese et al.* [7]

Table 1.1: Experimentally determined formation energy $E_f^{V^-}$ and prefactor $C_{V^-}^0$ of the single negatively charged vacancy in Ge.

According to *Giese et al.* [7] the self-diffusion coefficient of Ge is dominated by vacancy diffusion and is given by

$$D_{Ge} \approx 13.6e^{-3.09\,eV/kT}\ cm^2s^{-1} \tag{1.6}$$

leading to

$$C_V^* D_V \approx 1.18 \times 10^{24} e^{-3.09\,eV/kT}\ cm^2 s^{-1}. \tag{1.7}$$

With a formation energy of 2.0 ± 0.1 eV for the single negatively charged vacancy [13], a vacancy migration energy of 1.1 eV is estimated. In **Table 1.2** a best estimate is given for the formation energy of the different charge states of the vacancy in Ge [13]. The best estimates are also represented graphically in **Figure 1.4** illustrating that the single negatively charged vacancy is the dominant intrinsic point defect in Czochralski pulled Ge.

E_f^{V0} (eV)	C_{V0}^0 (site fraction)	E_f^{V-} (eV)	C_{V-}^0 (site fraction)	E_f^{V--} (eV)	C_{V--}^0 (site fraction)
2.35 ± 0.11	28 ± 16	1.98 ± 0.11	5.0 ± 2.8	2.19 ± 0.13	0.22 ± 0.13

Table 1.2: Best estimates for the formation energy E_f^{V-} and prefactor C_{Vx}^* of the vacancy in germanium in three charge states [13].

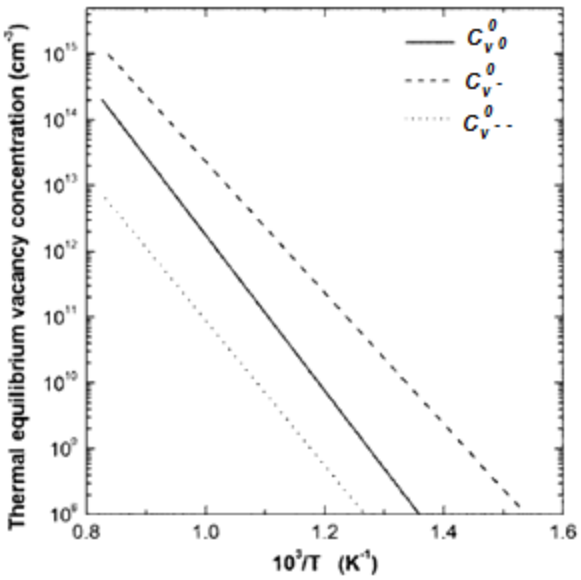

Fig.1.4. Best estimate of thermal equilibrium vacancy concentrations in Ge versus T [13].

Figure 1.5 shows **(a)** the self-diffusion coefficients and **(b)** $C_V^* D_V$ for Si and for Ge as a function of the normalized temperature T_m/T.

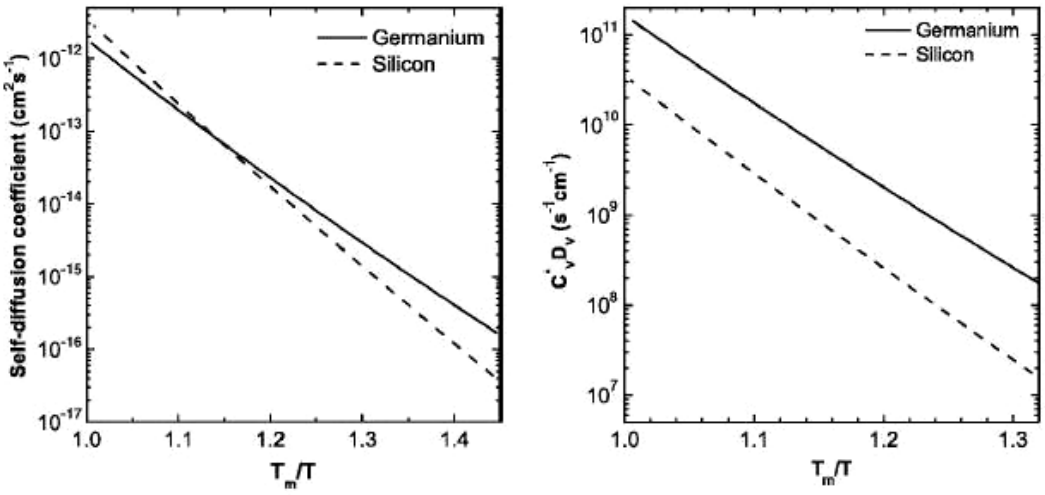

Fig.1.5. Self-diffusion coefficients and $C_V^* D_V$ in Si and Ge as a function of the normalized temperature T_M/T [14] .

Table 1.3 summarizes the calculated formation energy E_f of vacancy (V) and interstitial (I) in Ge compared to Si [15]. For the self-interstitial, tetrahedral (T), hexagonal (H), bond-centered (BC), and ⟨110⟩ dumbbell (D) sites are calculated. It is found that the formation energy of vacancies in Ge (E_f = 2.56 eV) is smaller than that in Si (E_f = 3.81 eV). Four Ge atoms around the vacancy move 0.046 nm inward from their original position to reduce the total energy. The calculations show that the most stable site for the self-interstitial in Ge is the D site, as is also the case in Si. The formation energy of the self-interstitial at the D site in Ge (E_f = 3.50 eV) is very close to that in Si (E_f = 3.51 eV). The distance between two Ge atoms at the D site is 0.251 nm.

	Vacancy	Self-interstitial			
		T	***H***	***BC***	***D***
Si	3.81	3.82	3.56	4.89	3.51
Ge	2.56	3.78	3.97	5.10	3.50

Table 1.3: Calculated formation energies E_f (eV) of the uncharged vacancy and self-interstitial in Si and Ge.

To summarize, the properties of the intrinsic point defects such as the interstitial, vacancy, di-vacancy, and Frenkel pairs recently published [16-21] are still rather scanty relative to that in Si. A study of these very unstable primary defects could only be possible when irradiation is done at helium temperatures followed by in-situ

characterization. One of the major outcomes of these studies is the clear observation of the self-interstitial and Frenkel pair which has never been detected in silicon. These elementary building blocks play a major role in diffusion processes, and their respective charge states and thermal stability are thus key factors for a good control of device processing.

1.2. METALLIC IMPURITIES IN GERMANIUM

The electronic properties of metallic impurities in Ge have been quite intensively studied about 50 years ago. However the tools were mainly Hall-effect and conductivity measurements [22], which present some limitations. If these methods were particularly useful for shallow donors and acceptors, for deep levels they required working with high resistivity materials. Making the materials highly resistive by reducing the dopants concentration rendered the experiments hard to conduct. The development of junction techniques allowed eliminating the need for high-resistive materials, opening a new era in the domain of point defects studies.

Among all kind of defects, transition metals (TM) can be effective lifetime killers due to the introduction of deep electronic levels in the bandgap of the semiconductor. They can act as generation, recombination or trapping centers for the charge carriers, and are therefore detrimental to the device operation by increasing the leakage current for instance. The exact electrical behavior of such deep-level centers will largely depend on the energy levels E_{na}, total trap concentrations N_T and the capture cross sections for electrons σ_n and holes σ_p [2].

Today the collected data in germanium are by far much less complete than in silicon thus still exhibiting some scattering. Currently no general formalism exists to predict the physical properties of deep level impurities in semiconductor. New insights into deep level behavior are thus still substantially needed essentially through experimental studies.

1.2.1. Solubility and diffusivity of Au, Cr, Ni and Fe in Ge

Typically, metals in Ge have a high diffusivity D, which means that they can easily be integrated into the lattice from the surface during one of the numerous step of device manufacturing, among which the most critical is thermal treatment. In addition, they have a low solid solubility S_0, which enhances their tendency to precipitate during subsequent cooling from high temperature.

The studies of Au doping in Ge indicated a maximum solubility in the range $4.1 \times 10^{16} cm^{-3}$ [2]. For Ni a maximum retrograde solubility is observed near 900 °C ($\sim 8 \times 10^{15} cm^{-3}$) [2, 23]. The maximum solubility of Fe appears to be

$\sim 1.5 \times 10^{15} cm^{-3}$ [23] at ~800 °C. Less complete information is available for Cr in Ge. Its solubility is low but accurate measurements have not been made [23].

Interstitial-substitutional (*i-s*) diffusion processes in germanium via the dissociative mechanism are characterized by *i-s* interchange of the impurity (X) via vacancies (V) according to

$$X_i + V \rightleftharpoons X_s. \tag{1.8}$$

As a consequence, the valence electrons of the TM impurity in germanium on the substitutional (S) sites are involved in the local bonding, allowing acceptor states to prevail (**Figure 1.6**). The vacancy is the "*hole*" with which the foreign TM atom couples to and produces the resulting impurity-host hybrid states. The four dangling bonds at the vacancy can induce a doubly occupied triplet level in the gap. This makes it able to trap up to three electrons. It is thus highly likely that the vacancy model developed by Watkins holds for transition metals in germanium [24]. For comparison in silicon the transition metals stabilize mainly in interstitial (I) sites, impeding them from engaging their valence electrons with their neighbors leading to donor states.

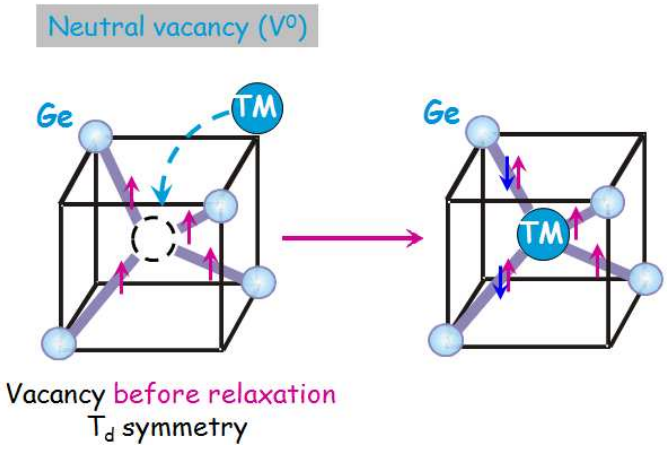

Fig.1.6. Schematic representation of the vacancy diffusion mechanism for TMs in Ge and the double acceptor formation.

The data are described by four individual Arrhenius expressions for each impurity:

$$D_{Au} = 1.05 \times 10^{-2} \exp\left(-1.52\ eV/k_B\,T\right) cm^2 s^{-1} \text{ [2]} \tag{1.9}$$

$$D_{Ni} = 0.8 \exp(-0.91 eV/k_B\,T)\ cm^2 s^{-1} \text{ [14]} \tag{1.10}$$

$$D_{Fe} = 0.19 \exp\left(-1.22\ eV/k_B\,T\right) cm^2 s^{-1} \text{ [25]} \tag{1.11}$$

$$D_{Cr} = 3.8 \times 10^{-4} \exp\left(-0.71\, eV / k_B\, T\right) cm^2 s^{-1}$$ [25]. (1.12)

The diffusion coefficients of Fe, Cr and Ni resulting in **Figure 1.7** are plotted versus inverse temperature.

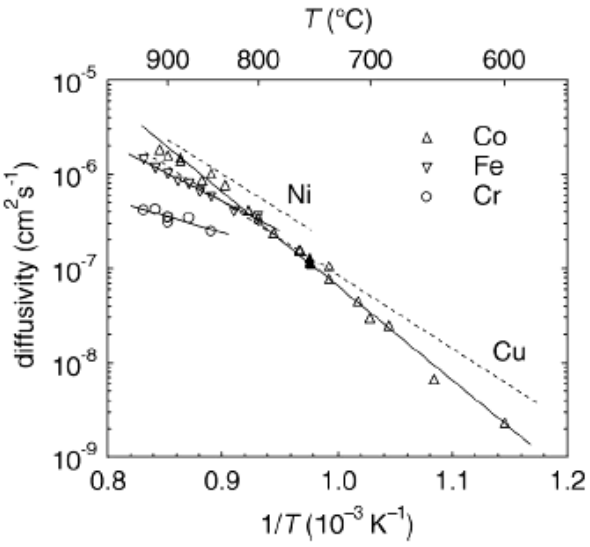

Fig.1.7. Temperature dependence of diffusion coefficients of Fe, Cr and Ni in as-grown Ge [26].

The standard deviation in the activation energies (Q_D) are 0.06 and 0.16 for Fe and Cr, respectively, whereas the corresponding uncertainty factors in the pre-exponential factors (D_0) amount to 1.8 and 4.9 in both directions.

1.2.2. Electronic and energetic properties of metallic atoms in Ge

Since the introduction of Ge-based diodes and transistors during the early 1950s a simple model for the incorporation of *3d* metals has been proposed and turned out to work remarkably well. *Tyler* and *Woodbury* [27] suggested that the multi-acceptor states expected from transition metals in germanium should result from their tendency to complete the tetrahedral bonding arrangement with the four nearest germanium atoms.

From the theoretical point of view [25], the question whether a TM impurity is more stable in a substitutional or interstitial site is usually answered by calculating formation energies. The formation energy is calculated as the energy difference between the total energies of an ideal supercell of host matrix with and without TM atom considering the chemical potential of the TM atom (μ_{TM}).

The formation energy of a single vacancy in a sufficiently large supercell within the Ge host matrix can be approximated to

$$E_F(V) \approx E(C_{N-1}) - [E(C_N) - \mu_{Ge}], \tag{1.13}$$

where $E(C_N)$ is the total energy of a pure Ge unit cell with N germanium atoms, among which one can be replaced by either a vacancy or an impurity; $E(C_{N-1})$ the total energy of a similar cell with a single vacancy at the center, μ_{Ge} is the chemical potential of Ge, taken equal to the total energy per atom in bulk Ge. By using a value for $E_F(V)$ from a periodic calculation, μ_{Ge} can be estimated at the center of the cell

$$\mu_{Ge} \approx E(C_N) + E_F(V) - E(C_{N-1}). \tag{1.14}$$

The relative formation energies E_r of interstitial (TM_i) and substitutional (TM_s) impurities are respectively

$$E_r(TM_i) = E(C_N TM_i) - E(C_N) \tag{1.15}$$

and

$$E_r(TM_s) = E(C_N TM_s) - [E(C_N) - \mu_{Ge}] \text{ [25]}. \tag{1.16}$$

Figure 1.8 summarizes the formation energies for TM species obtained within generalized gradient approximations (*GGA*) [28].

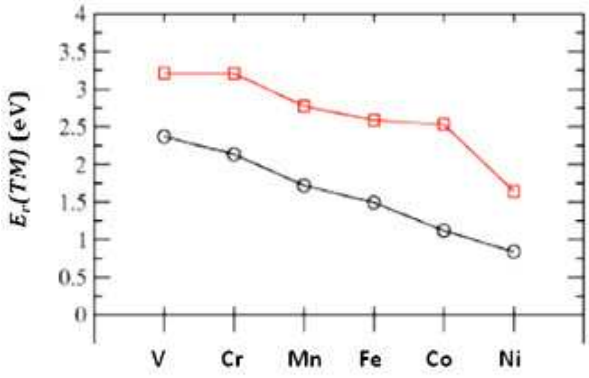

Fig.1.8. The formation energy calculated within GGA for the substitutional (black circles) and interstitial (red squares) TM defects in Ge as a function of the TM atomic species [28].

Results displayed in **Figure 1.8** show that the substitutional site is favored over the interstitial one for all TM of the *3d* series. In addition, the formation energies for both substitutional and interstitial sites decreases as the *3d* shell becomes more and more occupied.

The combined approach of emission channeling experiments and *ab initio* total energy calculations [29] led to the fact that a large fraction of ion implanted TMs was

found on the substitutional *S* site together with a smaller fraction located on the bond-centered *BC* site. This result contributes significantly to the understanding of the electrical properties of transition metals in germanium, since they are known to be electrically active on the *S* site, while no active defect levels have been attributed to TMs on the *BC* site. Corroborated by theory, this *BC* fraction is attributed to impurity-vacancy complexes in the split-vacancy configuration. By investigating the formation energy of this complex, it can be concluded that the mobile vacancies, created during the ion implantation process, are trapped by substitutional impurities, resulting in the spontaneous occupation of the *BC* site. Hence, this *BC* behavior is a direct consequence of the presence of mobile vacancies, which can be created during the ion implantation process.

In order to better understand the electronic properties of TM impurities, we need to consider an elementary model, based on simple electron-filling criteria. The electrons which come into play, when a TM replaces a Ge atom, are those belonging to the *p* states of Ge and to the *d* and *s* states of the TM atom. Cubic symmetry splits the five-fold degenerate TM *d* states into three-fold t_2 and two-fold *e* degenerate states. The coupling of TM to the Ge host in cubic symmetry is determined by linear combinations of t_2 derived states from the TM and the *p* states of Ge, having t_2 symmetry as well. The *d* derived *e* states do not participate to the bonding due to symmetry rules, and therefore form nonbonding states well localized in energy and space [28]. This picture presented in **Figure 1.9** is known as the *Watkins model*.

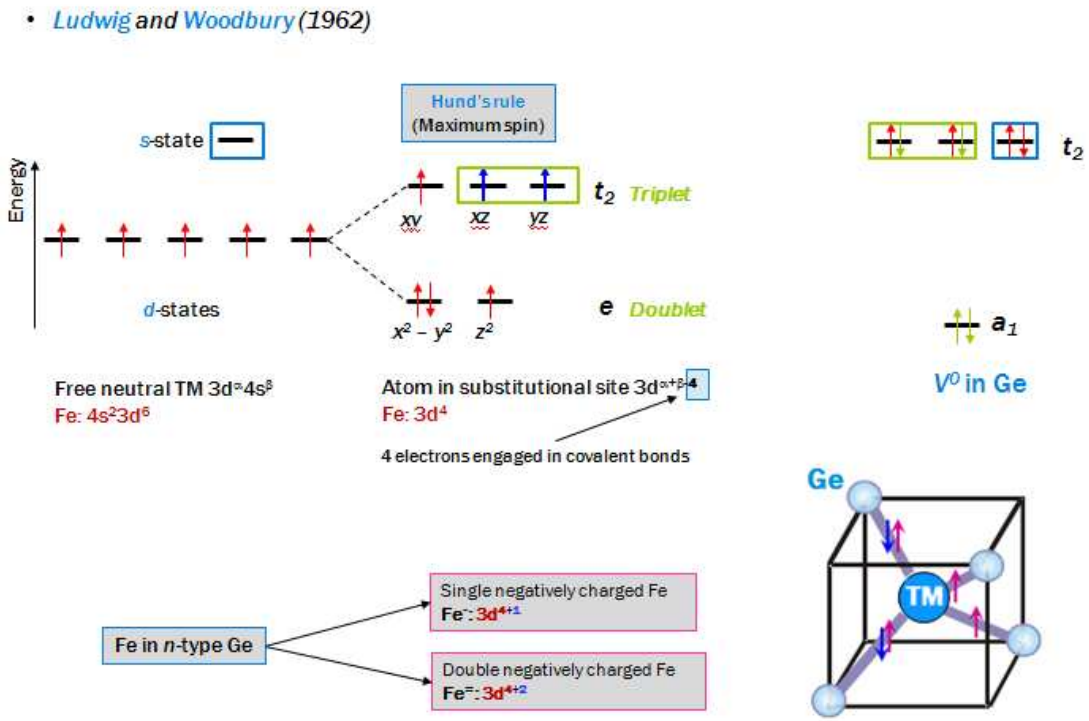

Fig.1.9. Simplified schematization of the Watkins model mechanism.

State-of-the-art concludes with respect to the metals, that Group I elements such as Cu, Ag and Au will be triple acceptors, Group II impurities such as Zn, Be, Cd, Hg and the transition elements – Mn, Fe, Co, Ni – which have two *4s* electrons in the outer shell, act as double acceptors. The established exceptions to this general rule are the donor levels of Ag, Au and Cr, which by giving up their one valence electron, can take up the closed shell configuration, which is energetically quite favorable.

Figure 1.10 summarizes the position of energy levels induced by substitutional metal impurities in Ge bandgap, depicted schematically [1, 3, 4, 23, 30-32]. The energy values in eV are given positive relative to the top of the valance band E_v and negative relative to the bottom of the conduction band E_c. The acceptor level of Cu at 0.002 eV, marked by blue color, which may be considered as (+/0) occupation level, is included. In the case of platinum only two acceptor states have been reported, while a third level is expected based on the electronic configuration ($6s^1$). This state could merge with the conduction band and be thus not observable [33].

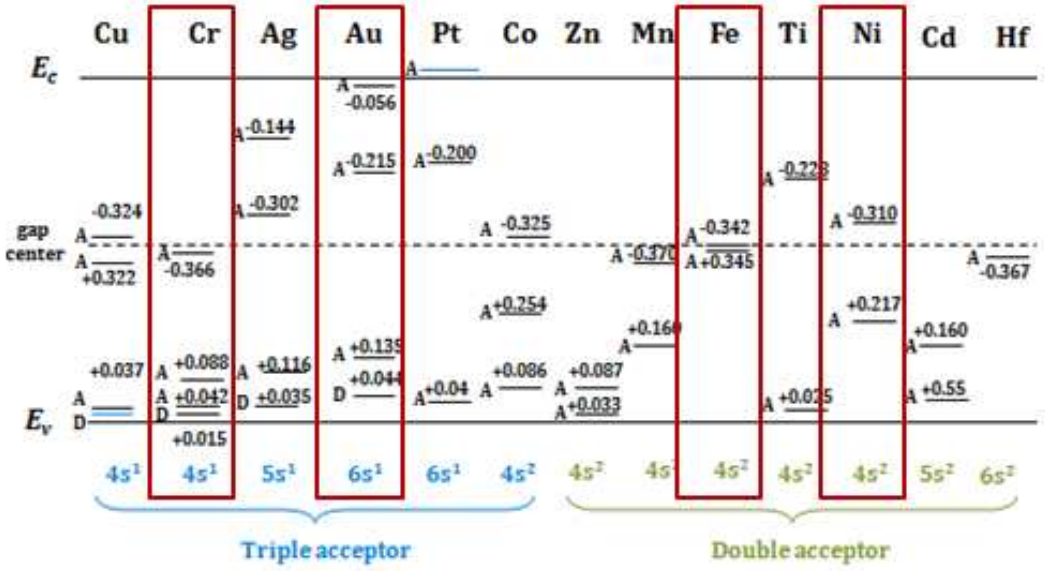

Fig.1.10. The deep acceptor (A) and donor (D) levels in the Ge bandgap induced by substitutional Cu, Ag, Au, Pt, Cr, Co, Zn, Mn, Fe, Ti, Ni, Cd and Hf.

The electronic configuration of metal atom gives only some indications on the number of levels to be expected in the band gap of germanium. The position of these levels will also be determined by some extent by the atomic radius (size) of the impurities involved: the heavier (the larger the atomic number) the farther the corresponding level from its respective band will be (see **Figure 1.10**). It should also be remarked that the order of the levels is determined by the rule that the more negative the charge state is, the higher the ionization energy [2]. Such behavior is corresponding to so-called positive *U*-centers, when multivalent impurities behave

normally in the ionic host – the charge state goes from the most negative to the less negative if we move from the conduction band E_c toward to the valance band E_v.

1.2.3. Au, Ni, Cr and Fe impurity centers in Ge

With respect to the model described in **Section 1.2.2.**, Au ($6s^1$), Cr ($4s^1$), Ni ($4s^2$) and Fe ($4s^2$), the four metals dealt with in the present work, are expected to introduce triple, for the first two, and double acceptor states, for the last two species. This has clearly been shown by *Clauws et al.*, [1, 3, 4, 31] with the exception that for chromium a fourth donor level seems to merge next to the triple acceptor state. A summary of the results obtained for Cr, Fe, Ni and Au is displayed above.

In *n*–type Cr-implanted Ge a single electron trap Cr–E1 was observed by DLTS (**Figure 1.11 a)** at 173 K with no other resonances down to a temperature of 8 K.

Obtained from Arrhenius diagram trap signature is listed in **Table 1.4**. The real capture cross section could be directly measured and was found to be thermally activated. The capture parameters are included in **Table 1.4**. The capture barrier amounts to 56 meV, allowing a correction of the apparent activation energy of Cr-E1 to an enthalpy of ΔH=0.311 eV and resulting in a fairly high value for the entropy ΔS=(6.73±0.35)k_B. It was also found that the position of Cr-E1 resonance is independent of the electric field strength. The observations are in agreement with assignment to a multiple acceptor.

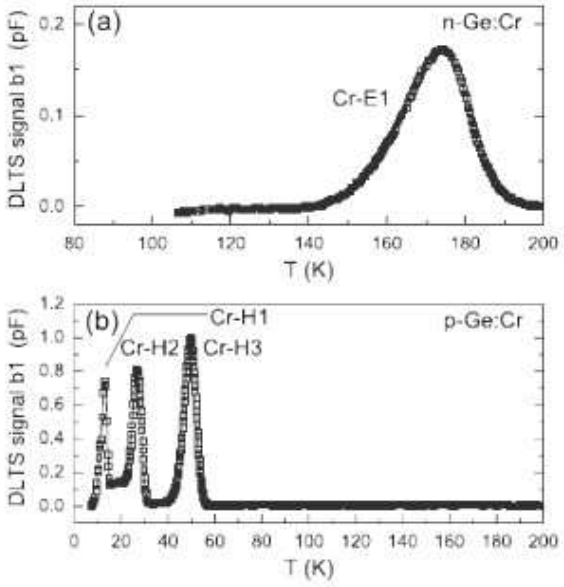

Fig.1.11. DLTS of Cr-implanted germanium: bias -1 V →-0.01 V, pulse duration 2 ms; (a) *n*-type, τ_{ref} =23.5 ms; (b) *p*-type, τ_{ref}=2.1 ms [4].

For *p*-type chromium three hole traps Cr–H1, Cr–H2 and Cr–H3 could be observed (**Figure 1.11 b**) [4]. The signatures of these three levels have been included in **Table 1.4**. The presence of a Poole–Frenkel shift [34], stresses the acceptor character of the Cr–H2 and Cr–H3 levels. The field dependence of the apparent activation energy for Cr-H2 and Cr-H3 levels helps determining the zero field corrected values of E_{pa} which are given in **Table 1.4**. This electric field dependence observed for Cr-H2 and Cr-H3 is typical for acceptor levels, which are attractive for holes, while the behavior of Cr-H1 is in agreement with a donor level.

Level label	Level assignment	Energy level (eV)	K_T ($s^{-1}K^{-2}$)	σ_{na}/σ_{pa} (cm^2)	σ_∞ (cm^2)	ΔE_σ (eV)	ΔH (eV)	$\Delta S/k_B$
Cr-E1	$Cr_s^{(2-/3-)}$	E_c-0.364 (A)	5.2×10^{7}	1.8×10^{-14}	2.2×10^{-17}	0.056	0.310	6.7
Cr-H3	$Cr_s^{(-/2-)}$	E_v+0.088 (A)	1.6×10^{8}	1.7×10^{-13}			0.095	
Cr-H2	$Cr_s^{(0/-)}$	E_v+0.042 (A)	3.9×10^{7}	4.1×10^{-14}			0.048	
Cr-H1	$Cr_s^{(+/0)}$	E_v+0.015 (D)	1.7×10^{6}	1.8×10^{-15}				

Table 1.4: Energy levels and assignments of the DLTS bands of Cr-diffused germanium [4]; (A) – acceptor level; (D) – donor level.

For Fe-implanted *n*-type germanium also one single electron trap Fe–E1 could be observed (**Figure 1.12 a**). Direct capture experiments [3] reveal a thermally activated capture cross-section: E_σ=49.88±0.06 meV and σ_∞=3.7±0.4×10^{-15}cm^2. The trap signature is listed in **Table 1.5**. An extrapolation to room temperature gives the capture cross-section of 5.3×10^{-16}cm^2, which is in excellent agreement with the photoconductivity measurements of *Belyaev* and *Malogolovets* [35]. The extracted entropy and enthalpy change for electron emission are ΔS=1.98±0.12k_B and ΔH=0.293±0.001 eV. The enthalpy change is in fair agreement with the E_{na} =0.27±0.02 eV observed by means of Hall-effect measurement of *Tyler* and *Woodbury* [36].

For *p*-type Fe-implanted germanium a hole trap Fe–H1 was observed (**Figure 1.12 b**) where the emission could be described by the following signature (K_T=2.0×10^{-9} $K^{-2}s^{-1}$; E_a=0.345 eV). Within the temperature range of the emission peak (130–145 K) no variation in capture cross-section could be observed. The average capture cross-section is σ=2.35±0.03×10^{-14} cm^2 and the extracted entropy change for emission is ΔS=4.3±0.2k_B, while due to the absence of a temperature dependent capture cross-section the enthalpy change remains equal to the value extracted from the Arrhenius plot, itself being in very good agreement with the value E_{na}=(0.34±0.02) eV obtained from Hall-effect measurements [36].

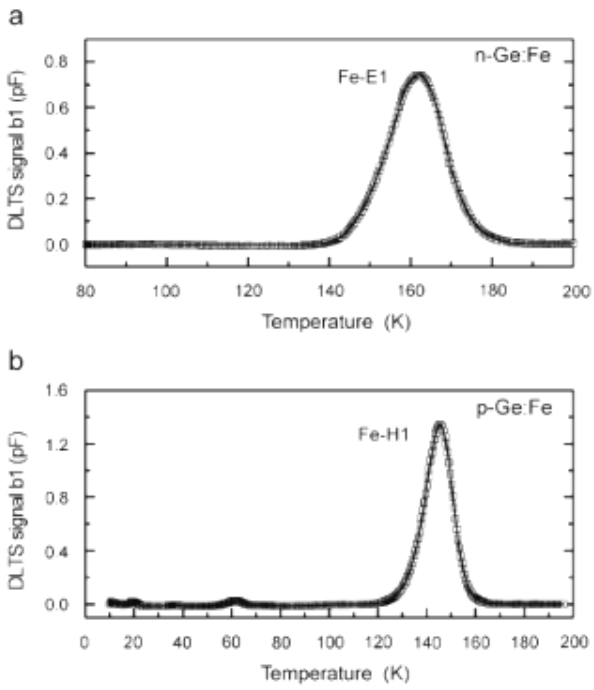

Fig. 1.12. DLTS of Fe-implanted germanium: (a), (b) τ_{ref}=23.5 ms, bias -1 V →-0.01 V, pulse duration 2 ms [1].

All extracted parameters are presented in **Table 1.5.**

Level label	Level assignment	Energy level (eV)	K_T ($s^{-1}K^{-2}$)	σ_{na}/σ_{pa} (cm^2)	σ_∞ (cm^2)	ΔE_σ (eV)	ΔH (eV)	$\Delta S/k_B$
Fe-E1	$Fe_s^{(-/2-)}$	E_c-0.343 (A)	7.6×10^{7}	2.6×10^{-14}	3.4×10^{-15}	0.049	0.294	2.0
Fe-H1	$Fe_s^{(0/-)}$	E_v+0.345 (A)	2.0×10^{9}	2.1×10^{-12}	2.4×10^{-14}			4.3

Table 1.5: Energy levels and assignments of the DLTS bands of Fe-diffused germanium [1]; (A) – acceptor level; (D) – donor level.

In match with the simple model discussed above, Ni is a double acceptor with levels at E_V+0.22 eV and E_C-0.30 eV [23]. The DLTS spectrum for Ni-implanted germanium is shown in **Figure 1.13**. The signatures of Ni–E1 and Ni–H1 are in very good agreement with Hall-effect data [23] and are presented in **Table 1.6**.

Only weak temperature dependence is observed for the cross section of Ni–E1. The corresponding entropy and enthalpy values are also listed in **Table 1.6**. The value of ΔH change is in fair agreement with the energy E_a =0.30 eV observed in Hall-effect measurements [36] and assigned to the $Ni^{(-/2-)}$ transition. The real capture cross section obtained in these measurements and presented in **Table 1.6** is in good agreement with data published by different authors [37-40]. *G. Huylebroeck et al* .[38] obtained $\sigma_n = 4 \times 10^{-18}\ cm^2$ at 165 K from direct capture measurements using Ni-

diffused samples, a much lower value than found in other experiments. It should be mentioned however that the Ni–E1 peak can overlap with Cu–E2 [38], so that a less accurate value of σ_n may be expected. *Wertheim* [39] obtained a value $\sigma_n = 6 \times 10^{-16}\ cm^2$, and *Belyaev* and *Miselyuk* [40] also observed a weak temperature dependence with a value of σ_n in the $10^{-18}\ cm^2$ range.

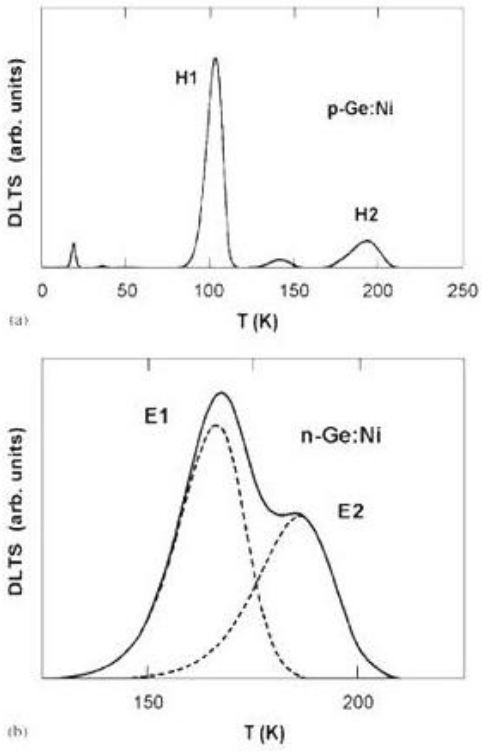

Fig. 1.13. DLTS of Ni-diffused Ge: bias -4 V →-3 V, pulse duration 1 ms, τ_{ref} =6.2 ms; (a) p-type, (b) n-type. Band E2 is due to the presence of Cu [38].

A band Ni–H2 have been assigned to Ni-H complexes [41]. Ni is an efficient lifetime killer in germanium with the Ni–H1 level as the predominant recombination center. The hole capture cross-section σ_{pa} of this trap is too high to be measured directly. These observations are in general agreement with the expected behavior for multiple acceptor centers.

Level label	Level assignment	Energy level (eV)	K_T ($s^{-1}K^{-2}$)	σ_{na}/σ_{pa} (cm^2)	σ_∞ (cm^2)	ΔE_σ (eV)	ΔH (eV)	$\Delta S/k_B$
Ni-E1	$Ni_s^{(-/2-)}$	E_c-0.310 (A)	2.2×10^{7}	7.5×10^{-15}	1.9×10^{-16}	0.001	0.309	3.7
Ni-H1	$Ni_s^{(0/-)}$	E_v+0.217 (A)	2.2×10^{8}	6.2×10^{-13}				

Table 1.6: Energy levels and assignments of the DLTS bands of Ni-diffused germanium [31]; (A) – acceptor level; (D) – donor level.

Ni is the only one species for which a detailed model is available from Electron Spin Resonance (ESR) measurements: the metal atom is displaced from the substitutional lattice position making bonds with two Ge neighbors, while the other two Ge neighbors form a reconstructed bond [42].

The DLTS-spectra of Au diffused *p*- and *n*-type germanium are shown in **Figure 1.14**. The corresponding signatures are listed in **Table 1.7**.

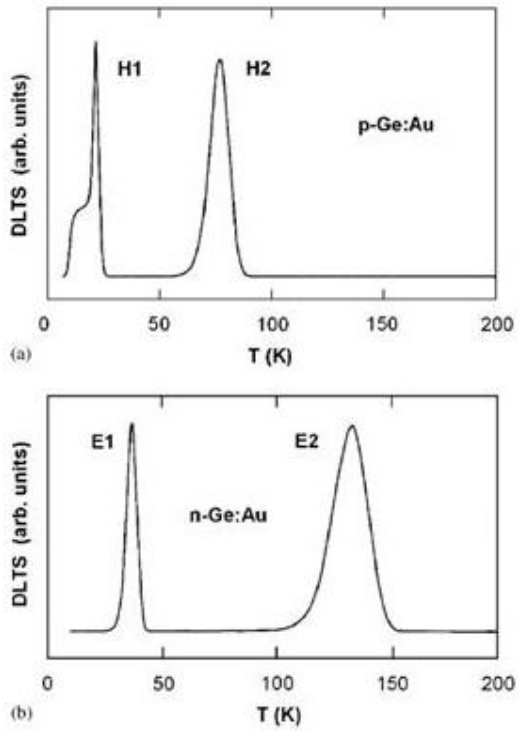

Fig. 1.14. DLTS of Au-diffused Ge: bias -4 V →-3 V, pulse duration 1 ms, τ_{ref} = 6.2 ms; (a) p-type; (b) n-type; [43].

Four bands are observed with concentrations indicating that the corresponding levels very probably belong to the same defect in the gold-doped samples [43, 44].

Level label	Level assignment	Energy level	K_T ($s^{-1}K^{-2}$)	Pearton [45]	Kotina [37]
Au-E2	$Au_s^{(2-/3-)}$	E_c-0.056 eV (A)	2.7×10^6		
Au-E1	$Au_s^{(-/2-)}$	E_c-0.215 eV (A)	1.2×10^6	E_c-0.22 eV (D)	E_c-0.20 eV
Au-H2	$Au_s^{(0/-)}$	E_v+0.135 eV (A)	1.8×10^7	E_v+0.14 eV (A)	E_v+0.15 eV
Au-H1	$Au_s^{(+/0)}$	E_v+0.044 eV (D)	3.9×10^9		

Table 1.7: Energy levels and assignments of the DLTS bands of gold-diffused germanium [43]. The DLTS level corresponds to the signature (E_T, K_T) derived from Arrhenius diagrams. (A) – acceptor level; (D) – donor level.

For Au-E1 and Au-E2 low values of capture cross-sections of the order 10^{-18}–10^{-17} cm^2 are found, as expected for capture of electrons by negatively charged states. All these observations, together with the fair agreement of the E_n values with the energies obtained by Hall-effect leave little doubt that the four DLTS lines in **Figure 1.14** correspond to the single donor and triple acceptor levels of Au_s in germanium.

Despite the fact that each conventional DLTS spectrum, presented in **Figures 1.11 (a)**, **1.12 (a)**, and **1.14 (b)**, consist of the sharp dominant peaks, indicating monoexponential transients related to a single well-defined energy levels, a careful analysis of the state-of-the-art of the literature for Fe, Au, and Cr [1, 4, 30, 31, 38, 43, 46, 47] suggests the presence of a nearby level due to the asymmetry of the corresponding DLTS peaks. This might be guessed from **Figures 1.11 (a)**, **1.12 (a)**, and **1.14 (b)** of *Clauws et al.* [1, 4, 38, 43] displaying asymmetric peaks Cr-E1, Fe-E1 and Au-E2, respectively. FWHM and T_m for each peak in case of Cr-, Fe- and Au-doped *n*-type Ge are listed in **Table 1.8**, clearly demonstrating an asymmetry of the corresponding peaks.

Level label	*FWHM* (K)	T_m (K)
Cr-E1	23	173
Fe-E1	18	162
Au-E2	19	131

Table 1.8: Parameters obtained from conventional DLTS spectra presented on **Figures 1.11 (a)**, **1.12 (a)**, and **1.14 (b)** demonstrating an asymmetry of the corresponding peaks.

For a single, well isolated level in the bandgap, its FWHM should be equal to $\Delta T = 0.1 \times T_m$, which is not the case for all mentioned peaks. Thus for each impurity it is legitimate to expect the presence of a nearby level manifested as a shoulder on the low temperature side of the major peak. The question of the presence of a nearby level should be carefully reviewed with the clarifying of the origin of this level appearance.

Results, concerning Ni-doped *n*-type Ge, presented in **Figure 1.13 (b)**, show the occurrence of Cu in the bandgap and should also be re-exemained.

Summary

To summarize, after a long absence, extending from the late fifties to very recently, germanium is re-emerging owing to its good intrinsic properties as high carrier mobilities and low post-implant thermal budgets. Thus, the use of Ge layers in Si-based field-effect transistors is expected to push the frequency limit much further than what is possible with silicon [48].

For these reasons, point-defects studies in germanium become a necessity. The data collected on germanium often scatter requiring a re-examination, and this task is undertaken by different groups belonging to the defect community [7, 10-13].

Metal impurities, especially transition metals (TM), are among the most unwanted contaminants in most of the group IV semiconductors (Si, Ge and SiGe). They are highly reactive fast diffusers, introducing deep levels in the band gap affecting the life time of minority carriers and thereby the device yield [2]. As for the intrinsic defects, the collected data in Ge are by far much less complete than in Si, and still exhibit some scattering. Fortunately, the quality of the diodes made from germanium crystals has become much better than in the past which helps clarifying the situation. In the defect community, the Gent/IMEC group has undertaken the most recent and thorough studies on metallic impurities in germanium mainly via the very sensitive Deep Level Transient Spectroscopy (DLTS) technique [1, 2, 4, 30, 31, 38, 43, 46, 47] .

Also for the metallic species a clear cut exist between Si and Ge. Whereas in Si these impurities prefer interstitial sites, they are found to stabilize in substitutional sites in Ge, forming predominantly multiply-charged acceptor centers, introducing thus several deep levels in the band gap. The reason for that is that in Ge the formation energy of the vacancy is smaller than that of the self-interstitial [13]. It is also much smaller than the formation energy of the vacancy in Si [49]. Therefore, diffusion processes in Ge are mainly mediated by vacancies leading to a preferential stabilization in substitutional sites for the diffusing species. As a consequence, the valence electrons of the impurity in Ge are involved in the local bonding, allowing acceptor states to prevail. It is thus highly likely that the vacancy model developed by *Watkins* holds for TMs in Ge [24]. It was actually already in the late fifties that such a simple picture was proposed and turned out to work remarkably well. *Tyler* and *Woodbury* [23, 27] suggested that the multi-acceptor states induced by transition metals in germanium resulted from their tendency to complete the tetrahedral bonding arrangement with the four nearest germanium atoms.

In this respect, Au ($6s^1$), Cr ($4s^1$), Ni ($4s^2$) and Fe ($4s^2$), the four metals dealt with in the present work, are expected to introduce triple, for the first two, and double acceptor states, for the last two species. This has clearly been shown by *Gent/IMEC Group* [1-4, 31, 47] with the exception that for chromium and gold, a fourth donor level seems to merge next to the triple acceptor state [4, 43].

A striking feature, however, is that for Cr, Fe and Au, the corresponding DLTS peaks recorded in *n*-type germanium display clearly asymmetry and seem to result from a composite peak including a main peak and a shoulder on its low-temperature side. Thus the question – these shoulders, if they exist at all, are due to sample processing or linked to the metallic impurities – initiates the present work. For Ni-doped Ge the situation confirming the presence of copper in the band gap, scatters, requiring also a re-examination.

Bibliography

1. Clauws, P., et al., *Deep level transient spectroscopy of transition metal impurities in germanium.* Physica B: Condensed Matter, 2007. **401-402**(0): p. 188-191.
2. Simoen, E. and C. Claeys, *Chapter 5 - Metals in germanium*, in *Germanium-Based Technologies*2007, Elsevier: Oxford. p. 131-185.
3. Clauws, P. and J. Lauwaert, *Electronic Properties of Transition Metal related Defects in Germanium*, in *The 5th International Symposium on Advanced Science and Technology of Silicon Materials (JSPS Si Symposium)*2008: Kona, Hawaii, USA.
4. Lauwaert, J., et al., *Electronic properties of titanium and chromium impurity centers in germanium.* Journal of Applied Physics, 2009. **105**(7): p. 073707-6.
5. http://www.ioffe.rssi.ru/SVA/NSM/Semicond/Ge/bandstr.html.
6. Macfarlane, G.G., et al., *Fine Structure in the Absorption-Edge Spectrum of Ge.* Physical Review, 1957. **108**(6): p. 1377-1383.
7. Giese, A., N.A. Stolwijk, and H. Bracht, *Double-hump diffusion profiles of copper and nickel in germanium wafers yielding vacancy-related information.* Applied Physics Letters, 2000. **77**(5): p. 642-644.
8. Werner, M., H. Mehrer, and H.D. Hochheimer, *Effect of hydrostatic pressure, temperature, and doping on self-diffusion in germanium.* Physical Review B, 1985. **32**(6): p. 3930-3937.
9. Fuchs, H.D., et al., *Germanium ^{70}Ge/^{74}Ge isotope heterostructures: An approach to self-diffusion studies.* Physical Review B, 1995. **51**(23): p. 16817-16821.
10. Simoen, E. and C. Claeys, *Chapter 2.2. - Intrinsic Point Defects in Germanium*, in *Germanium-Based Technologies: From Materials to Device*2007, Elsevier Ltd: London.
11. Mayburg, S., *Vacancies and Interstitials in Heat Treated Germanium.* Physical Review, 1954. **95**(1): p. 38-43.
12. Tweet, A.G., *Precipitation of Cu in Ge.* Physical Review, 1957. **106**(2): p. 221-224.
13. Vanhellemont, J., et al., *On the solubility and diffusivity of the intrinsic point defects in germanium.* Journal of Applied Physics, 2007. **101**(3): p. 036103-3.
14. Vanhellemont, J. and E. Simoen, *Brother Silicon, Sister Germanium.* Journal of The Electrochemical Society, 2007. **154**(7): p. H572-H583.
15. Sueoka, K. and J. Vanhellemont, *Ab initio studies of intrinsic point defects, interstitial oxygen and vacancy or oxygen clustering in germanium crystals.* Materials Science in Semiconductor Processing, 2006. **9**(4-5): p. 494-497.
16. Fage-Pedersen, J., A.N. Larsen, and A. Mesli, *Irradiation-induced defects in Ge studied by transient spectroscopies.* Physical Review B, 2000. **62**(15): p. 10116-10125.
17. Lindberg, C.E., et al., *The antimony-vacancy defect in p-type germanium.* Applied Physics Letters, 2005. **87**(17): p. 172103-3.
18. Mesli, A., et al., *Low-temperature irradiation-induced defects in germanium: In situ analysis.* Physical Review B, 2008. **78**(16): p. 165202.

19. Kolkovsky, V., et al., *Gallium interstitial in irradiated germanium: Deep level transient spectroscopy.* Physical Review B, 2008. **78**(23): p. 233201.

20. Kolkovsky, V., et al., *Low-temperature irradiation-induced defects in p-type germanium.* Physical Review B, 2010. **81**(3): p. 035208.

21. Christian Petersen, M., A. Nylandsted Larsen, and A. Mesli, *Divacancy defects in germanium studied using deep-level transient spectroscopy.* Physical Review B, 2010. **82**(7): p. 075203.

22. Haller, E.E., W.L. Hansen, and F.S. Goulding, *Physics of ultra-pure germanium.* Advances in Physics, 1981. **30**(1): p. 93-138.

23. Tyler, W.W., *Deep level impurities in germanium.* Journal of Physics and Chemistry of Solids, 1959. **8**(0): p. 59-65.

24. Watkins, G.D. and P.M. Williams, *Vacancy model for substitutional Ni^{-}, Pd^{-}, Pt^{-}, and Au^{0} in silicon.* Physical Review B, 1995. **52**(23): p. 16575-16580.

25. Silva, E.L., et al., *Electronic structure of Zn, Cu and Ni impurities in germanium.* Journal of Physics: Condensed Matter, 2011. **23**(6): p. 065802.

26. Lerner, L. and N.A. Stolwijk, *Radiotracer diffusion of cobalt, iron, and chromium in dislocation-free germanium.* Applied Physics Letters, 2008. **93**(3): p. 032107-3.

27. Woodbury, H.H. and W.W. Tyler, *Triple Acceptors in Germanium.* Physical Review, 1957. **105**(1): p. 84-92.

28. Continenza, A., G. Profeta, and S. Picozzi, *Transition metal impurities in Ge: Chemical trends and codoping studied by electronic structure calculations.* Physical Review B, 2006. **73**(3): p. 035212.

29. Decoster, S., et al., *Transition Metal Impurities on the Bond-Centered Site in Germanium.* Physical Review Letters, 2009. **102**(6): p. 065502.

30. Forment, S., et al., *A deep-level transient spectroscopy study of transition metals in n-type germanium.* Materials Science in Semiconductor Processing, 2006. **9**(4-5): p. 559-563.

31. Lauwaert, J. and P. Clauws, *Majority carrier capture rates for transition metal impurities in germanium.* Thin Solid Films, 2010. **518**(9): p. 2330-2333.

32. Simoen, E., et al., *Lifetime and leakage current considerations in metal-doped germanium.* Journal of Materials Science: Materials in Electronics, 2007. **18**(7): p. 799-804.

33. Conwell, E.M., *Properties of silicon and germanium: II*, in *Proceedings of the IRE* 1958. p. 1281 - 1300

34. Frenkel, J., *On Pre-Breakdown Phenomena in Insulators and Electronic Semi-Conductors.* Physical Review, 1938. **54**(8): p. 647-648.

35. Belyaev, A.D. and V.G. Malogolovets, *Effective cross section for electron capture by negative iron ions in germanium.* Soviet phyiscs, Solid state, 1964. **5**(10): p. 2229.

36. Tyler, W.W. and H.H. Woodbury, *Properties of Germanium Doped with Iron. I. Electrical Conductivity.* Physical Review, 1954. **96**(4): p. 874-882.

37. Kotina, I.M., et al., *Capacitance spectroscopy of deep Cu, Au, Ag, and Ni centers in germanium.* Soviet physics semiconductors, 1987. **21**(6): p. 635.

38. Huylebroeck, G., et al., *DLTS of nickel impurities in germanium.* Solid State Communications, 1992. **82**(5): p. 367-369.

39. Wertheim, G.K., *Recombination Properties of Nickel in Germanium.* Physical Review, 1959. **115**(1): p. 37-47.

40. Belyaev, A.D. and E.G. Miselyuk, *Electron recombination at negative ions of nickel in germanium.* Soviet physics-solid state, 1964. **6**(9): p. 2101.

41. Zach, F.X., Hermann G. Grimmeiss, and E.E. Haller, *Nickel Related Deep Levels in Germanium.* Materials Science Forum (Volumes 83 - 87), 1992. **Defects in Semiconductors 16**: p. 245-250.

42. Ludwig, G.W. and H.H. Woodbury, *Electron Spin Resonance in Nickel-Doped Germanium.* Physical Review, 1959. **113**(4): p. 1014-1018.

43. Simoen, E., et al., *DLTS of gold impurities in germanium.* Semiconductor Science and Technology, 1987. **2**(8): p. 507.

44. Huylebroeck, G., et al., *DLTS of silver in germanium: evidence for an amphoteric impurity.* Semiconductor Science and Technology, 1989. **4**(7): p. 529.

45. Pearton, S.J., Solid-State Electronics, 1982. **25**(305).

46. Clauws, P. and E. Simoen, *Metals in germanium.* Materials Science in Semiconductor Processing, 2006. **9**(4-5): p. 546-553.

47. Clauws, P. and J. Lauwaert, *Electronic Properties of Transition Metal related Defects in Germanium*, in *The 5th International Symposium on Advanced Science and Technology of Silicon Materials (JSPS Si Symposium)*2008: Kona, Hawa.

48. Chui, C.O., et al., *Germanium n-type shallow junction activation dependences.* Applied Physics Letters, 2005. **87**(9): p. 091909-3.

49. Lauwaert, J., et al., *Simulation of point defect diffusion in germanium.* Physica B: Condensed Matter, 2006. **376–377**(0): p. 257-261.

DEPLETION LAYER CAPACITANCE SPECTROSCOPY

CHAPTER II. DEPLETION LAYER CAPACITANCE SPECTROSCOPY.

2.1. METAL-SEMICONDUCTOR JUNCTION.

Electronic transport based analysis require test devices such as *Schottky* barriers or *p-n* junctions. As will be shown in this chapter, carrier capture and emission processes at deep levels need to be separated in time and space to enable extracting physical parameters. The present chapter is divided in three sections. The first part is devoted to the basics of an ideal Schottky barrier. In a second section a deep level is introduced in the band gap to see how the capture-emission processes affect the behavior of the Schottky barrier. Then, in third section the principle of transient capacitance and its relation to DLTS and Laplace DLTS are described.

2.1.1 Schottky model

It is essential to start by introducing the model describing the electrical contact between metal and semiconductor (*n*-type material in the present case) in the absence of surface states, proposed by *Schottky* in 1942. The various techniques used in this work are all based on such a simple device, justifying thus a brief description [1]. The structure of a device is presented in **Figure 2.1.**

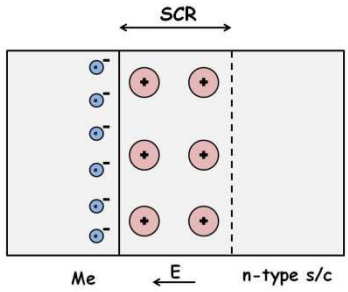

Fig. 2.1. The formation of SCR in Schottky diode.

Immediately after the two materials have been brought into intimate contact, electrons are transferred from the semiconductor to the metal, leading to the equalization of their respective Fermi levels E_F throughout the whole structure. The resulting excess of negative charge in the metal close to the surface is determined by the excess of electrons within the free carrier screening length x_m (~0.5Å). In the *n*-type semiconductor positive charges (ionized donors) are left and their amounts correspond to the concentration of electrons that have escaped the semiconductor. This mechanism leads to a local violation of charge neutrality in the vicinity of the interface. The layer depleted from free carriers is referred to the “depletion region” or space charge region (SCR), where an electric field builds-up inducing a curvature

of the energy bands. We consider the case $x_m \ll x_d$, where x_d is the depletion width, extending mainly in the semiconductor.

According to the model developed by *Schottky* [2] the energy band diagram is constructed by reference to the vacuum level. We consider an ideal contact between the metal and the semiconductor with the condition $\Phi_s < \Phi_m$, where Φ_m and Φ_s are the respective work functions[1] [3]. Under thermal equilibrium the Fermi levels E_F in both materials should coincide. Due to continuous vacuum level, a step between Fermi level of the metal and the conduction band of the semiconductor, known as potential barrier Φ_b, is formed and given by

$$\Phi_b = \Phi_m - \chi_s, \tag{2.1}$$

where χ_s is the electron affinity[2] of the semiconductor. The formation of a Schottky barrier Φ_b for n-type semiconductor is graphically illustrated in **Figure 2.2**. The band bending in the metal eV_m is negligibly small due to the large electron density in this material.

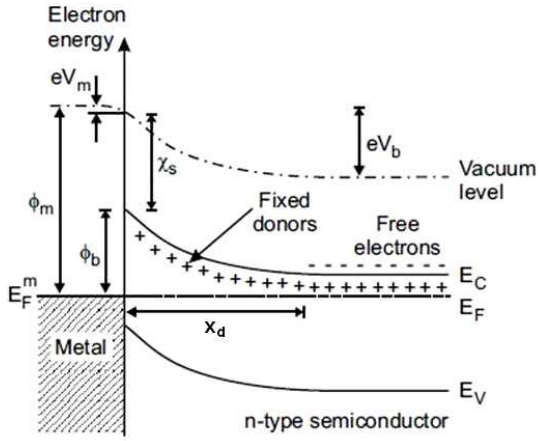

Fig. 2.2. Energy-band diagram of a metal-n-type semiconductor Schottky barrier [4].

The zero bias conditions, where there is no net flow of electrons over the barrier, corresponding to the thermal equilibrium mentioned above, are described by the built-in potential

$$eV_b = \Phi_b - (E_c - E_F), \tag{2.2}$$

[1] The work function is the minimum energy needed to remove an electron to liberate it from an initial energy at Fermi level to a point immediately outside the solid surface in metal-vacuum system.

[2] The electron affinity of a semiconductor is the energy released when and electron is added to the material, i.e. the distance measured from the bottom of the conduction band E_c to the vacuum level.

where $(E_c - E_F)$ is the energy difference between conduction band and Fermi level in neutral semiconductor.

By applying an external bias V_a across the barrier, it is possible to modify the potential barrier height and the electric field in the SCR of the semiconductor. Under reverse bias V_r the Fermi level of semiconductor is lowered, increasing the barrier for electrons and enlarging the depletion width x_d. Under forward bias V_f the position of the Fermi level in the semiconductor is raised relative to that in the metal, leading to a decrease of the barrier and a shrinkage of the depletion width x_d.

In any material with a spatially distributed space charge a link between the electrostatic potential ψ and the electric field is extracted from the *Poisson equation*, which can be written in the one-dimensional case as

$$\frac{d^2\psi}{dx^2} = \frac{1}{\varepsilon_0 \varepsilon_s}\rho(x), \tag{2.3}$$

where $\rho(x)$ is the charge density in semiconductor at a depth x, ε_s is the relative dielectric constant of the semiconductor material, ε_0 is the permittivity of the vacuum.

The charge density in the SCR is determined by the net charge of ionized donor density N_d, so the charge density in the semiconductor can be written as

$$\rho(x) = \begin{cases} eN_d\,, & if\ x \le x_d \\ 0, & if\ x > x_d \end{cases}. \tag{2.4}$$

By integrating **Equation 2.3** twice and applying the boundary conditions of vanishing band bending at the edge of the depletion region, we obtain the depletion width

$$x_d = \sqrt{\frac{2\varepsilon_0 \varepsilon_s}{eN_d} V}, \tag{2.5}$$

where $V = (V_b - V_a)$.

In accordance with the Poisson equation the electric field increases linearly from the edge of the depletion region towards the metal, reaching a maximum in the metal interface according to

$$E(x) = -\frac{eN_d(x_d - x)}{\varepsilon_0 \varepsilon_s}. \tag{2.6}$$

And the electrostatic potential decreases quadratically according to

$$V(x) = -\frac{eN_d}{2\varepsilon_0 \varepsilon_s}(x_d - x)^2. \tag{2.7}$$

The capacitance associated with the depletion region arises from the immobile donors in SCR, known as the depletion capacitance. Any system where electrical charge Q is changed due changing the potential V induces a capacitance, which is determined as $C = \left|\frac{\delta Q}{\delta V}\right|$. The space charge per unit area of semiconductor is given by

$$Q_d = ex_d N_d = \sqrt{2e\varepsilon_0\varepsilon_s N_d V} \tag{2.8}$$

from which the capacitance of the barrier follows by applying the *Gauss's* law

$$C = \sqrt{\frac{\varepsilon_0\varepsilon_s e N_d}{2V}} = \frac{\varepsilon_0\varepsilon_s}{x_d} \tag{2.9}$$

Taking into account the infinitesimal analysis, **Equation 2.9** can be written in the form

$$\frac{\varepsilon_0\varepsilon_s}{eN_d(x)} = x \cdot \frac{\delta x}{\delta V} = x \cdot \frac{\delta x}{\delta C} \cdot \frac{\delta C}{\delta V} = \frac{(\varepsilon_0\varepsilon_s)^2}{C^3} \cdot \frac{\delta C}{\delta V} = \frac{(\varepsilon_0\varepsilon_s)^2}{2} \cdot \frac{\delta}{\delta V}\left(\frac{1}{C^2}\right), \tag{2.10}$$

which leads to determination of apparent doping concentration

$$N_d\big(x(V)\big) = \frac{2}{\varepsilon_0\varepsilon_s e}\left(\frac{d(1/C^2)}{dV}\right)^{-1} \tag{2.11}$$

If N_d is constant throughout the depletion region, the plot of $1/C^2$ versus V gives a straight line. From the intercept on the voltage axis the barrier height can be determined.

The current-voltage characteristic of a rectifier contact is given by

$$I = I_s\left[exp\left(\frac{eV - IR_s}{nk_BT}\right) - 1\right], \tag{2.12}$$

where $I_s = AA^{**}T^2 exp\left(-\frac{e\Phi_b}{k_BT}\right)$ is the saturation current, a device parameter, specified by diode area A, Richardson constant A^{**}; n is the ideality factor. In **Equation 2.12** R_s represents the series resistance which for an ideal Schottky barrier is equal to zero.

I-V characteristic of Schottky diode has a pronounced asymmetric behavior, which is typical for barrier structures. The current in Schottky barrier is conditioned by the majority carriers – electrons in the present case. The role of an external voltage consists of changing the number of electrons, moving across the depletion region.

In consideration of the case when $V \gg k_B T/e$, the ideality factor can be obtained from

$$n = \frac{e}{k_B T \frac{d \ln I}{dV}} \tag{2.13}$$

This quantity is equal to unity for an ideal Schottky barrier. From *I-V* characteristic all these important features like the turn-on voltage and the break-down voltage can be extracted. From the temperature dependence of the *I-V* characteristics, the barrier height of the junction can be also extracted.

2.1.2 Schottky diode with deep level in the bandgap

The presence of a defect in the semiconductor may induce more than one level in the bandgap [4]. The ability of these levels to trap free carriers leads to a change of the charge states with the consequence of a modification of the capacitance of the SCR.

The simplest approach is to consider a single deep level – a carrier trap – with two charge states in the bandgap. This level will communicate via carrier transitions with either the conduction band E_c or the valance band E_v. The four most common processes that define the dynamic behavior of such level – electron and hole emission and capture – are illustrated in **Figure 2.3**. The capture processes are characterized by capture cross section, σ_n – for electrons and σ_p – for holes.

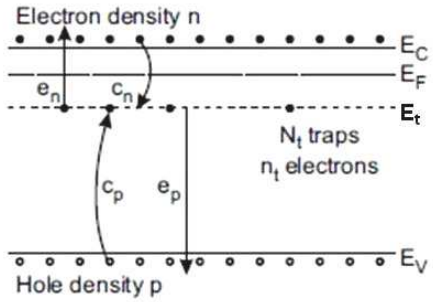

Fig. 2.3. Schematic representation of transitions of carriers between a deep center with energy level E_t.

To achieve the complete knowledge of parameters related to a defect under study, we analyze the kinetics of filling and emptying these levels with free electrons and holes.

Due to the emission and capture of carriers, the concentration of occupied traps will change according to kinetic equation

$$\frac{dn_t}{dt} = \big(e_p + c_n\big)(N_t - n_t) - (e_n + c_p)n_t, \tag{2.14}$$

where e_n and e_p are the rates of electron and hole emission, and c_n and c_p are the rates of electron and hole capture. N_t is the total concentration of traps and (N_t – n_t) represent those which are not occupied.

The solution of this linear **equation 2.14** is an exponential function with a time constant equal to the sum of reciprocal rates of all participating processes. It is given by

$$n_t(t) = n_t(\infty) + [N_t(0) - n_t(\infty)]\exp\,[-(c_n + e_p + c_p + e_n)t], \tag{2.15}$$

where $n_t(\infty) = \frac{c_n + e_p}{c_n + e_p + c_p + e_n} N_t$ is the equilibrium concentration of the occupied trap for which $dn_t/dt=0$.

For the case under consideration – an electron trap in the depletion region – the emission rate e_n dominates all the other emission and capture rates, so the trap concentration as a function of time is given by

$$n_t(t) = N_t \exp\,(-e_n t) \tag{2.16}$$

The width of the SCR connected by relation with the depletion capacitance can be registered directly through the changing of electrical charge Q in this region due to the changing of potential V. The space charge per unit area of semiconductor is given by

$$Q_d = ex_d\big(N_d + N_t - n_t(t)\big). \tag{2.17}$$

Substituting **expression (2.5)** in **(2.17)** and applying the Gauss's law the depletion capacitance can be obtained.

Provided the condition that $N_t \ll N_d$ is fulfilled, where N_t is the total concentration of electron traps and N_d is the constant dopant concentration, the time dependent barrier capacitance related to the carrier emission from the trap is given by

$$C(V) = C_\infty(V) + \Delta C(V) = C_\infty(V)\sqrt{\frac{N_t - n_t}{N_t}} \approx C_\infty(V)\left(1 - \frac{n_t}{2N_t}\right), \tag{2.18}$$

where $C_\infty = \sqrt{\frac{\varepsilon_0 \varepsilon_s e(N_d+N_t)V}{2}}$ is the steady-state capacitance of the diode, when the traps are empty.

The process of time separation between the capture and emission processes, achieved by pulsing the applied bias, is illustrated in **Figure 2.4**.

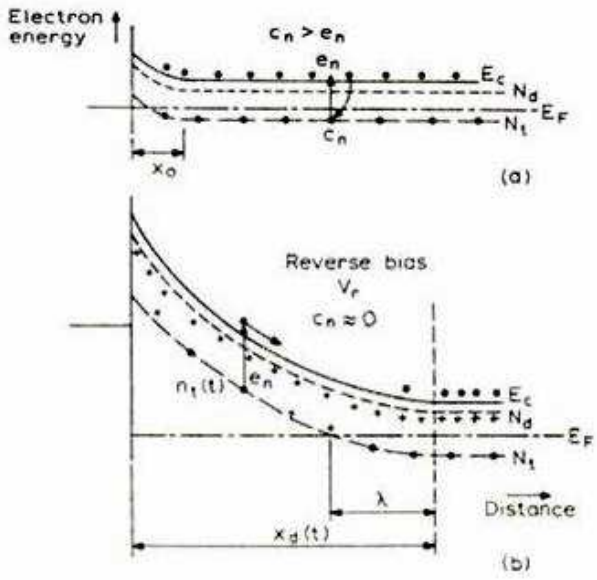

Fig. 2.4. A Schottky contact on n-type semiconductor (a) at low bias and (b) under the reverse bias V_r.

The change in capacitance leads to the concentration of trapped electrons and is given by the relation

$$\frac{\Delta C(V)}{C_\infty(V)} = \frac{n_t}{2N_t}. \tag{2.19}$$

If the level has been saturated by applying large filling pulse ($t_F = \infty$), then $n_t(\infty) = N_t$ which is the total concentration of the defect.

2.2. PRINCIPLE OF THE TRANSIENT SPECTROSCOPY METHODS

As shown above the use of a depletion region of a Schottky barrier makes possible the separation process of emission and capture of carriers, allowing extracting various physical parameters of the deep levels in semiconductor bandgap. All these parameters form the so-called *signature* of the defect under study and are recalled below.

For any transition (see **Figure 2.3**) the emission and capture rates for any carrier type are governed by detailed balance principle. At the same time, the occupancy of a trap in thermal equilibrium conditions is described by Fermi-Dirac statistics and as a result electron emission is given by [4]

$$e_n(T) = c_n \frac{g_{i-1}}{g_i} exp\left(\frac{E_t - E_F}{kT}\right) = \gamma T^2 \sigma_{na} exp\left(-\frac{E_c - E_t}{kT}\right), \quad (2.20)$$

where we use the following notations: $\gamma = 2\sqrt{3}(2\pi)^{\frac{3}{2}} k^2 m^* h^{-3}$, m^* is the majority carrier effective mass, g_{i-1} and g_i are the degeneracies for the state empty and filled respectively, $\sigma_{na} = \sigma_\infty \frac{g_{i-1}}{g_i}$. Exchanging g_{i-1} and g_i, while replacing the subscript n by p, results in the corresponding equation for holes.

Here the temperature dependence of the capture cross section is taken into account

$$\sigma_{na}(T) = \sigma_\infty exp\left(-\frac{\Delta E_\sigma}{kT}\right). \quad (2.21)$$

Inserting **Equation 2.21** into **Equation 2.20** and using the *Gibbs* free energy $\Delta G = \Delta H - T\Delta S$, with ΔH being the enthalpy and ΔS the entropy following the ionization of the defect, the *apparent activation enthalpy* E_{na} and the *apparent capture cross section* σ_{na} (extrapolated to $T=\infty$) can be extracted from a plot of $ln(e_n/T^2)$ versus $1/T$

$$E_{na} = (E_c - E_t) + \Delta E_\sigma = \Delta H + \Delta E_\sigma \quad (2.22)$$

$$\sigma_{na}(T) = \sigma_\infty \frac{g_{i-1}}{g_i} exp\left(\frac{\Delta S}{k}\right). \quad (2.23)$$

Together these two parameters gives the *electronic signature* that is associated with particular transition, i.e. level, in the bandgap and a plot of ln (e_n/T^2) versus $1/T$ is usually named *Arrhenius plot*.

The basis of transient spectroscopy methods such as DLTS, MCTS and Laplace DLTS is a concept of the capacitance relaxation of the structure with a potential barrier.

2.2.1. Capacitance transient

As mentioned above, the change in capacitance, when the trap is emitting trapped electrons, is given by the time dependent equation

$$C(e_n(T), t) = C_\infty + \Delta C_0 exp(-e_n(T)t), \tag{2.24}$$

where ΔC_0 is the capacitance transient amplitude and it is illustrated in **Figure 2.5 (c)** and $C(e_n(T), t) - C_\infty = \Delta C(e_n(T), t)$.

In transient spectroscopies, deep levels within the depletion region are first filled during capture process and in a subsequent step these deep traps emit the carriers. These two processes are repeated in time while the temperature is scanned. The resulting capacitance transient due to the emission of electron in n-type semiconductor is schematically represented in **Figure 2.5** where the various steps of filling and empting are illustrated.

In a Schottky barrier as in asymmetric *p-n* junction under reverse bias the width of the depletion region x_d is large. Any trap present in SCR will not be populated at thermal equilibrium since no mobile charge carriers are available for capture. This is schematically presented in **Figure 2.5 (a)** as **step 1**. The structure can be regarded as a parallel-plate capacitor with a capacitance *C*.

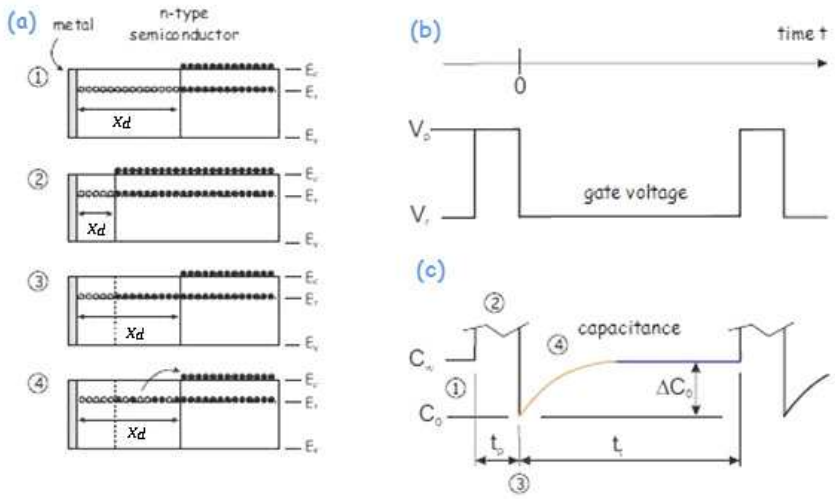

Fig. 2.5. (a) The capacitance transient due to the presence of a deep energy level in an *n*-type semiconductor (b) voltage-pulse sequence and (c) the corresponding capacitance function in periodic DLTS cycle.

A short filling pulse, applied across the diode results in the immediate reduction of the depletion region illustrated as **step 2** which leads to the filling of the trap by majority carriers. The decrease of the depleted width x_d results in an increase of the capacitance, as shown on the **Figure 2.5 (c)**. After the system returns to the reverse bias condition as shown in **Figure 2.5 (a) – step 3**, the capacitance value becomes lower than the original value C due to trapped carriers. If the trap is allowed to emit captured carriers – see **Figure 2.5 (a) – step 4** - an exponential transient in the capacitance takes place, a relaxation process represented by **Equation 2.24** in which an essential part of the finger print is contained in the time constant $e_n(T)$.

$$C(t) = C_\infty + \Delta C_0 exp\left(-\frac{t}{\tau_{tr}}\right), \tag{2.25}$$

where $\tau_{tr} = e_n^{-1}$.

2.2.2. Deep level transient spectroscopy (DLTS)

The capacitance transient shown in **Figure 2.5** has a characteristic time constant τ_{tr}, equal to the inverse of the emission rate of the deep level.

In **Figure 2.5 b** and **c** the principle of DLTS method, devised by *Lang* [5], is briefly introduced. Voltage pulses V_p of duration t_p are periodically applied to the Schottky contact in order to charge with majority carriers the trap located in semiconductor bandgap ($t < 0$). At $t = 0$ the bias of the Schottky diode switches back to the reverse voltage V_r at which the deep level is raised above the semiconductor quasi-Fermi level E_F. Thus the measured capacitance change defined by **Equation 2.24** reflects the time evolution of the level occupation driven by the carrier emission rate [5-7].

From the capacitance transient the extraction of the emission rate $e_n = 1/\tau_n$, where $e_n = e_n(T)$ is given by **Equation 2.20**, and τ_n is the relaxation time, can be achieved using several fitting procedures among which the single exponential fit in the simplest case, double-boxcar [4] or lock-in deconvolution and Laplace transform [7].

Figure 2.6 illustrates the simplest method based on double box-car (**DB**) deconvolution by performing a *temperature scan* of the diode. It aims at picking the capacitance at two different instants t_1 and t_2 and recording the difference $(\Delta C(e_n(T), t_2) - \Delta C(e_n(T), t_1)$. The blue and red dashed vertical lines denote the times t_1 and t_2 for two different rate windows, respectively. For simplicity, instrument recovery and gate-off times have been neglected [4].

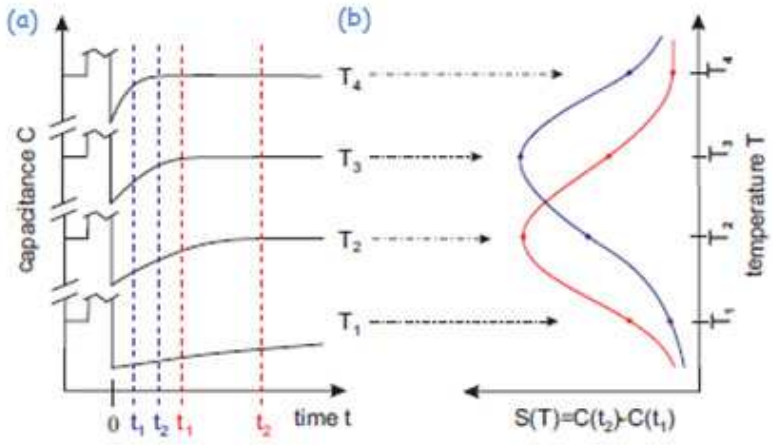

Fig. 2.6. Evaluation of capacitance transient with double box-car filter: (a) capacitance transient at various temperatures and (b) DLTS signal *S(T)* obtained at corresponding temperatures.

The temperature dependent DLTS spectrum is recorded as a difference of the capacitance transient at times t_1 and t_2

$$S(T) = C(t_1) - C(t_2) = -\Delta C[\exp(-e_n \times t_1) - \exp(-e_n \times t_2)]. \qquad (2.26)$$

It is easily shown that the large DLTS signal is observed if the time DLTS constant τ_r in the capacitance transients becomes equal to the reference time constant or experimental rate window [4]

$$\tau_{ref} = \frac{(t_2 - t_1)}{ln\frac{t_2}{t_1}}. \qquad (2.27)$$

Thus, a maximum of DLTS spectrum occurs at the temperature T_m, at which the relaxation time τ_r becomes equal to the reference time

$$\tau_r = \tau_{ref} = e_n^{-1}. \qquad (2.28)$$

As shown in **Figure 2.6** setting different values of t_1 and t_2, and thus τ_{ref}, allows the DLTS peak to shift. A new maximum is obtained at a different temperature T_m. Assuming an exponential dependence of the signal, the reference-time dependence of T_m is used in Arrhenius analysis corrected by T^2 to obtain the deep level *signature*:

$$\ln(\tau_{ref} T_m^2) = -\ln(\sigma_a \gamma_n) + \frac{E_a}{kT_m}. \qquad (2.29)$$

From the slope of logarithmic plot of $ln(\tau_{ref} T_m^2)$ versus the inverse temperature of DLTS maximum $1/T_m$ and its intersection with the ordinate at the value $1/T_m=0$ the apparent activation enthalpy ΔH and the apparent capture cross section σ_{na} can be

obtained separately. A linear behavior is expected if the emission is dominated by a single thermally activated process. In case of several emission paths, such as competing tunneling processes $ln(\tau_{ref}T_m^2)$ versus the inverse temperature of DLTS maximum $1/T_m$ exhibits a nonlinear character.

2.2.3. Influence of electric field on the barrier height

When the thermal emission rate is strongly electric field dependent, nonexponential transients can be observed due to the variation of the electric field in SCR. In the simplest case of the *Poole-Frenkel* (**PF**) effect this field-enhanced emission of carriers is taken as indication that the defect is ionized and has a charge state opposite to the emitted carrier.

Generally speaking, the presence of an electric field ξ tilts the band structure, which may lead to three mechanisms of emission enhancement such as the *PF* effect, the phonon-assisted tunneling or the direct tunneling, illustrated in **Figure 2.7**. Below we focus on the case where the tunneling is negligible and thus the only effect would be a distortion of the coulombic potential of the defect, known as the *PF* effect.

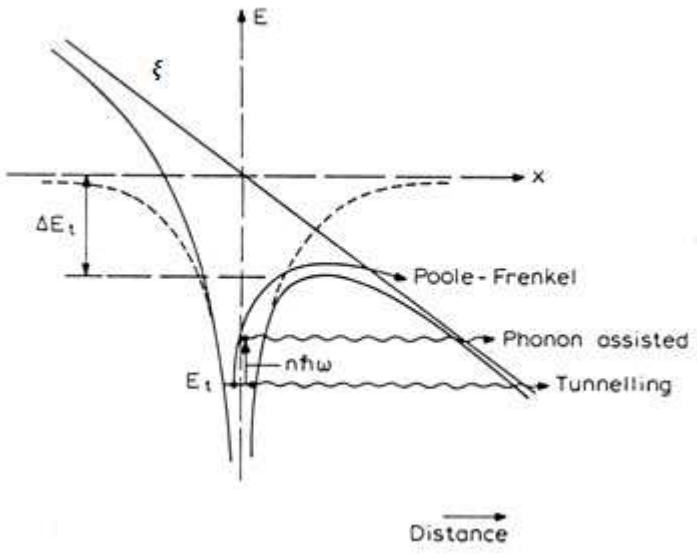

Fig. 2.7. Potential barrier for the emission at a deep-level defect in external electric field ξ. The arrows show different ionization processes [4].

The *PF* effect describes the increase of the thermal emission rate of carriers in an external electric field ξ due to the lowering of a barrier height by the energy ΔE_t, associated with *Coulombic* potential. The original theory was developed by *Frenkel* in 1938 [8] showing that in the one dimension case the emission rate is increased by the lowering of the barrier according to

$$e_n(\xi) = e_{n0}\exp\left(\Delta E_t(\xi)/kT\right), \tag{2.30}$$

with

$$\Delta E_t(\xi) = \frac{1}{2}\sqrt{\frac{Ze^3\xi}{\varepsilon_s}}, \tag{2.31}$$

where Z is the absolute charge of the center, e is the electron charge, ε_s is the dielectric constant, e_{n0} is the emission rate in zero field. The relation between ΔE_t and ξ depends upon the form of the potential which binds the carrier. It can be clearly seen from **Equation 2.30**, that if $\Delta E_t = 0$, no field effect is given and $e_n(\xi) = e_{n0}$.

Equation 2.31 yields an exponential increase of the ionization probability with the square root of the electric field.

Phonon assisted tunneling is possible for impurities in all charge states – charged and neutral. The numerical studies for this effect were developed by *Makram-Ebeid* and *Lanoo*[9] leading to

$$e_n(\xi)/e_n(0) = \exp\left(\frac{\xi^2}{E_c^2}\right), \tag{2.32}$$

where

$$E_c = \sqrt{\frac{3m^*h}{e^2\tau_2^3}} \tag{2.33}$$

and

$$\tau_2 = \frac{h}{2kT} \mp \tau_1, \tag{2.34}$$

where the signs (-) and (+) correspond to the adiabatic potential structures of auto localized centers and substitutional impurities, respectively and τ_1 is the time constant.

We can see from the equations above that the dependence of emission rate on electric field is given by $\ln(e_n) \propto \sqrt{\xi}$ in case of *PF* effect, while in the case of phonon assisted tunneling the electric field dependence is given by $\ln(e_n) \propto \xi^2$. The knowledge of details of the mechanisms of field-enhanced emission, including barrier lowering, can be used to probe the nature of the defects and helps to distinguish between donor and acceptor in standard methods of deep levels analysis – DLTS, MCTS and Laplace DLTS. Substitution **Equations 2.30** and **2.31** to **Equations 2.24** and **2.25** allows establishing the link between the field dependence and the shape and position of the DLTS spectra as illustrated in **Figure 2.8**.

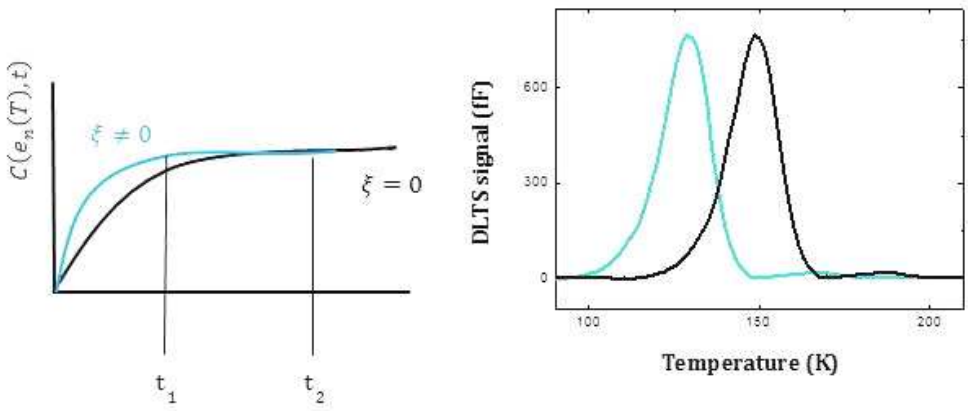

Fig. 2.8. Evaluation of the capacitance transient (blue) in presence and (black) without Poole-Frenkel effect and DLTS signal *S(T)* in *n*-type Ge.

The Poole-Frenkel effect applies only to donor-like electron traps and acceptor-like hole traps (states that are neutral when they are occupied and charged when they are empty). Detecting the Poole-Frenkel effect establishes thus an important characteristic of a defect.

2.2.4. Laplace DLTS

In several circumstances, DLTS produces broad, relatively featureless spectra that are difficult to interpret in terms of precise energetic relationships [7]. The most difficult issue in DLTS is that noise sets the fundamental limit in the extraction of time constants. The ability to distinguish close energy levels in the band gap, the dynamic range of transient amplitudes and the emission rate range measurable are all dependent on signal to noise ratio.

So there is a limitation in the study of fine structure with conventional DLTS. If for instance the fine structure is composed of two close time constants differing by a factor less than 10, a broad peak is given instead. A better resolution can be obtained via two ways; (i) by reducing the width of the excitation electrical pulse, provided a large imbalance of the capture cross sections holds between the two levels. This procedure allows filling the level with large capture cross section only; (ii) by using Laplace DLTS which is capable of resolving two levels with emission rate differing by a factor of 2, no matter how different are their respective capture cross sections, provided both levels are saturated. This approach makes possible the observation of effects and processes which are difficult if not impossible to observe with the usual methods.

The relaxation process of the non-equilibrium capacitance can be written as the sum of several exponential processes, given by

$$C(t) = \sum_{i=1}^{n} C_{oi} \exp(-e_{ni} t), \tag{2.35}$$

where e_{ni} represents the emission rate from the level E_i. The central issue to this analysis is how to convert the exponential decays – transients - from the time domain to the frequency domain. The appropriate mathematical procedure is the inverse Laplace transform [10]. This idea is developed in Laplace DLTS method.

The recorded transient is described as a continuous spectrum of emission rates rather than the discrete sum given by equation

$$f(t) = \int_0^{\infty} F(s) \exp(-st) ds, \tag{2.36}$$

where *f(t)* is the measured transient and *F(s)* is the spectral density function. The basic idea is to determine the solution *F(s)* from the measured transient *f(t)* by using an appropriate mathematical algorithm – the inverse Laplace transform of the averaged transient *f(t)*. The result of this procedure is a spectrum of clear and narrow delta-like peaks for a mono- or multi-exponential transient, allowing getting information on the number of levels and values of emission factors for each of the peaks. If the transient is described by the multi-exponential expression, the individual peaks are centered about the emission rates e_n with the intensities ΔC obtained as the areas under each sharp peak.

The main difficulty is that the analytical dependence *f(t)* has a unique solution *F(s)*, but in the case of the experimental results the existence of noise leads to a set of solutions. The task of the original signal *F(s)* reconstruction by the image *f(t)* can be considered as the problem of finding stable solutions of Fredholm integral **equation 2.36** of the first kind, related to the class ill-posed problems.

The mathematical algorithm used to obtain the solution *F(s)* is known as the Tikhonov regularization method [11]. Laplace DLTS utilizes three mathematical routines that are all based on the Tikhonov regularization method (CONTIN [12], FTIKREG [13] and FLOG [14]).

For comparison **Figure 2.9** shows the Laplace DLTS and DLTS spectra, obtained from the same *Si:Au,H* sample. Both spectra were taken at the same conditions: with -5V reverse bias and a 1 ms filling pulse [7].

The broad peak in conventional DLTS spectrum of hydrogenated silicon containing gold centered at 260 K is attributed to electron emission from both the gold acceptor and G4 which has been identified as the complex Au-H. The main spectrum uses the Laplace technique and clearly separates the gold-acceptor level and the gold-hydrogen level G4.

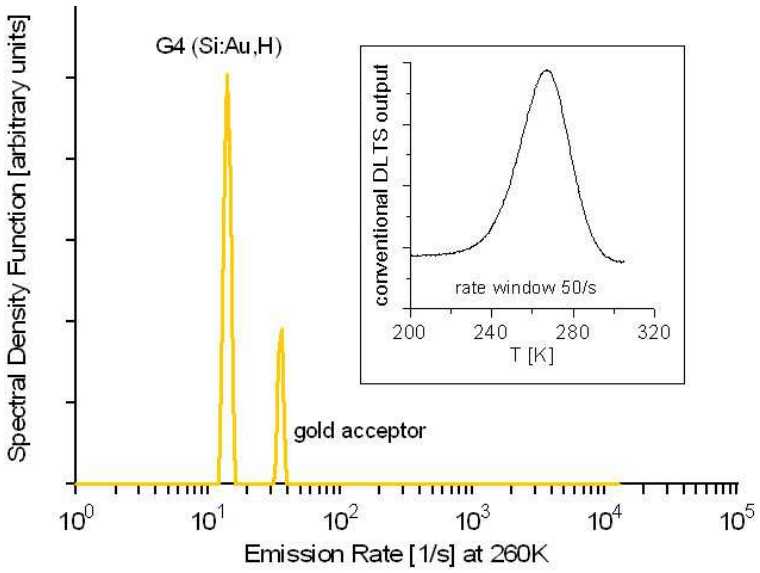

Fig. 2.9. DLTS (insert) and Laplace DLTS spectra of hydrogenated silicon containing gold [7].

Thereby Laplace DLTS technique has several advantages which are summarized below:

- It is an isothermal technique in which the capacitance transient is averaged at a fixed temperature;
- As a rule of thumb, the components are reliably separated for emission rate ratios larger than a factor of 2;
- The substantial increase in resolution allows investigating more closely spaced deep energy levels in the band gap of semiconductor.

2.2.5. Minority carrier transient spectroscopy (MCTS)

The two methods – DLTS and Laplace DLTS – depicted above, are used to investigate majority carrier emissions from deep levels in the upper half of the band gap in n-type semiconductor. To be able to detect minority carrier traps in a Schottky barrier, where there is no *p*-type part to supply holes, the key issue is to rely on an external optical source to generate minority carriers in the depletion region. This method is called minority carrier transient spectroscopy (MCTS) [15] and is dedicated to the investigation of the lower half of the band gap in n-type materials or the upper half in *p*-type materials.

The approach to study minority carrier thermal relaxation processes was first described in detail by Sah *et al.*[16] The methodology is very similar to majority carrier measurements with the exception that the occupancy is perturbed by the capture of minority carriers in the lower half of the semiconductor band gap in n-type material. For the Schottky diodes, majority carrier traps are observed by

applying an electrical pulse, while minority carrier traps can be observed when the reverse bias is kept constant and light pulses with the photon energy greater than the band-gap are used to generate exponentially electron-hole pairs from the surface down in the bulk [15]. The signal treatment remains uncharged.

In MCTS technique the diode is permanently under reverse bias while the laser is pulsed. The free electron-hole pairs generated in the device may lead to two components of the photocurrent, depending on the absorption coefficient. The first results from the pairs, generated within the depletion region. These pairs are separated by the field, creating a generation current. The second component is composed of a pure minority carrier flux generated in the bulk, but within a diffusion length of the barrier, and flowing through the space-charge region since the majority carriers generated in the bulk are repelled by the potential barrier. Depending on the wavelength used, one of the two components may be dominant. Therefore, the only significant component of the photocurrent is the generation current.

The Poole-Frenkel effect, effective for positively charged holes being trapped by negatively charged centers, can quantitatively be probed.

Summary

To summarize the methods used in this work they are all based on capacitance transient measurements. A temperature-dependent capacitance transient of a Schottky diode is produced, whenever deep energy levels within the depletion region emit charge carriers to any of allowed bands after a filling process. The filling of the deep levels with charge carriers can take place by pulsing the diode from reversed to forward bias in case of conventional DLTS or optically with a sub-band gap light pulse while the reverse bias is kept constant in conventional MCTS. The approach of treating the signal is either an analog signal processing in which the transient is multiplied by time-dependent weighting function whereas high resolution Laplace DLTS is based on digital signal processing using an appropriate mathematical algorithm. This procedure is called inverse Laplace transform. As a result deep level's *signatures* are extracted from the Arrhenius analysis.

Bibliography

1. Schottky, W.H., *Zur Halbleitertheorie der Sperrschichtrichter und Spitzen-gleichrichter.* Zeitschrift für Physik, 1939. **113**(516): p. 367.
2. Schottky, W.H., Zeitschrift für Physik, 1939. **113**(516): p. 367.
3. Sze, S.M., *The physics of semiconductor devices*. 1969, New York: John Wiley and Sons.
4. Blood, P. and J.W. Orton, *The Electrical Characterization of Semiconductors: Majority Carriers and Electron States*. 1992, London: Academic Press.
5. Lang, D.V., *Fast capacitance transient appartus: Application to ZnO and O centers in GaP p-n junctions.* Journal of Applied Physics, 1974. **45**(7): p. 3014-3022.
6. Istratov, A.A. and O.F. Vyvenko, *Exponential analysis in physical phenomena.* Review of Scientific Instruments, 1999. **70**(2): p. 1233-1257.
7. Dobaczewski, L., A.R. Peaker, and K.B. Nielsen, *Laplace-transform deep-level spectroscopy: The technique and its applications to the study of point defects in semiconductors.* Journal of Applied Physics, 2004. **96**(9): p. 4689-4728.
8. Frenkel, J., *On Pre-Breakdown Phenomena in Insulators and Electronic Semi-Conductors.* Physical Review, 1938. **54**(8): p. 647-648.
9. Makram-Ebeid, S. and M. Lannoo, *Quantum model for phonon-assisted tunnel ionization of deep levels in a semiconductor.* Physical Review B, 1982. **25**(10): p. 6406-6424.
10. Nolte, D.D. and E.E. Haller, *Optimization of the energy resolution of deep level transient spectroscopy.* Journal of Applied Physics, 1987. **62**(3): p. 900-906.
11. Provencher, S.W., *A constrained regularization method for inverting data represented by linear algebraic or integral equations.* Computer Physics Communications, 1982. **27**(3): p. 213-227.
12. Provencher, S.W., *CONTIN: A general purpose constrained regularization program for inverting noisy linear algebraic and integral equations.* Computer Physics Communications, 1982. **27**(3): p. 229-242.
13. Weese, J., *A reliable and fast method for the solution of Fredhol integral equations of the first kind based on Tikhonov regularization.* Computer Physics Communications, 1992. **69**(1): p. 99-111.
14. Matulis, A. and Z. Kancleris.

    http://www.laplacedlts.eu/help/default.htm?turl=511tikhonovregularisationmethod.htm.
15. Hamilton, B., A.R. Peaker, and D.R. Wight, *Deep-state-controlled minority-carrier lifetime in n-type gallium phosphide.* Journal of Applied Physics, 1979. **50**(10): p. 6373-6385.
16. Sah, C.T., et al., *Thermal and optical emission and capture rates and cross sections of electrons and holes at imperfection centers in semiconductors from photo and dark junction current and capacitance experiments.* Solid-State Electronics, 1970. **13**(6): p. 759-788.

EXPERIMENTAL DETAILS

CHAPTER III. EXPERIMENTAL DETAILS.

3.1. SAMPLE PREPARATION.

3.1.1. Ge samples description

In this study we used *n*- and *p*-type (001) oriented, 300 µm thick, 2-Ω cm Ge-single crystal wafers from UMICORE. The wafers are doped with antimony (Sb) or gallium (Ga) at concentrations of 1.4×10^{15} cm^{-3} and 1.8×10^{15} cm^{-3}, respectively. The residual concentration of oxygen is below 10^{15} cm^{-3} whereas the one for carbon is below 10^{14} cm^{-3}.

3.1.2. Metallic contamination by Ni, Fe and Cr

3.1.2.1. Implantation

The back sides of the wafers have been implanted respectively with Cr, Ni and Fe at 100 keV and doses of 5×10^{14} cm^{-2}. At this energy SRIM (Stopping and Range of Ion in Matter) simulation gives projected ranges for Fe, Ni and Cr of respectively 55 nm, 53 nm and 58 nm with straggling of 30 nm, 29 nm and 32 nm. The reason for implanting into the back side was to avoid any interference with irradiation defects which could otherwise be disturbing if the implantation were done into the front side where the analyses were carried out.

The implantation of stable ions has been performed at the laboratory in InESS (**In**stitut d'**É**lectronique du **S**olide et des **S**ystèmes) with the implanter EATON 200 kV, presented in **Figure 3.1**.

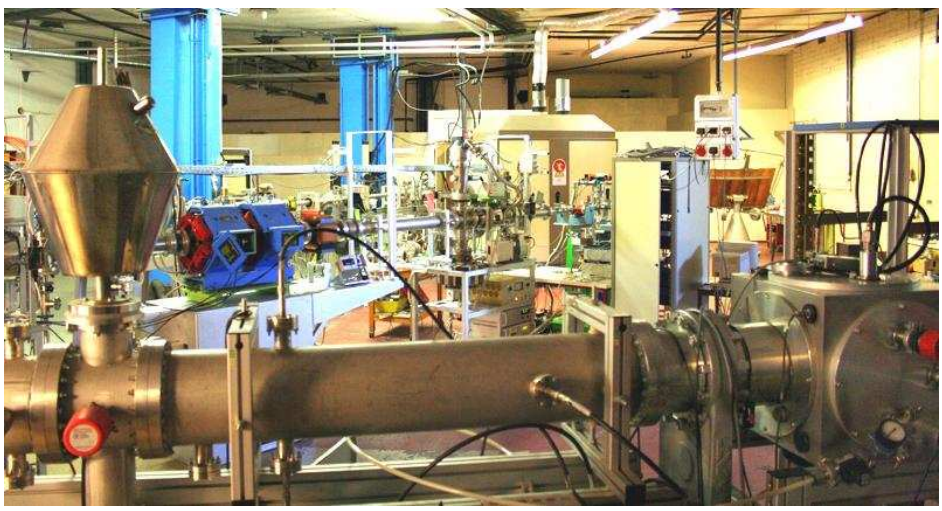

Fig. 3.1. Implanter EATON 200 kV used at InESS.

The ion implantation proceeds following successive steps, starting with the production of the ions of the desired element (Cr, Fe and Ni) at the ion source. Then the mass selection is carried out through a magnet whose allows selecting the desired element or isotope and finally accelerated towards to the target material. Thus acceleration of the specific ions to its normal energy of 100 keV is the last step. This is achieved by subjecting the charged particles to an electrostatic potential.

3.1.2.2. Annealing

A post-implantation annealing in a quartz tube under 300 mbar of Argon for about 15 min at 500 °C revealed to be sufficient to remove the implantation damage and redistribute the metal atoms in lattice sites throughout the whole sample.

From C-V (capacitance-voltage) investigation we measured net doping concentration in the range from 9×10^{13} cm^{-3} to 2×10^{14} cm^{-3}, depending on the sample.

A preliminary test which consisted of implanting Ge successively into the back and front side followed by annealing at 500 °C for 15 min did not reveal any residual defects as DLTS analysis resulted in a flat spectrum.

3.1.3. Schottky and junction preparation

3.1.3.1. Schottky for *n*-type Ge

Before evaporating the electrical contacts the samples were etched during a few seconds in a mixture of nitric and hydrofluoric acid - $HNO_3 : HF$ - in the proportions 3:1. Such a treatment appeared to be responsible for the hydrogen injection into the first few microns of the substrate, forming the observation area [1]. Hydrogen is expected to bind to TM impurities, producing new and sometimes unexpected deep levels in the Ge bandgap. This aspect will be discussed in **Chapter IV** devoted to the experimental results.

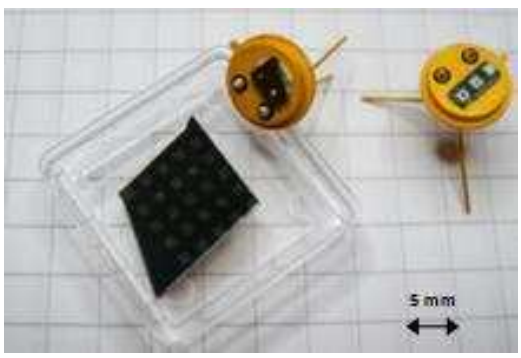

Fig. 3.2. Schottky for *n*-type Ge, independent and glued on the *TO5* packages.

As a last step, Au dots *1×1 mm²* were evaporated (150 Å) on the front side to form semi-transparent Schottky contacts and Al layer was evaporated (500 Å) on the back side to form ohmic contact. Gold (Au) has a large work function (5.1 eV) compared to the electron affinity of Ge (4.13 eV) meaning that Au on *n*-type Ge will act as a rectifying Schottky barrier. The diodes are mounted on TO5 sample holder as shown in **Figure 3.2**.

3.1.3.2. Junctions on *p*-type Ge

Schottky contacts on *n*-type samples were formed after standard chemical cleaning of the surface. This approach does not work on highly doped *p*-type samples. To circumvent such a difficulty n^+p-mesa diodes were prepared in the Institute of Physics and Astronomy, at the University of Aarhus, Denmark.

The n^+-top layer consists of an epitaxial Sb-doped Ge layer grown by molecular beam epitaxy (**MBE**) in which a sufficiently high concentration of Sb is incorporated during the growth. The drawback resulting from this procedure is that a significant fraction of antimony diffuses into the *p*-type substrate beyond the junction leading to a counter doped area. Thus, Sb related signals can be expected to appear in the DLTS spectra from the p-type region under certain conditions. In the same time both C and O contaminants may diffuse, however, much less than Sb. In any case a special attention must be addressed when analyzing the spectra. The resulting current-voltage (IV) characteristics of the so manufactured n^+p mesa diodes reveal to be good enough for our purposes [2]. Finally, as a consequence of the very shallow acceptor levels of Ga and Sb in Ge (about 11 meV above the valence band or below the conduction band, respectively), the carrier freeze-in temperature is much lower as compared to silicon. This allows the DLTS scans to start at ~ 20 K, which is a serious advantage when compared to silicon.

To form an ohmic contact Au layer was evaporated (500 Å) on the back side.

3.1.4. Metallic contamination by Au

Au-diffused samples were prepared in the following way. Firstly, the 1000 Å layer of Au was evaporated on the back side of n-type Ge wafer. Annealing in a quartz tube under 300 mbar of Argon for about 6 hours at 700 °C was followed before usual etching and contact evaporation is realized as it is described above.

Average net doping concentration for Au-doped samples, obtained by C-V measurements, is found to be equal to 0.9×10^{14} cm^{-3}.

3.1.5. Treatment devoted to check hydrogen injection

Cr-implanted n-type wafers were annealed during 5 hours at 500 °C to allow a distribution of the metal throughout the whole sample. One type of samples was treated by hydrogen during 2 min in HNO_3:HF solution prior to contact formation. Some of the samples were annealed a second time under Ar atmosphere (300 mbar) in a sealed ampoule during 30 min at 450 °C, a temperature required to release and out diffuse hydrogen from the observation area, and directly put into the evaporator for contacts formation. These samples are not supposed to contain any hydrogen.

3.2. EXPERIMENTAL SETUP

Before proceeding with the defect analysis, current-voltage (I-V) and capacitance-voltage (C-V) were carried out to help selecting the best diodes, a prerequisite for a pertinent defect analysis. As the examples, the I-V characteristic at RT for Au-, Cr-, Ni- and Fe-doped *n*-type Ge and C-V characteristic for the same types of doping and also the case of implantation Ge into Ge in *n*-type Ge are presented in **Figure 3.3** and **Figure 3.4**, respectively. **Figure 3.5** represents I-V and C-V characteristics and concentration profile of Ni-doped *p*-type Ge sample. The necessity of implanting the metallic impurities followed by annealing procedure seems to be harmful for n^+p diodes, which is clearly demonstrated in **Figure 3.5**.

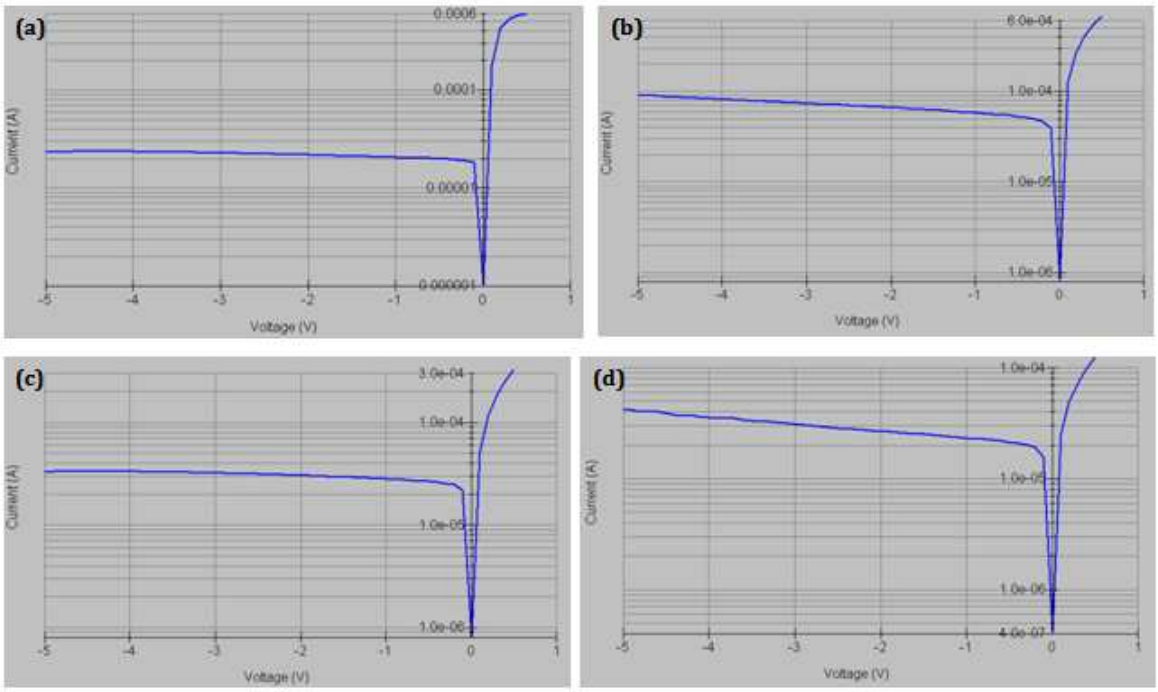

Fig.3.3. I-V characteristic of (a)Au-, (b) Cr-, (c) Ni- and (d) Fe-doped *n*-type Ge sample at RT.

Figure 3.4 displays the representative A^2/C^2-V data of device, based on Au-doped *n*-type Ge sample, at RT while the spatial distribution of background concentration of the device is shown in the inset of the same figure.

A linear behavior of the inversely squared capacitance A^2/C^2 versus applied bias V clearly supports Schottky behavior of the metal-semiconductor contacts. The depth profile of the apparent doping concentration in the explored area is uniform starting from the depth around 2 μm as follows from the inset of the **Figure 3.4**.

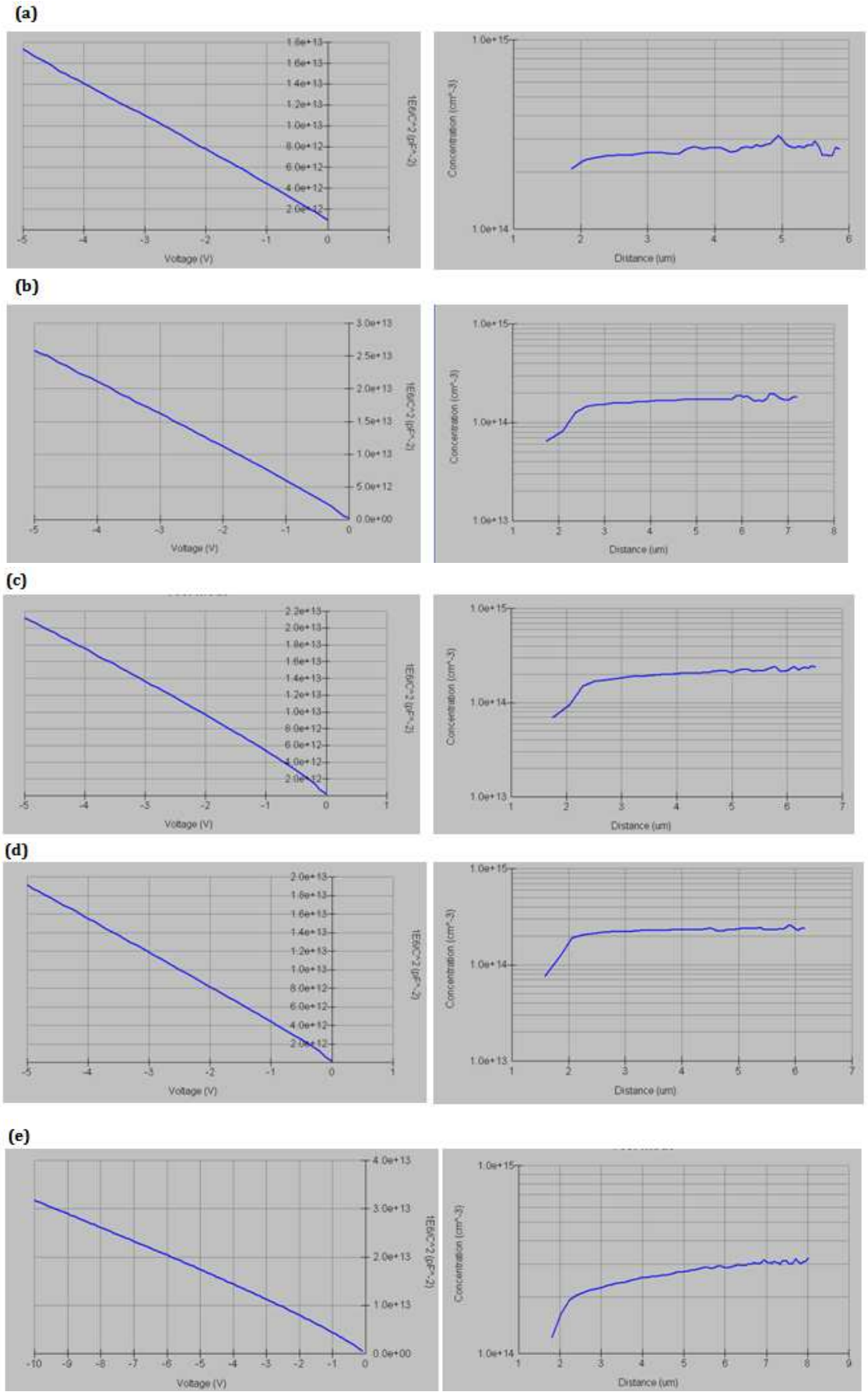

Fig.3.4. Typical C-V characteristic (left) and depth profile of the background concentration in the depletion region (right) of (a) Ge-, (b) Au-, (c) Fe- and (d) Cr, (e) Ni-doped *n*-type Ge sample at RT.

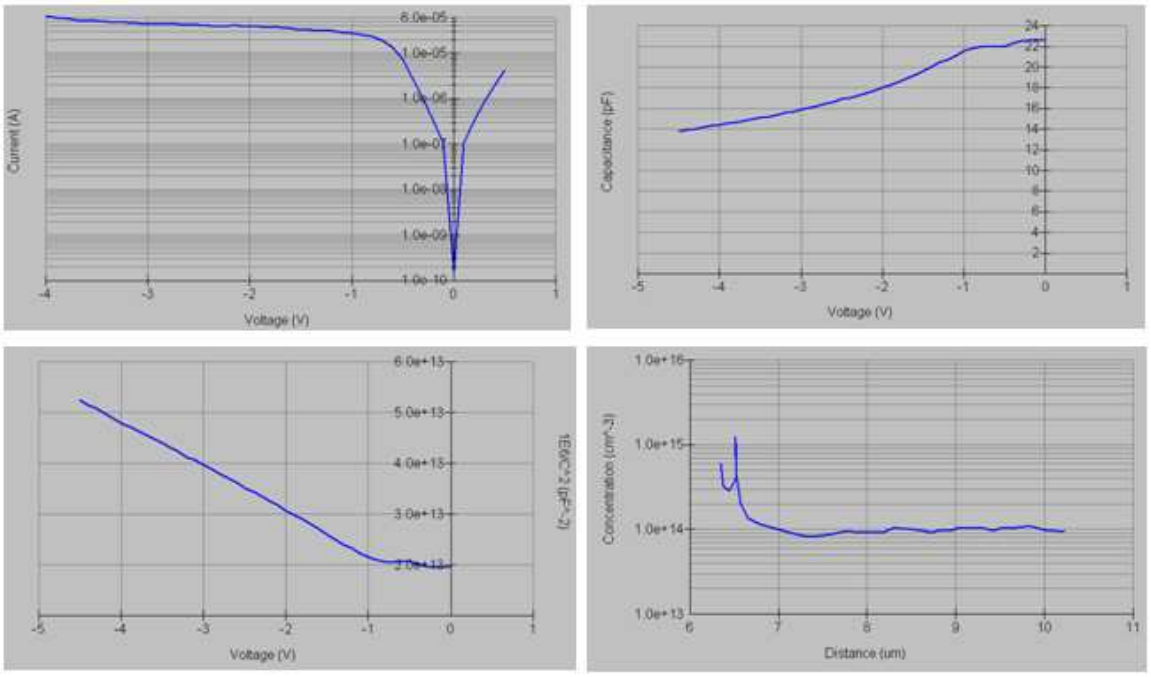

Fig.3.5. I-V, C-V characteristics and depth profile of the background concentration in the depletion region Ni-doped *p*-type Ge sample at RT.

For conventional DLTS and Laplace DLTS measurements a commercial setups was used. It contains an acquisition and pulse generator (*National instrument 6251*) for sample biasing and pulsing, a *GPIB* interface to control all system, a capacitance meter (*Boonton 7200*), a capacitance compensator, a temperature controller (*LakeShore 340*) and a closed cycle cryostat with helium compressor enabling to scan the temperature in the range from 10K to 800K. The whole system shown in **Figure 3.6** is fully controlled by an appropriate software [3].

For MCTS measurements a commercial *Polaron S4600* setup from *Bio-Rad* company was used. The system is shown in **Figure 3.7**. It is based on the double-box car method with a simultaneous recording of two rate windows. As light source the GaAs laser diode, emitting at 850 nm with a variable power up to 200 mW, is connected directly onto the cryostat.

As was mentioned above, depending on the wavelength used, one of the two components of the photocurrent may be dominant. In the present study, the depletion width is of the order of 3 μm whereas the penetration depth (1/e value) at the wavelength given above is of the order of 0.2 μm. Therefore, the only significant component of the photocurrent is the generation current. In the present case this has the advantage of excitation in a limited region near the interface where the electric field is maximum and can be varied significantly.

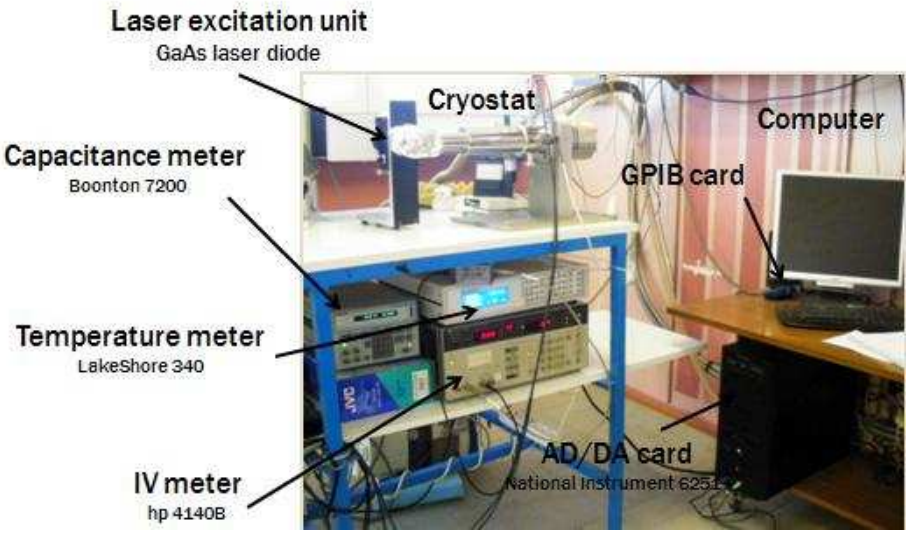

Fig. 3.6. Custom conventional DLTS and Laplace DLTS system.

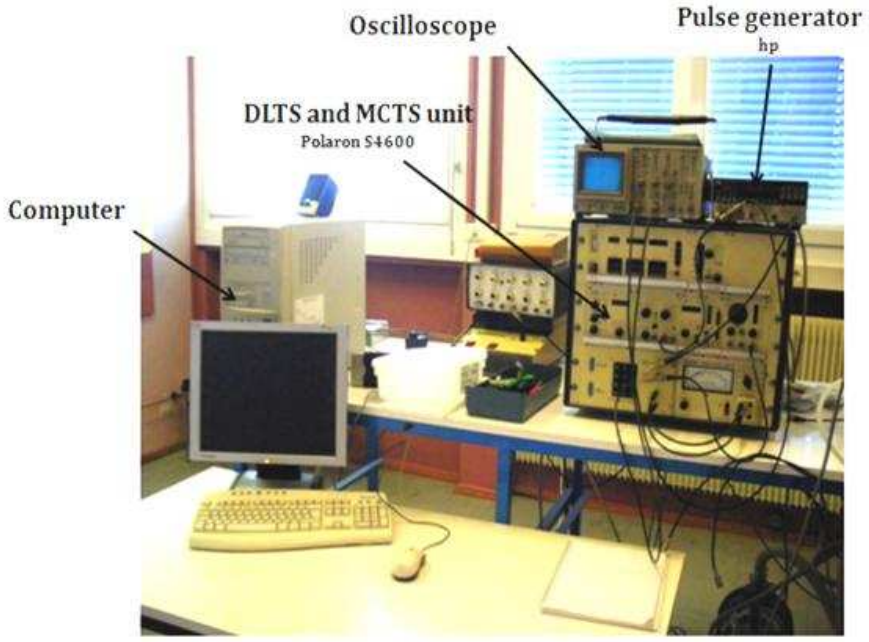

Fig. 3.7. Part of the commercial system for MCTS measurements.

Bibliography

1. Pankove, J.I. and N.M. Johnson, *Chapter 1 Introduction to Hydrogen in Semiconductors*, in *Semiconductors and Semimetals*, I.P. Jacques and M.J. Noble, Editors. 1991, Elsevier. p. 1-15.
2. Lindberg, C.E., et al., *The antimony-vacancy defect in p-type germanium.* Applied Physics Letters, 2005. **87**(17): p. 172103-3.
3. Dobaczewski, L., A.R. Peaker, and K.B. Nielsen, *Laplace-transform deep-level spectroscopy: The technique and its applications to the study of point defects in semiconductors.* Journal of Applied Physics, 2004. **96**(9): p. 4689-4728.

EXPERIMENTAL RESULTS AND DISCUSSION

CHAPTER IV. EXPERIMENTAL RESULTS AND DISCUSSION.

4.1. INTRODUCTION

In this chapter capacitance transient measurements, dealing with four types of impurities, namely Cr, Fe, Ni and Au, are presented. The impurity-related levels and the corresponding temperature dependencies of carrier emission and capture rates have been carefully investigated. The use of Schottky barriers for *n*-type Ge restricts the studies to levels located in the upper half of the band gap. However, by applying external optical excitation, to generate minority carriers, the investigation is extended to the lower half of the band gap. We were successful only in one type of n^+p mesa diode preparation –doped with Ni, which turned out to be very helpful in studying Ni-induced hole trap located in the lower half of the bandgap.

Before proceeding with defect analysis, current-voltage (*I-V*) and capacitance-voltage (*C-V*) were carried out to help selecting the best diodes, a prerequisite for pertinent defect analysis.

The structure of the chapter is the following. The first part investigates the upper part of the Ge bandgap, using DLTS and Laplace DLTS analysis. The temperature dependent trap parameters are obtained and the role of hydrogen as an unavoidable contaminant giving rise to the generation of complex-related levels in the band gap is highlighted. The second part deals with the investigation of the lower part of bandgap using MCTS technique on Schottky diodes, as well as DLTS and Laplace DLTS on n^+p junctions allows investigating hole traps in the case of Ni.

4.2. DLTS ANALYSIS

As was discussed in **Chapter I**, *Clauws et al.* [1] performed the most thorough research on metallic impurities in germanium, using mainly DLTS technique. Their spectra [1-7] revealed however a clear asymmetry for the three impurities Cr, Fe and Au, suggesting the presence of a nearby level manifested as a shoulder on the low temperature side of the major peak. Results, concerning Ni-doped *n*-type Ge [8], in addition to the major peak, show the presence of Cu in the bandgap, assuming contamination by Cu during diffusion process. The purpose of this work is to examine and possibly complete the earlier findings of *Clauws et al*.

Figures 4.1, 4.2 and **4.3** show typical DLTS scans of n-type germanium samples contaminated with Fe, Cr and Ni, respectively. The DLTS signals were recorded for a reference time constant of τ_{ref} =10 ms, corresponding to a rate window of 100 s^{-1}. The pulse sequences are (-4V; -1.5V) for of Cr-doped samples and (-4V; -2V) for Fe- and Ni-doped samples.

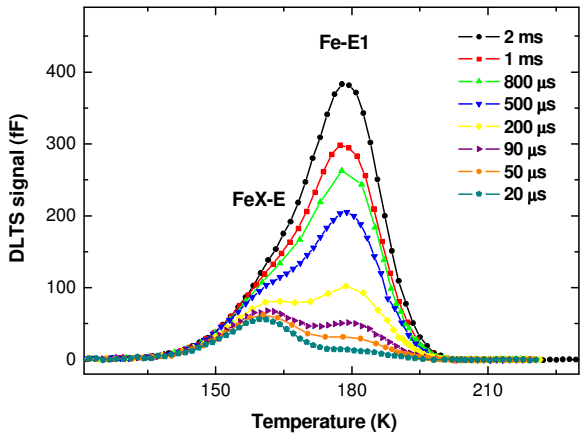

Fig. 4.1. DLTS spectra of Fe contaminated *n*-type Ge samples. The scans were recorded with the pulse sequence (-4V; -2V) and at a rate window of 100 s^{-1}. The pulse widths are indicated in the figure.

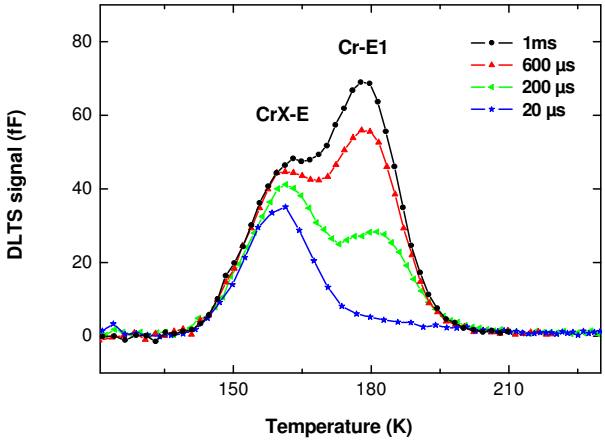

Fig. 4.2. DLTS spectra of Cr contaminated *n*-type Ge samples. The scans were recorded with the pulse sequence (-4V; -1.5V). The other parameters are similar to those indicated in **figure 4.1**.

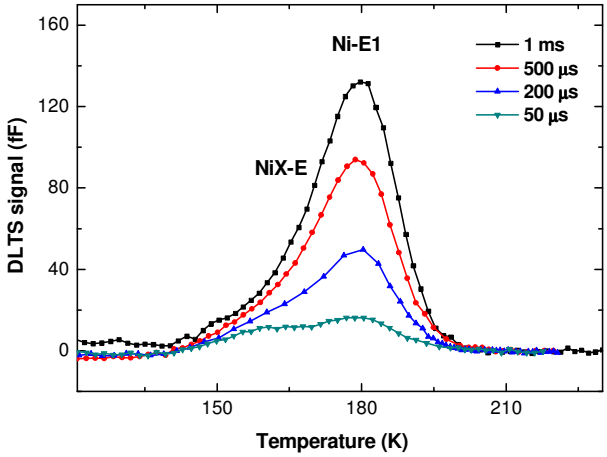

Fig. 4.3. DLTS spectrum recorded in the Ni-diffused *n*-type Ge sample. The scans were recorded with the same conditions as in **figure 4.1**.

In our experiments the amplitudes of filling pulses are selected to be less than zero volt but greater-than reverse bias. Such filling pulses reduce the effect of minority carrier (hole) tail at the germanium/metal interface, but retain the amplitude of the DLTS peak highest possible. It has been shown in a recent study [9] that the barrier height for the Au-Ge Schottky diodes is close to or exceeds the band gap value. Such a high barrier results in the appearance of an inversion layer with a high concentration of holes near the semiconductor surface. Application of "injection" (forward or zero) bias to such Au-Ge diodes results in a flux of holes from the inversion layer to semiconductor bulk, thus explaining the possibility of recharging of hole traps in the lower part of the band gap of *n*-type Ge samples with Au Schottky barriers [9].

The positive sign of the DLTS signals indicate emission of majority carriers.

For the largest pulse duration, corresponding to the conditions used by *Clauws et al.* [1-6], almost a single peak, labeled TM-E1 with TM indicating the transition metal, is observed at 180 K although a shoulder, labeled TMX-E, can already be guessed on the left-hand side at around 160 K for all spectra. Below this temperature and above the major peak no other level is detected. As a first step toward understanding the shoulder, varying the pulse width could be very instructive.

Figures 4.1, 4.2 and **4.3** show a significant drop of the amplitude of the major peak TM-E1, confirming the imbalance of the capture cross sections between the major peak and the shoulder. The use of lower pulse durations allows indeed the shoulder to emerge. We can infer qualitatively that the capture cross section of the major peak TM-E1 is significantly lower than for peak TMX-E, which will be confirmed quantitatively below. It is worth mentioning that for pulse duration of 20 µs the major peak TM-E1 vanishes completely in Cr doped germanium.

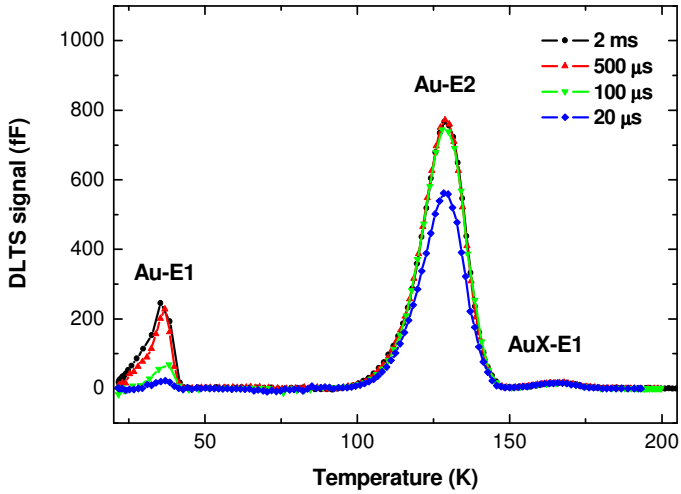

Fig. 4.4. DLTS spectrum recorded in the Au-diffused *n*-type Ge sample. The scans were recorded with the pulse sequence (-5V; -2V), the other conditions being the same as in **figure 4.1**.

Although Au is considered to be the most intensively studied metal in Ge, its analysis continues to display interesting facts.

Typical DLTS spectra of gold-diffused *n*-type Ge sample are shown in **Figure 4.4**. The signals were recorded with the pulse sequence (-5 V; -2 V), but with different filling pulses as indicated in the figure. Two main peaks, labeled Au-E1 and Au-E2, are observed at 35 K and 130 K, respectively. Also minor but significant "bump", labeled AuX-E1, is observed above 150K. Reducing the pulse width t_F (2 ms to 20 μs) seems to affect peak Au-E1 more strongly, allowing straightforward determination of the electron capture cross sections σ_{na} with the approach, detailed in **Appendix 1**.

Based on the doping concentration, the approximate relation (2.19) given on the page 33 in **Chapter II** allows estimation of the trap concentration in the considered samples. A trap concentration of 3×10^{12} cm^{-3} has been derived for Fe-doped Ge samples, 2.2×10^{12} cm^{-3} – for Ni-doped Ge samples, 1.4×10^{12} cm^{-3} – for Cr-doped Ge samples and around 1.4×10^{12} cm^{-3} for Fe-doped Ge samples

4.3. LAPLACE DLTS ANALYSIS

As it was described previously in **Chapter II**, achieving a better resolution of complex DLTS spectra can be reached via two ways:

- By reducing the width of the excitation electrical pulse provided the capture cross sections of the two close levels differ significantly, allowing thus to fill preferentially the level with large capture cross section only. The impact of this approach is shown in the figures above;

- By using Laplace DLTS method, which is capable of resolving two levels with emission rates differing by a factor of 2, no matter how different are their respective capture cross sections.

Figures 4.5, 4.6 and **4.7** display Laplace DLTS scans, recorded in Fe-, Cr- and Ni-diffused *n*-type Ge samples, respectively. The spectra were taken at temperatures close to the temperatures of maxima of the dominant peaks in the conventional DLTS results shown in **Figures 4.1-4.3**. The Laplace DLTS spectra look similar and consist of two sharp peaks – the shoulder and the major peak, clearly separated.

The shoulder appears now on the right hand side as the x-axis in a Laplace DLTS scan represents the emission rate which increases with the temperature, whereas in a conventional DLTS, the x-axis represents the temperature; this is why the positions of the peaks are inverted in both types of scans.

All three **figures 4.5-4.7** leave no doubt that the procedure of introducing transition metals utilized in this work, which is identical in all respects to the one used by *Clauws et al.* [1], is responsible for the creation of the observed shoulder. In the **Chapter 1.2.3** of present work the peak of **Figure 1.11 (a)**, displaying the DLTS spectrum of Fe-implanted *n*-type Ge, shows an asymmetry, although it is less obvious than in the case of Cr, shown in **Figure 1.10 (a)**. Thus the question is: whether the major peak and its shoulder are linked or is the shoulder an unwanted contamination with unknown origin, and if so what could be the nature of this contamination? These questions will be answered in the **Chapter 4.5**.

The insets of **Figures 4.5-4.7** display the Arrhenius diagram of the emission rates, corrected by the factor T^2, of the major levels TM-E1 and their corresponding shoulders TMX-E.

From the standard Arrhenius plots of the peaks position as a function of temperature, obtained by varying the emission rate windows, we get the activation enthalpy and the extrapolated capture cross section $\sigma_{na.}$

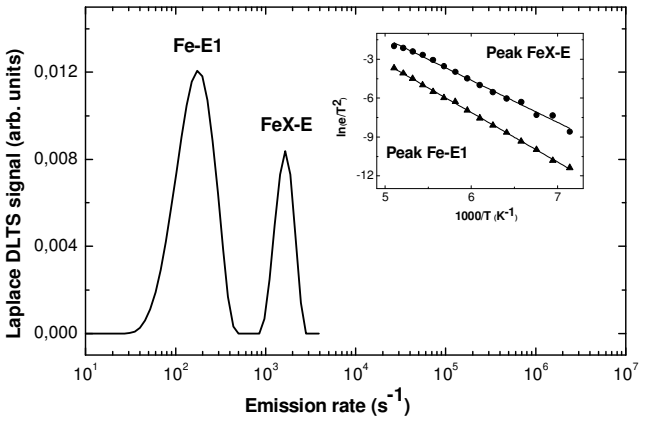

Fig. 4.5. Laplace DLTS spectrum recorded at T = 180K with the pulse width t_F = 200 μs, the other parameters being similar to the corresponding DLTS analysis.

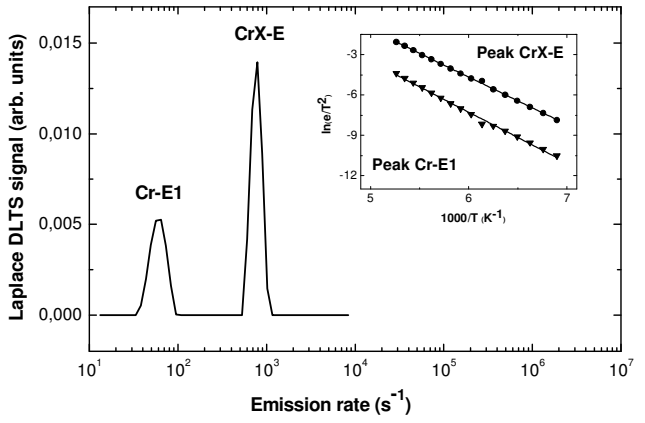

Fig. 4.6. Laplace DLTS spectrum recorded at T = 175K with the pulse width t_F = 200 μs, the other parameters being similar to the corresponding DLTS analysis.

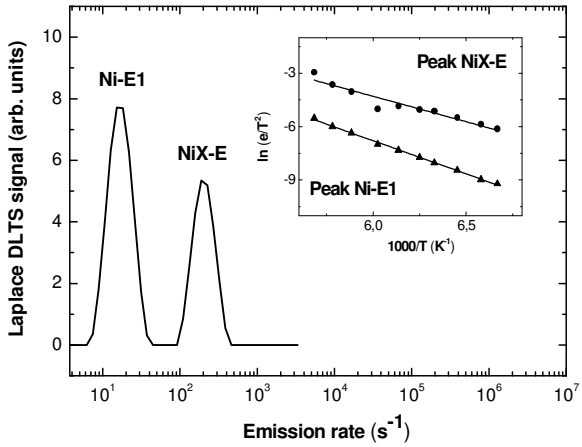

Fig. 4.7. Laplace DLTS spectrum recorded at T = 175K with the pulse width t_F = 200 μs, the other parameters being similar to the corresponding DLTS analysis.

The data for all the impurities consider in this work are listed in **Table 4.1**. Such low values of capture cross sections collected in **Table 4.1** are typical for centers repulsive for electrons.

Level label	K_T ($s^{-1}K^{-2}$)	E_{na} (eV)	σ_{na} (cm^2)
CrX-E	1.5×10^{7}	0.305±0.002	$(4.7\pm0.7)\times10^{-16}$
Cr-E1	4.2×10^{6}	0.325±0.005	$(1.4\pm0.5)\times10^{-16}$
FeX-E	4.1×10^{6}	0.287±0.006	$(1.3\pm0.6)\times10^{-16}$
Fe-E1	7.1×10^{6}	0.327±0.002	$(2.3\pm0.4)\times10^{-16}$
NiX-E	1.4×10^{5}	0.233±0.009	$(1.2\pm2.2)\times10^{-17}$
Ni-E1	5.5×10^{6}	0.321±0.005	$(1.8\pm0.6)\times10^{-16}$

Table 4.1: The activation enthalpy E_{na}, pre-exponential factor K_T and extrapolated capture cross sections σ_{na} derived from Arrhenius diagram in Laplace DLTS spectrum of Fe-, Cr- and Ni-diffused Ge.

As can be seen from **Figure 4.4**, the peak Au-E1 in DLTS spectra is broad and asymmetric: FWHM is equal to 10.5 K and T_m = 35 K. Therefore, if this were the signature of a single, well isolated level in the bandgap, its FWHM would have been equal to $\Delta T = 0.1 \times T_m$, which is not the case. Thus it is legitimate to expect the presence of close by level, which Laplace DLTS is expected to resolve. **Figure 4.8** shows the Laplace DLTS spectrum recorded on Au-diffused *n*-type Ge and taken at 35 K, and surprisingly, the scan displays one narrow peak with no subsidiary peaks over a range of almost two orders of magnitude above and one order below observed level. The inset shows the Arrhenius plot of the emission rate, corrected by the factor T^2, leading to the data given in **Table 4.2**.

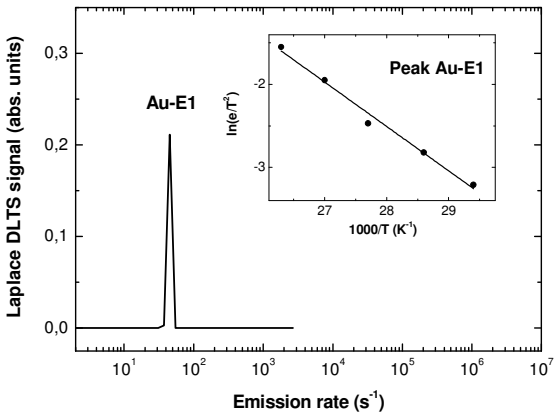

Fig. 4.8. Laplace DLTS spectrum recorded at T = 35K with the pulse width t_F = 200 μs, the other parameters being similar to the corresponding DLTS analysis.

In fact, the apparent asymmetry of the peak seen in conventional DLTS spectrum (**Figure 4.4**) can be simply explained if one realized the fact, that the peak shows up at a temperature very close to the freezing regime, as a consequence the capacitance drops as the free carriers are bound by the host atoms, thus not participating to the filling – emptying process. It turns out therefore that the asymmetry is an artifact. In other words there is no other structure and Au-E1 is a single level as indicated in Laplace DLTS.

In the Laplace DLTS spectrum for the Au-E2 defect a family of two peaks is observed as shown in **Figure 4.9**. This confirms the expectation that the spectrum displayed in **Figure 4.4** should contain few numbers of peaks due to the asymmetry of the peak Au-E2: FWHM is equal to 16.8 and T_m = 129 K. As can be seen, the FWHM is not equal to $\Delta T = 0.1 \times T_m$, indicating the presence of two close levels.

From the Laplace DLTS spectra taken at different temperatures the activation enthalpies and the apparent capture cross sections of peaks, labeled Au-E2 and AuX-E2, were obtained. The inset of **Figure 4.9** shows the Arrhenius plot of the emission rate, corrected by the factor T^2, leading to the data given in **Table 4.2**. Although Au is taken into consideration as the most extensively experimentally investigated impurity in Ge [6], there is still very little information on it and the presence and the results from the study of the family of two levels for Au-E2 (Au-E2 and AuX-E2) defect are firstly reported in the present work.

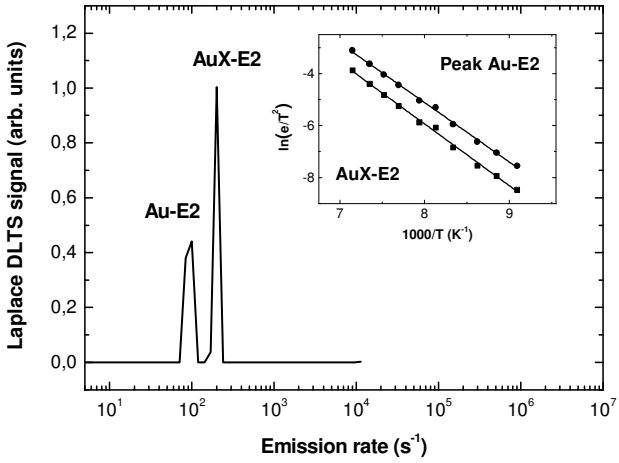

Fig. 4.9. Laplace DLTS spectrum recorded at T = 130 K with the pulse width t_F = 200 μs, the other parameters being similar to the corresponding DLTS analysis.

Taking into account the previous results, concerning shoulders in DLTS and Laplace DLTS spectra of Fe-, Cr- and Ni-doped *n*-type Ge, we suggest the presence of the shoulder appearance also in Au-doped samples. The question of the nature of the contamination giving such shoulders will be discussed in the **Chapter 4.5**.

Figure 4.10 shows Laplace DLTS spectrum with the inset of the Arrhenius plot of the emission rate, corrected by the factor T^2, for peak labeled AuX-E1 in **Figure 4.4**. The corresponding parameters are displayed in **Table 4.2**.

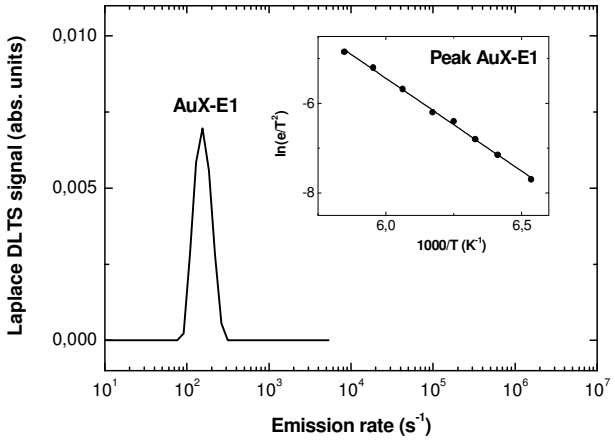

Fig. 4.10. Laplace DLTS spectrum recorded at T = 168 K with the pulse width t_F = 200 μs, the other parameters being similar to the corresponding DLTS analysis.

The emission behavior analyzed by the Laplace technique and presented in **Table 4.2** agrees with earlier published data [7, 10] for peak Au-E1, assigned to $Au_s^{(3-/2-)}$ and peak Au-E2, assigned to the charge sequence $Au_s^{(-/2-)}$. The electronic nature of the levels should be reflected in the capture cross sections. As may be seen from **Table 4.2**, Au-E1 and Au-E2 have the values of σ_{na} of about 1.1×10^{-17} cm^2 and 4.2×10^{-15} cm^2 respectively. Such low value of capture cross section in case of Au-E1 band is typical for center, repulsive for electrons, which is in agreement with the charge states assumed for the acceptor level. See **Table 1.8** in **Chapter I** for comparison.

Level label	K_T ($s^{-1}K^{-2}$)	E_{na} (eV)	σ_{na} (cm^2)
Au-E1	3.3×10^5	0.047±0.002	$(1.1\pm0.9)\times10^{-17}$
AuX-E1	3.1×10^8	0.359±0.006	$(1.0\pm0.5)\times10^{-14}$
Au-E2	1.3×10^6	0.212±0.001	$(4.2\pm1.6)\times10^{-15}$
AuX-E2	6.5×10^5	0.169±0.004	$(2.1\pm0.6)\times10^{-17}$

Table 4.2: The activation enthalpy E_{na}, pre-exponential factor K_T and extrapolated capture cross sections σ_{na} derived from Arrhenius diagram in Laplace DLTS spectrum of Au-diffused *n*-type Ge.

Besides the two main bands, a band at 165K (AuX-E1) was permanently observed. By the value of the activation enthalpy extracted from the Arrhenius plot of the emission rate and the temperature of level observation, the presence of well known copper-related band $Cu_s^{(3-/2-)}$ [11] can be suggested. But such a low value of σ_{na} (about 10^{-14} cm^2) might characterize rather donor level than repulsive center such as

$Cu_s^{(3-/2-)}$ is. Hence we suggest the presence of Sb-V pair (the E-center) which have been earlier found in the temperature range of (162-212) K in *n*-type Ge samples and investigated [12, 13], providing the activation enthalpy of 0.377 eV. Also we cannot exclude $Au_s^- Sb_i^+$ pair as possible candidate. The mobile Au_s^- ion is captured in the Coulomb field of Sb_i^+, forming a deep acceptor complex $(Au_s^- Sb_i^+)^{0/-}$. So far, no evidence for the existence of such pair in Ge has been found, but the possibility of forming such complex cannot be ruled out.

4.4. CAPTURE CROSS SECTION MEASUREMENTS

The strong drop of the DLTS signals, corresponding to peak TM-E1, where TM is transition metal in all three cases of Fe, Cr and Ni diffused samples, displayed in **Figures 4.1-4.3**, and to peaks Au-E1 and Au-E2 in **Figure 4.4**, is in favor of the existence of a potential barrier for capture with a consequence of a temperature dependent capture process. Such a behavior is reflected in a multi-phonon assisted capture kinetics [14], described by the following relationship

$$\sigma_n(T) = \sigma_\infty \left(-\frac{\Delta E_\sigma}{kT}\right). \tag{4.1}$$

Quantitatively the capture cross section is directly measured by the variable pulse length method, i.e. from the dependence of the Laplace DLTS amplitude upon the filling pulse at different temperatures [3]. The procedure is described in **Appendix 1**. The results are displayed in **Figure 4.11** for Fe, Cr or Ni in *n*-type Ge samples whereas **Figure 4.12** shows the results for Au.

The extracted values of barrier for capture for all species are listed in **Table 4.3**. These values allow correcting the magnitudes of the apparent activation enthalpy of ionization. The real values and the extracted entropy terms $\Delta S_n/k_B$ are also listed in **Table 4.3**.

Level	ΔE_n(eV)	σ_{na} (cm²)	σ_∞ (cm²)	E_σ(eV)	$\Delta S_n/k$	ΔH_n(eV)
Fe-E1	0.327±0.002	(2.3±0.4)×10^{-16}	(4.98±0.39)×10^{-15}	0.043	3.08	0.284
Cr-E1	0.325±0.005	(1.4±0.5)×10^{-16}	(4.59±0.36)×10^{-15}	0.046	3.49	0.279
Ni-E1	0.321±0.005	(1.8±0.6)×10^{-16}	(4.09±0.32)×10^{-15}	0.035	3.12	0.286
Au-E1	0.047±0.002	(1.1±0.9)×10^{-17}	(3.37±0.54)×10^{-14}	0.019	8.03	0.028
Au-E2	0.212±0.001	(4.2±1.6)×10^{-15}	(2.99±0.34)×10^{-13}	0.033	4.27	0.179

Table 4.3: The capture parameters derived by the variable pulse length method, apparent activation enthalpy of ionization and entropy of electron traps in Fe-, Cr-, Ni- and Au-diffused *n*-type Ge samples.

Note that E_σ is positive for all levels, meaning that the electron capture cross section for these repulsive centers increases with temperature.

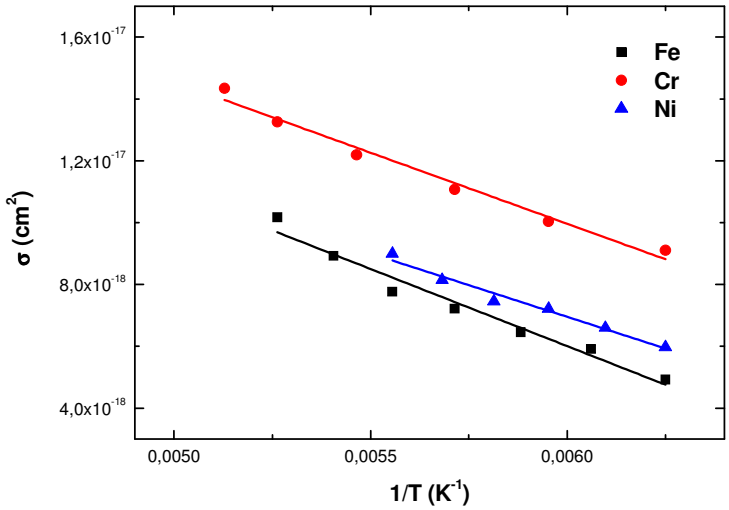

Fig. 4.11. The temperature-dependent capture cross sections of Cr-, Fe- and Ni-contaminated *n*-type Ge.

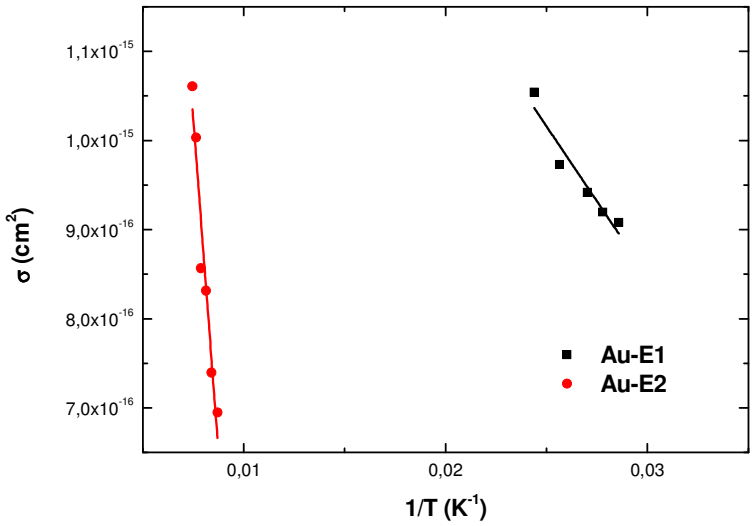

Fig. 4.12. The temperature-dependent capture cross sections of Au-contaminated *n*-type Ge.

The barrier for capture represents a clear indication that the observed electron traps listed in **Table 4.3** have an acceptor character. The drop in the amplitudes of the major peaks, observed when the pulse width is reduced, is indeed in favor of a repulsive character, which is consistent with our expectation and with results published by *Clauws et al.* [15]. It is also consistent with much earlier conclusions reported by *Woodbury* and *Tyler* [16] in the mid fifties showing that in Ge metallic species stabilize in substitutional sites, inducing acceptor levels as they are not tetravalent. According to this model, Au ($6s^1$), Cr ($4s^1$), Ni ($4s^2$) and Fe ($4s^2$), the four metals dealt with in the present work, are expected to introduce triple, for the first two, and double acceptor states, for the last two species. If these charge states distribute normally, the DLTS and Laplace DLTS signals correspond to the

configuration $Cr^{3-/2-}$, $Fe^{2-/-}$, $Ni^{2-/-}$ and $Au^{3-/2-}$ in case of level labeled Au-E1 and $Au^{2-/-}$ for one labeled Au-E2.

As to the shoulders and bumps, their identity will be discussed later. The related capture cross sections are quite large and cannot thus be measured by the procedure, applied to the major peaks. Large capture cross sections are generally assigned to defects exhibiting a donor character when interacting with the conduction band E_c.

4.5. HYDROGEN PRESENCE

It is worth mentioning that in all samples considered in the present work, none of observed levels presents without implanting transition metals but otherwise thermally treated in the same conditions (500 °C for 15 min) followed by conventional chemical treatment during 2 min in the solution consisting of a mixture of nitric and hydrofluoric acid, in the proportion *3:1*. The spectrum is flat as shown in **Figure 4.13**, indicating that no contamination could be expected although hydrogen diffusion cannot be avoided. Therefore, no other unexpected defect is present in the material to which H can bind.

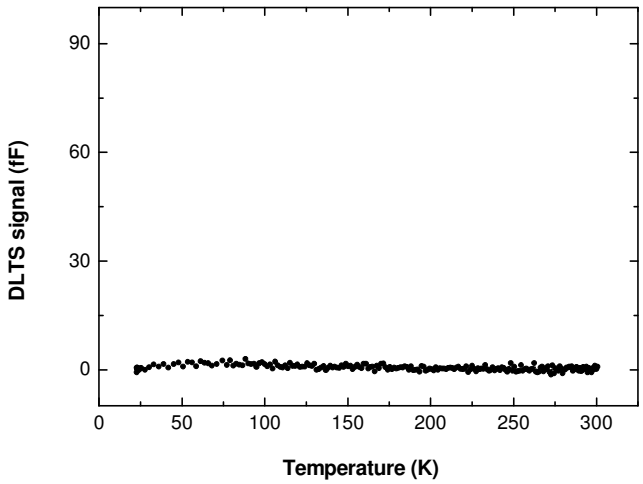

Fig. 4.13. DLTS spectra of pure not contaminated *n*-type Ge samples but thermally and chemically treated in the conditions which prevail for TM-implanted samples. The scans were recorded with the pulse sequence (-5V; -2V) and at a rate window of 100 s^{-1} with the pulse durations of 200 µs.

On the other hand, the damage caused by Si implantation, performed in the same conditions as for the transition metals, is completely removed by an annealing at 500 °C for 15 min, leading to a flat DLTS spectrum [17] similar to **Figure 4.13**. Moreover, the implantation of impurities in our case was performed on the back side, whereas the analyses were carried out on the front side of the wafer – more than 300 µm away from the implanted region. Therefore it can be assumed with confidence that the observed levels are related to the chemical species which have reached the front region by thermal diffusion.

The key issue regarding the shoulders TMX-E in case of Fe-, Cr-, Ni-diffused *n*-type Ge samples, is related to the way the samples were prepared before their characterization. The chemical treatment cannot be avoided as it is a prerequisite for a good quality of the diode. The difference between the results from various authors could be related to the nature and composition of the chemical solutions and the exposure time of the samples to those solutions which all contain ionic

hydrogen. This species is well known to diffuse into the substrate with the possibility of binding to existing defects [18].

Before evaporating the electrical contacts our samples were etched during a few seconds in a mixture of nitric and hydrofluoric acid, in the proportion *3:1*. Such a treatment is certainly responsible for hydrogen injection into the first few microns forming the observation area. Hydrogen is expected to bind to Cr as it does for the majority of metallic species so far studied in silicon [19, 20], although the microscopic details may differ from one type of material to another and from one existing defect to another. Thus, the amount of hydrogen inadvertently introduced will affect more or less the shape of a DLTS peak introducing differences in results from author to author, dealing with apparently similar experiments.

In germanium hydrogen has also been demonstrated to play a leading role [21, 22] in forming of new defect centers. The interaction of hydrogen with defects in semiconductors continues to be a field of active research due to its fundamental and technological relevance. In the present work our aim is to demonstrate, that hydrogen is an important partner in the observed shoulders.

Figure 4.14 displays two DLTS spectra recorded in Cr-contaminated *n*-type Ge samples before and after a significant annealing, following a dip during 2 min in the mentioned above chemical solution $-HNO_3:HF$ in the proportion *3:1*. We believe that the subsequent annealing for 30 min at 450 °C, necessary to remove hydrogen, leads to a redistribution of the metal resulting in a decrease of the DLTS peak height, impeding thus a one to one conversion. The shoulder appearing in **Figure 4.2** is now clearly enhanced and becomes the major peak. This CrX-E1 line disappears after an annealing at 450 °C during 30 min, a temperature known to release and diffuse out the hydrogen from the observation area.

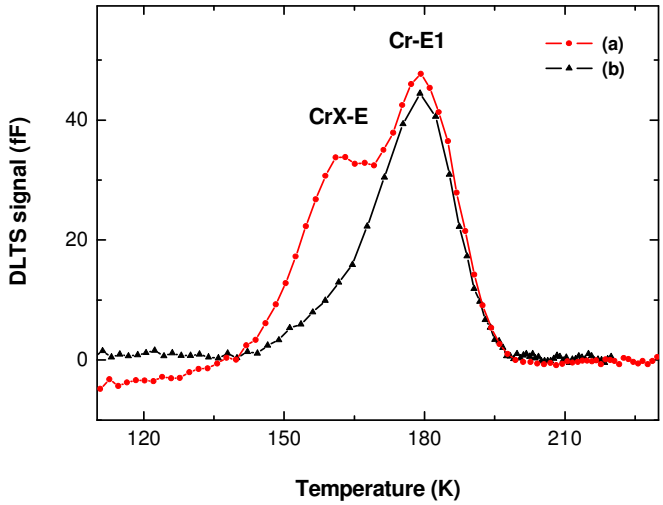

Fig. 4.14. DLTS spectra of Cr contaminated *n*-type Ge samples annealed 5 hours at 500 °C, treated 2 min by HNO_3 and (a) not annealed or (b) annealed 30 min at 450°C. The scans were recorded with the pulse sequence (-10V; -5V) and at a rate window of 100 s^{-1} with pulse duration t_F = 200 µs.

Figure 4.15 displays Laplace DLTS scans, recorded in *n*-type Ge samples, containing Cr, before and after a significant annealing, following a dip during 2 min in nitric acid. Application of the high resolution Laplace DLTS technique show two quite distinct levels Cr-E1 and CrX-E before and major peak Cr-E1 and almost vanished CrX-E after subsequent annealing. Laplace DLTS produces a plot of spectral density as a function of emission rate rather than capacitance change versus temperature as in conventional DLTS. **Figure 4.15** shows the effect of the annealing for 30 min at 450 °C on the Laplace DLTS spectra at 163 K. It can be seen that the lower emission rate peak Cr-E1 stays put due to the consideration of the area under each peak, corresponding to the integrated signal intensity in this technique, while the higher emission rate peak CrX-E diminishes significantly. We believe that the further annealing for 30 min at 450 °C, necessary to remove hydrogen, leads to a redistribution of the metal resulting in a decrease of the DLTS peak height, impeding thus a one to one conversion.

Repeating the Laplace DLTS at temperatures in the range 160-190 K enables us to construct the Arrhenius diagram of the emission rates, corrected by the factor T^2, shown in the inset in **Figure 4.15**. From the upper line corresponding to the shoulder CrX-E1 in not annealed *n*-type Ge sample, we obtain an activation energy of 0.350 eV, and for the lower lines, corresponding to the major level Cr-E1 and practically coincident for both cases of sample preparation as (a) not annealed and (b) annealed during 30 min at 450 ˚C – about 0.340 eV.

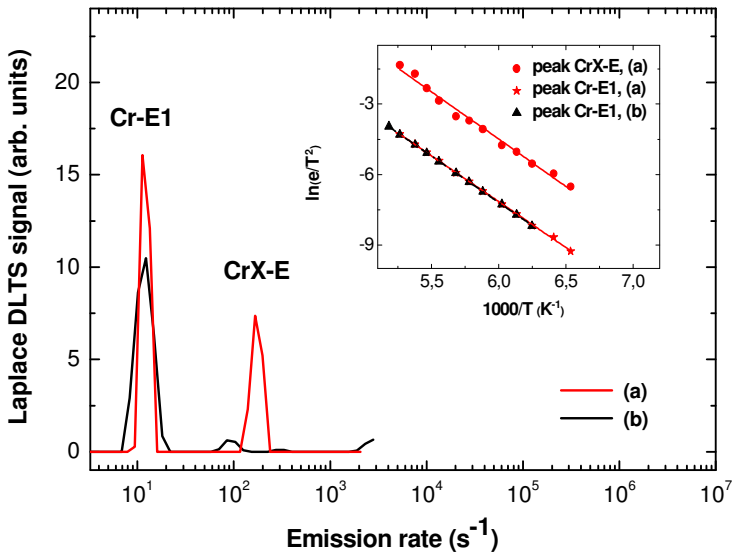

Fig. 4.15. Laplace DLTS spectrum of Cr contaminated *n*-type Ge samples annealed 5 hours at 500 ˚C, treated 2 min by HNO_3 and (a) not annealed or (b) annealed 30 min at 450°C. The scans were recorded at T = 163 K with the pulse width t_F = 200 μs, the other parameters being similar to the corresponding DLTS analysis resented in **Figure 4.14**.

The corresponding values of signatures and apparent capture cross sections are summarized in **Table 4.4**.

Level label	K_T ($s^{-1}K^{-2}$)	E_{na} (eV)	σ_{na} (cm^2)
Cr-E1 (annealed)	1.1×10^{7}	0.336±0.002	$(3.6\pm0.2)\times10^{-14}$
CrX-E1 (not annealed)	4.1×10^{8}	0.350±0.010	$(1.3\pm1.0)\times10^{-14}$
Cr-E1 (not annealed)	1.1×10^{7}	0.337±0.007	$(3.6\pm0.5)\times10^{-14}$

Table 4.4: The activation enthalpy E_{na}, pre-exponential factor K_T and extrapolated capture cross sections σ_{na} derived from Arrhenius diagram in Laplace DLTS spectrum of Cr-diffused *n*-type Ge.

From procedure and subsequent results described previously, it is concluded that the lower emission rate peak Cr-E1 staying almost put in Laplace DLTS spectra before and after annealing is due to the chromium acceptor while the higher emission rate peak CrX-E is due to the chromium-hydrogen complex.

The simplest defect, involving hydrogen, would be the pairs Cr-H. However, higher orders such as MH_n, where M stands for the metal and n for the number of hydrogen atoms involved in the complex cannot be excluded. Examples of such complex molecules are numerous in silicon [23].

For Fe, Ni and Au we observe the same trend. In these cases also the conversion between the hydrogen related shoulder and the major peak are not respected.

4.6. MCTS ANALYSIS

Previously used measurements such as DLTS and Laplace DLTS methods applied to the Schottky barriers on *n*-type Ge examine states in the half of the bandgap adjacent to the majority-carrier band. In order to access to the other half of the bandgap, minority carriers (holes in the present case) should be generated, making thus possible the characterization of minority carrier traps, requiring Schottky barriers on *p*-type Ge to be observed by the same methods or MCTS in *n*-type Ge [24].

It was unfortunately not possible to have fairly good *p*-type Schottky barriers compatible with DLTS analysis for Fe-, Cr- and Au-diffused Ge samples. To circumvent this difficulty we have used the semitransparent Schottky barriers on moderately doped *n*-type Ge and minority carrier transient spectroscopy (MCTS) allowing access to the lower half of the band gap. As was mentioned previously in **Chapter II** this procedure requires to keep the reverse bias constant while the above-band gap light is pulsed to generate minority carriers, in the present case – holes – in the depletion region [24]. However, because the light source is very seldom sufficiently intense we need to excite with a very large optical pulse width which has the drawback of making the use of large rate windows difficult if not impossible. Consequently, shallow levels appearing at low temperature would be barely visible. Also in our experiments the diode is illuminated through the front (Schottky) contact.

Figure 4.16 displays a typical MCTS spectrum for Cr-diffused n-type Ge sample. Very shallow hole trap Cr-H3 is expected around 20 K, but for the reason mentioned above it could not be fully recorded. Thus if there is no doubt that a level shows up very near the valence band E_v, we cannot figure out its signature. It's worth mentioning, that this shallow trap Cr-H3 seems to be field dependent due to its shift towards lower temperatures when the reverse bias is increased.

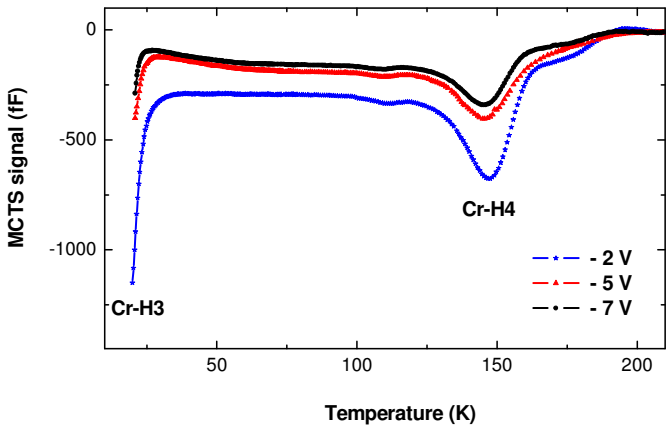

Fig. 4.16. MCTS scan of Cr-doped *n*-type Ge sample with optical pulse duration of 1 *ms* and rate window of 400 s^{-1} with the indicated biases.

Figure 4.17 focuses on the visible peak labeled Cr-H4 appearing around 150 K. The negative sign of MCTS signal indicates that the emission of the minority carriers is depicted here. Therefore, peak Cr-H4 is a hole trap located at 0.294 eV above the valance band E_v as obtained from the Arrhenius signature displayed in the inset. The apparent activation energy E_p, according to the analog of **Equation 4.1** for holes, as well as the apparent capture cross section $\sigma_p \exp(\Delta S/k_B)$, are given in **Table 4.5**.

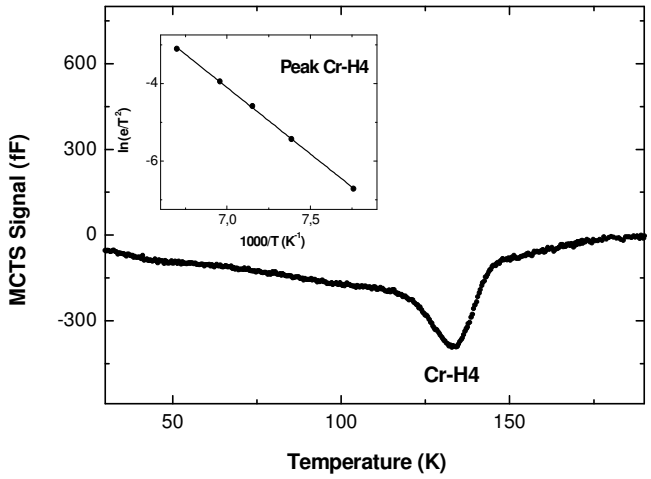

Fig.4.17. MCTS scan recorded in the Cr-diffused *n*-type Ge sample at -5V with optical pulse duration of 5 ms and rate window of 80 s^{-1}. The inset displays the Arrhenius plot of the level, labeled Cr-H4.

The investigation of the lower-part of Fe-contaminated Ge bandgap by MCTS analysis results in level Fe-H1, displayed on **Figure 4.18**. This typical MCTS spectrum shows a single line peaking around 140 K. Under the experimental conditions corresponding to this spectrum, the Arrhenius plot of Fe-H1 displayed in the inset, lead to the data reported in **Table 4.5**.

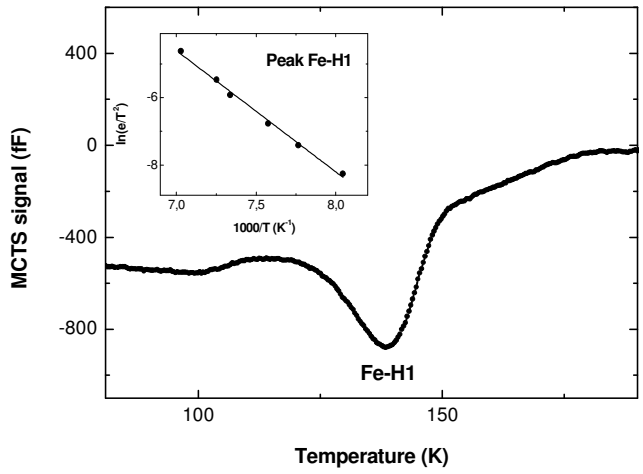

Fig.4.18. MCTS scan recorded in the Fe-diffused *n*-type Ge sample at -5V with optical pulse duration of 5 ms and rate window of 80 s^{-1}. The inset displays the Arrhenius plot of the hole trap Fe-H1.

Proceeding with similar conditions for Ni-diffused Ge leads to the MCTS scan shown in **Figure 4.19**, where a hole trap Ni-H1 is evidenced at about 140 K. The Arrhenius plot of carrier emission rate, displayed in the inset of this figure, allows the determination of the parameters presented in **Table 4.5**.

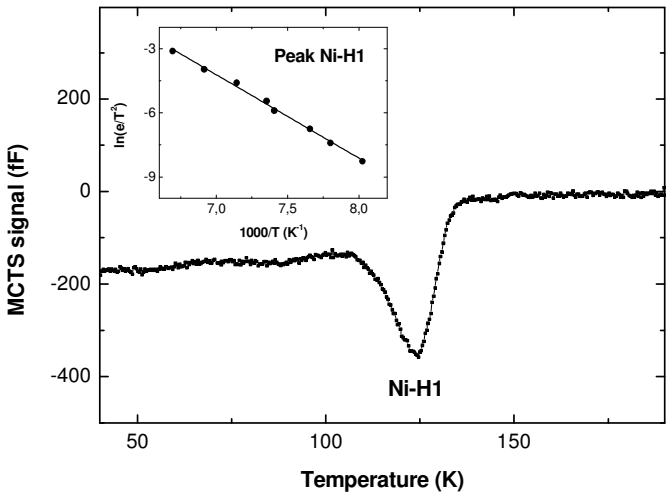

Fig.4.19. MCTS scan recorded in the Ni-diffused *n*-type Ge sample at -5V with optical pulse duration of 5 ms and rate window of 80 s^{-1}. The inset displays the Arrhenius plot of the hole trap Ni-H1.

Level label	K_T ($s^{-1}K^{-2}$)	E_{pa} (eV)	$\sigma_p \exp(\Delta S/k_B)$
Cr-H4	4.2×10^{8}	0.294±0.008	$(3.7\pm0.3)\times10^{-12}$
Fe-H1	2.8×10^{8}	0.310±0.008	$(3.3\pm0.3)\times10^{-12}$
Ni-H1	3.6×10^{9}	0.336±0.020	$(4.2\pm0.8)\times10^{-12}$

Table 4.5: The apparent activation energy E_p and the apparent capture cross sections $\sigma_p \exp(\Delta S/k_B)$ derived from Arrhenius diagram in MCTS spectrum of TM-diffused *n*-type Ge.

The necessity of annealing the n^+p diodes at 500 °C after implanting the metallic impurities seems to be harmful to the device characteristics. But surprisingly enough this was not the case for Ni-implanted n^+p diodes. The DLTS could thus be carried out as shown in **Figure 4.20**. The spectrum consists of one peak from majority carriers trap occurring at 205 K, labeled Ni-H1* there the star helps making a formal distinction between two identical hole traps, depicting the same defect seen by DLTS in n^+p-type material and by MCTS applied to the *n*-type Ge sample.

A trap concentration of 1.2×10^{13} cm^{-3} has been derived from **Figure 4.20**.

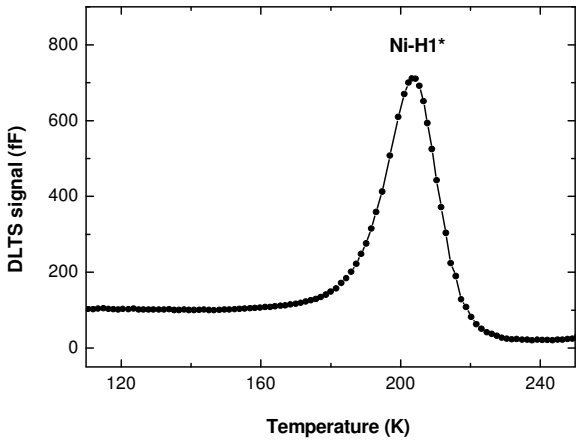

Fig.4.20. DLTS spectrum recorded in the Ni-diffused *p*-type Ge sample. The analytical parameters are: t_F = 200 µs, bias (−5V, −2V) and rate window of 100 s^{-1}.

The Laplace DLTS spectrum with its inset including the Arrhenius diagram of emission rate, corrected by the factor T^2, is shown in **Figure 4.21**. The corresponding values of the signature (K_T, E_p) according to the analog of **Equation 4.1** for holes and the apparent capture cross section σ_p are listed in **Table 4.6**.

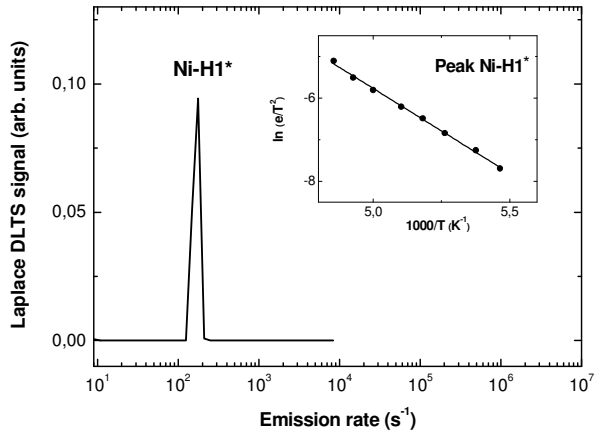

Fig.4.21. Laplace DLTS spectrum recorded in the Ni-diffused p-type Ge sample. The analytical parameters are: t_F = 200 µs, bias (−5V, −2V) and T = 200 K. The inset displays the Arrhenius plot of the hole trap Ni-H1*.

Level label	K_T ($s^{-1}K^{-2}$)	E_{pa} (eV)	σ_{pa} (cm^2)
Ni- H1*	2.4×10^{6}	0.354±0.006	$(2.1\pm0.4)\times10^{-15}$

Table 4.6: The activation enthalpy E_p, pre-exponential factor K_T and extrapolated capture cross sections σ_p derived from Arrhenius diagram in Laplace DLTS spectrum of Ni-diffused *p*-type Ge.

We believe that result obtained by Laplace DLTS method offering a higher resolution than conventional DLTS, leads to unambiguous results ever observed for Ni-implanted *p*-type Ge samples.

Typical MCTS spectra of Au-implanted *n*-type Ge are shown in **Figure 4.22** with the indicated experiment conditions. The spectra contain three strong bands at 30 K, labeled Au-E1, around 90 K, labeled Au-H2 and around 125 K, labeled Au-E2. **Figure 4.23** presents one MCTS spectrum of Au-implanted *n*-type Ge, recorded at constant reverse bias V_r = -5 V with laser diode pulse duration t_F = 5 ms and the rate window of 200 s^{-1}. The signatures (E_p, K_T) and the apparent capture cross sections $\sigma_p \exp(\Delta S/k_B)$ for detected levels were calculated from an Arrhenius plot, presented as inset in **Figure 4.23** and are given in **Table 4.7**.

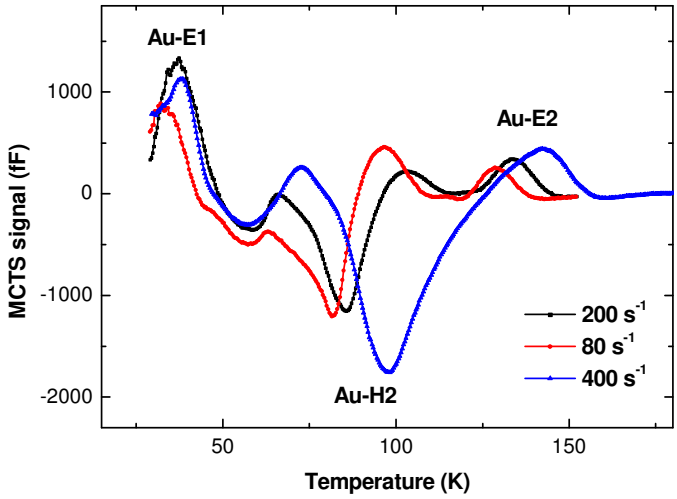

Fig. 4.22. MCTS scan recorded in the Au-diffused sample at -5V with an optical pulse duration of 5 ms and the indicated rate windows.

Level label	K_T ($s^{-1}K^{-2}$)	E_{pa} (eV)	$\sigma_p \exp(\Delta S/k_B)$
Au- E1	2.4×10^{3}	0.037±0.012	$(2.1\pm0.1)\times10^{-18}$
Au- H2	1.3×10^{7}	0.280±0.005	$(1.1\pm0.8)\times10^{-13}$
Au-E2	1.5×10^{5}	0.221±0.030	$(1.3\pm1.1)\times10^{-15}$

Table 4.7. The apparent activation energy for hole emission E_p, pre-exponential factor K_T and capture cross sections $\sigma_p exp(\Delta S/k_B)$ derived from Arrhenius plot of T^2-corrected emission rates determined from MCTS measurements for Au-diffused *n*-type Ge.

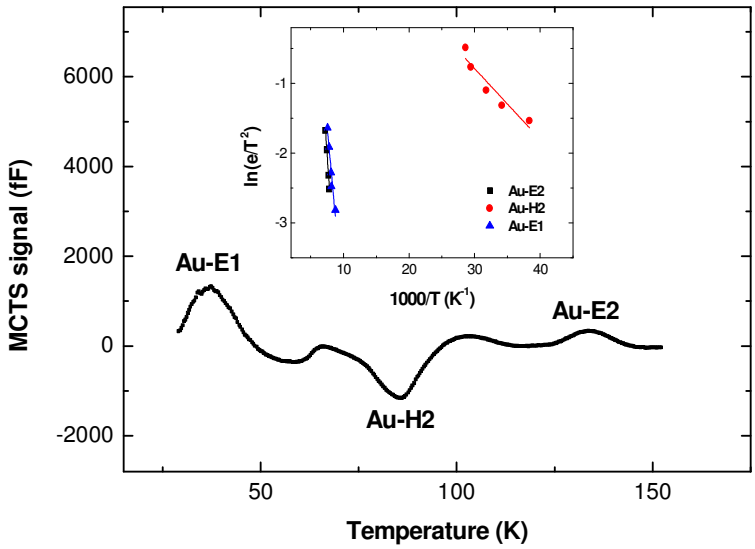

Fig. 4.23. MCTS scan recorded in the Au-diffused n-type Ge sample at -5V with an optical pulse duration of 5 ms and rate window of 200 s^{-1}.

As can be seen from **Figures 4.22 and 4.23**, two types of deep carrier traps are observed – both minority (Au-H2) and majority (Au-E1 and Au-E2) – in Schottky barrier on *n*-type Ge.

Basically, gold is an amphoteric defect with two coupled levels, i.e. a triple acceptor with an additional deep donor level. The case of the gold acceptor level is much more complicated, simply because it is a recombination-generation center, thus interacting with both the conduction and the valence bands. We cannot exclude the pinning of the acceptor level to the conduction band, thus the acceptor level $Au^{-/0}$, marked as Au-H2, being a midgap level, seem to interact simultaneously with both the conduction and valence band, which leads to presence of both electron and hole trap character in MCTS investigation [25]. As may be seen from **Table 4.7**, Au-E1 has value of $\sigma_p \exp(\Delta S/k_B)$ of about 10^{-18} cm^{-2}. This low value is typical for the repulsive center.

4.7. FIELD EFFECT

It is well known that an electric field lowers the barrier in traps with Coulomb-confinement potential as first discussed by Poole and Frenkel [26]. In the present work we have studied the effect of the electric field in the depletion region on the hole emission from the single acceptor states of Fe and Ni-doped n-type Ge (see **Figures 4.18** and **4.19**). It should be noticed that the assignment of a level, interacting with the valence band E_v and bearing an acceptor state, is expected to undergo the Poole-Frenkel effect which holds two opposite charges interacting. The coulombic interaction leads to a large extrapolated capture cross section given in **Table 4.5**. The same holds when probing a donor level interacting with the conduction band.

The consequence is that the enthalpy of ionization, extracted from an Arrhenius plot, depends on the external electric field, under which the hole-emission process takes place; the higher the electric field, the lower the barrier associated with the Coulombic potential, that the hole has to overcome to be emitted; thus the higher the emission rate is. This is the basic of the Poole-Frenkel effect, shown in **Figures 4.24** and **4.25** for Fe- and Ni-diffused *n*-type Ge samples, respectively, and is often used as a mean to check the charge state of a given level.

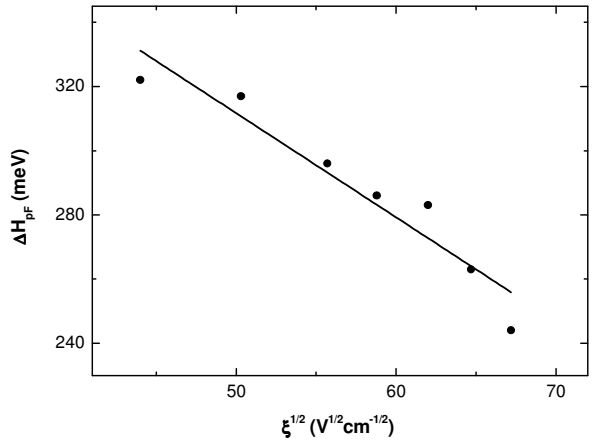

Fig.4.24. Poole-Frenkel effect observed in MCTS analysis of Fe-doped *n*-type Ge, showing the reduction of the enthalpy of ionization ΔH_{pF} as a function of $\xi^{1/2}$.

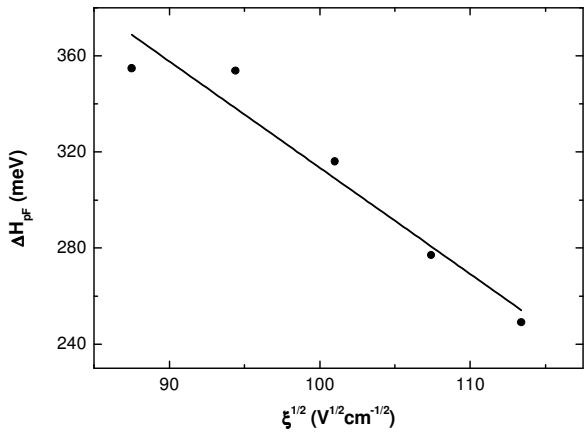

Fig.4.25. Poole-Frenkel effect observed in MCTS analysis of Ni-doped *p*-type Ge, showing the reduction of the enthalpy of ionization ΔH_{pF} as a function of $\xi^{1/2}$.

The predicted linear decrease of the enthalpy of ionization as a function of $\xi^{1/2}$ is clearly displayed, where ξ represents the maximum electric field strength [26] for a given reverse bias V_r. Taking into account this basic mechanism, the real ionization energy, which holds under zero bias, can be extracted by extrapolation to zero electric field. The extrapolated zero field activation energies ΔH_p for the Fe-H1 and Ni-H1 levels are listed in **Table 4.8**.

Level label	ΔE_{pa} (eV)	σ_{pa} (cm^2)	ΔH_p (eV)
Fe-H1	0.310±0.008	(3.3±0.3)×10^{-12}	0.374±0.010
Ni-H1	0.336±0.020	(4.2±0.8)×10^{-12}	0.378±0.013

Table 4.8: The apparent activation energy ΔE_p, capture cross sections σ_p and the final corrected value of ΔH_p at zero electric field.

In this chapter the field dependent emission signatures of the hole traps Fe-H1 and Ni-H1 investigated by MCTS method have been reported for the first time. The same result is expected for Cr-H3 level, presented in Figure 4.16, due to the mentioned peak shifting by applied field variation. Consequently levels Fe-H1 and Ni-H1 were attributed to the charge impurities, the candidates are Fe and Ni in single acceptor states due to the investigation presented previously.

4.8. DISCUSSION

The empirical correlation between the electronic configurations of a given transition metal and the type and number of energy levels introduced in Ge, known as *Watkins model* [27], but inferred earlier by *Woodbury* and *Tyler* [16] is found to be generally correct. The simple approach based on *s*-states occupancy, leads to the results displayed in **Figure 4.26**. The applicability of the tetrahedral bonding model constitutes evidence, that TM impurities are in substitutional sites in Ge lattice.

According to the model mentioned in **Chapter I**, Au ($6s^1$), Cr ($4s^1$), Ni ($4s^2$) and Fe ($4s^2$) - the four metals dealt with in the present work – give rise to the triple for the first two and to the double acceptor states, for the last two species, respectively. Our results and the thorough analysis carried out by *Clauws et al*. [1, 2, 4, 5, 8, 15] is in fairly good agreement with the model, with the exception that for gold and chromium a fourth donor level seems to merge next to the triple acceptor state.

In the Cr-doped samples four bands Cr-E1 and CrX-E (**Figures 4.2** and **4.6**), using DLTS and Laplace DLTS methods and Cr-H3 and Cr-H4 (**Figures 4.16** and **4.17**), using MCTS technique, are observed.

In **Figures 4.16** and **4.17** we can see a single line peaking above a continuum distribution of states. The reason for the existence of this continuum is found in the fact that light, being absorbed exponentially away from the surface, the whole depletion region, including the near surface region, is involved in the excitation. In the conventional DLTS method the mentioned near surface region can be avoided by appropriately selecting the height of the electric pulse. The continuum is often related to the surface states, which are difficult to avoid in Schottky barriers.

Before a DLTS-band with level Cr-E1 at $E_c - 0.364\ eV$ and levels Cr-H2 and Cr-H3 at $E_v + 0.046\ eV$ and $E_v + 0.088\ eV$ [1, 2, 5] were observed, using conventional DLTS technique. These levels are however rather different from the signatures in our study. The low temperature peak Cr-H3 can be observed only partly as shown in **Figure 4.16**. This peak displays a clear electric-field dependent shift but an accurate signature could not be determined, due to its position close to the freeze-out temperature. If we compare the signatures with energy levels attributed to Cr in previous publications, the hole trap, labelled as Cr-H4, located at 0.294 eV above E_v, is very different from the levels attributed earlier to this impurity. We attribute Cr-H4 to the double acceptor state of Cr defect. Taking into account the DLTS bands, which can appear due to the implantation damage, we are confident in their difference from the bands presented in this work. As was mentioned in **Chapter III**, damage related bands should be efficiently removed by the 500 °C anneal. Since for the present experiments an additional short etch was applied, it can be excluded that the presently observed bands could be due to damage effects.

In case of Fe three levels Fe-E1, FeX-E and Fe-H1 are observed (**Figures 4.1**, **4.5** and **4.18**). We attribute Fe-E1 and Fe-H1 to the same defect. If we compare the signatures with energy levels attributed to Fe in earlier publications, we can conclude that Fe-related levels reported here are different from the levels attributed earlier to this impurity.

In the Ni-doped samples three levels Ni-E1, Ni-H1 and NiX-E are observed; first two of them are considered as belonging to the same defect (**Figures 4.3**, **4.7** and **4.19**). The success in n^+p mesa diode preparation gives us possibility to investigate the lower part of the bandgap of *p*-type Ge doped by Ni using Laplace DLTS method at the first time. Observed hole trap labeled as Ni-H1* is presented in **Figure 4.20** with the corresponding signature listing in **Table 4.6**.

For mentioned previously metals the TM-E1 level corresponds with a low value of the electron capture cross section, which is thermally activated. This observation may be considered as an indication that we are concerned with multiphonon-assisted capture against a repulsive barrier, as would be the case for electron capture into a negative charge state of the defect [28]. These levels are attributed to the double acceptors so that electron capture occurs in the doubly negative charge states. The assignment to acceptor levels is supported by the absence of an electric field enhanced shift of the TM-E1 levels.

The capture cross section of the hole traps labeled TM-H1 could not be measured by the pulse length method, so that values are estimated to be in order of 10^{13} cm^2 or higher. Such high cross sections indicate that the holes are probably captured into negative charge state of the defects [28].

For Fe-H1 and Ni-H1 levels show a distinct electric field enhanced emission, which was observed for the first time. In **Figures 4.24** and **4.25** the field dependence of the apparent activation energy has been plotted according to a simple Poole-Frenkel model for attractive centers [26]. The lowering of the Coulomb barrier due to the field ξ is calculated and can be found in **Chapter 2.2.3**. In this work we have studied the effect of the electric field on the hole emission from the single acceptor states of Fe, Ni and Cr impurity atom in *n*-type Ge. The experimental results (**Figures 4.24** and **4.25**) indicate that Poole-Frenkel model can be considered as the mechanism for the electric-field-induced minority carrier emission from the single acceptor states of Fe and Ni centers in the range of electric fields from $2 \times 10^3\ V/cm$ to $1.3 \times 10^4\ V/cm$. Extrapolating of the apparent activation energy to zero field results in the corrected values of ΔH presented in **Table 4.8**. Observed field enhancement of the hole emission is a strong indication that peaks Fe-H1 and Ni-H1 are due to the states attractive for holes, i.e. the acceptor states, which is also in agreement with high values of the capture cross sections.

In this work a new insight is revealed on the microscopic behavior of the investigated chemical species through their unavoidable interactions with hydrogen giving rise to the generation of complex-related levels in the band gap. We suggest

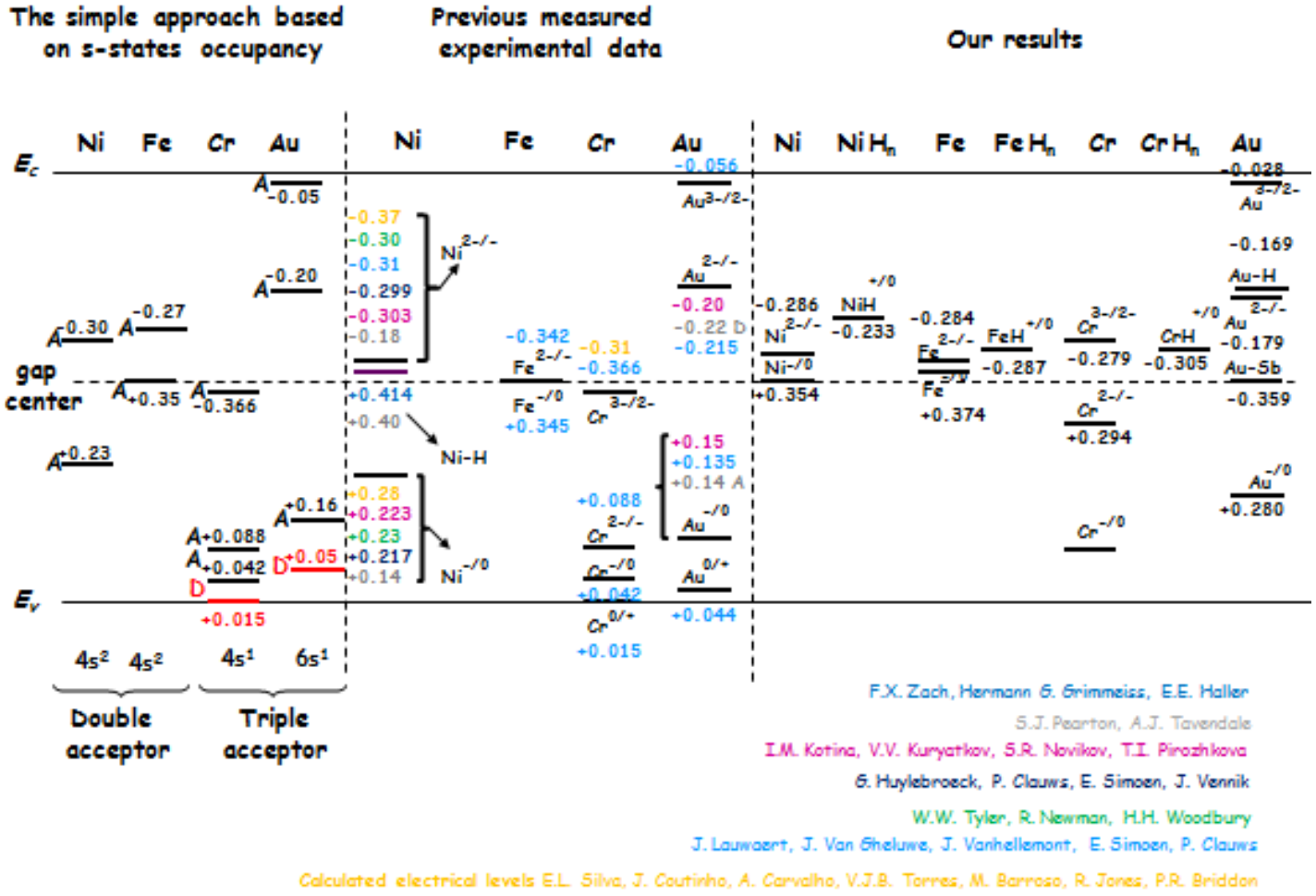

Fig. 4.26. Deep-level parameters and assignments of electron and hole traps in Fe-, Cr-, Ni- and Au-implanted Ge [1, 2, 6-8, 10, 15-17, 29-34].

the presence of complexes formed by Fe, Cr, Ni (peak TMX-E1 in DLTS and Laplace DLTS spectra) and Au (peak AuX-E2 in DLTS and Laplace DLTS spectra) impurities and hydrogen during the sample preparation. It is known that when hydrogen binds to multivalent acceptors in Ge, it acts as a positive ion by capturing a hole. When acting as a neutral impurity, hydrogen binds an extra electron becoming a negative ion [35]. We suggest that observed TM-H_n complexes are responsible for the donor action. Such donor levels should capture holes into neutral charge state and expected intermediate values for capture cross sections σ_n were found and presented in **Table 4.1**.

Among the impurities studied in this work whose parameters are displayed in **Figure 4.26**, Ni and Fe offer and interesting feature. Below we consider the case of Fe, but the same reasoning can be applied to Ni as well. The striking feature is the tiny separation between the two Fe-related levels $Fe^{2-/-}$ and $Fe^{-/0}$.

As mentioned above, also called Positive-U system so far the distribution of the various charge states for a given metallic impurity is normal. In other words, as we move from the conduction band E_c toward the valence band E_v the charge state goes from the most negative to the less negative. But in many circumstances this distribution may be inverted -Negative-U system.

In the case of Fe for instance, this would correspond to the single acceptor level being closer to the conduction band. It does not seem to be the case here but the levels are so close that depending on their pinning mechanism to the band edges, the distribution might be inverted at some higher temperature. This would definitely happen at some critical temperature if each level is pinned to its respective band. This critical temperature can be estimated by the following considerations. Firstly, we assume that the double acceptor state is pinned to the conduction band, that is $\Delta H_n\left(Fe^{2-/-}\right) = 0.327 - \Delta E_\sigma = 0.284\ eV$. It follows that its position relative to the valence band is given by

$$\Delta H_p\left(Fe^{2-/-}\right)(T) = E_g(T) - \Delta H_n\left(Fe^{2-/-}\right), \tag{4.2}$$

where $E_g(T)$ is specified by **Equation 1.1** in **Chapter 1**.

Now, accordingly we assume that the single acceptor state is pinned to the valence band, thus keeping $\Delta H_p\left(Fe^{0/-}\right) = 0.374\ eV$ independent of the temperature. Then, the critical temperature T_c at which the system of the two levels switches to Negative-U is given by the equality

$$\Delta H_p\left(Fe^{-/0}\right) = \Delta H_p\left(Fe^{2-/-}\right)(T) \tag{4.3}$$

or

$$\Delta H_p\left(Fe^{-/0}\right) = E_g(T) - \Delta H_n\left(Fe^{2-/-}\right), \quad (4.4)$$

where $\Delta H_p\left(Fe^{-/0}\right) = 0.374\ eV$ and $\Delta H_n\left(Fe^{2-/-}\right) = 0.284\ eV$. Using the data above we find a critical temperature of T_c = 308 K. At this temperature and above, the intermediate negative charge state does no longer exist and the charge state of the defect flips directly from -2 to 0. It would be challenging to find a way of checking this property.

In case of Au the situation is far from to be clear. Basically, gold is an amphoteric defect with two coupled levels, i.e. a triple acceptor with an additional deep donor level. The main bands Au-E1, Au-E2 (**Figures 4.4**, **4.8** and **4.9**) and Au-H2 (**Figures 4.22 and 4.23**) belong to substitutional gold. Other observed levels seem to be produced by possible interaction of gold with other impurities forming the complexes with H, appearing as a shoulder in Au-E2 peak family, and with shallow Sb, appearing around 165 K in DLTS and Laplace DLTS measurements, labeled AuX-E2 and AuX-E1, respectively. These levels seem to be uncorrelated with the main Au-related levels. Speaking of permanently observed AuX-E1 level, we should mention the band, which has already been observed and referred in the literature, attributed to the $Cu_s^{(3-/2-)}$ [11]. But large capture cross section of AuX-E1 reject the possible presence of a repulsive center such as Cu_s is. We tentatively suggest the possible interaction of gold with shallow antimony (Sb), which being a donor in our wafers can form a complex with Au by Coulombic interaction. This point is deserving consideration in a further work.

The deep level parameters for all bands have been determined carefully and are summarized previously. The activation enthalpies for Au-E1 and Au-E2 levels are in fair agreement with previously reported DLTS results [7, 15]. For these levels the temperature dependence of the capture cross section was established, resulting in the correcting of magnitudes of apparent activation enthalpy of ionization summarized in **Table 4.3**. The extracted barriers for capture E_σ represent an acceptor character of observed traps. The directly determined values of capture cross section σ_∞ are considered to be more accurate.

As can be seen from **Figures 4.22 and 4.23**, in MCTS investigation two types of deep carrier traps can be observed – both minority (Au-H2) and majority (Au-E1 and Au-E2). This unusual phenomenon might be explained if we assume the gold acceptor level as a recombination-generation center, interacting with both the conduction and the valence bands. We cannot exclude the pinning of the acceptor level to the conduction band, thus the acceptor level $Au^{-/0}$, marked as Au-H2, being a midgap level, seem to interact simultaneously with both the conduction and valence band, which leads to presence of both electron and hole trap character in MCTS investigation [25].

Bibliography

1. Clauws, P., et al., *Deep level transient spectroscopy of transition metal impurities in germanium.* Physica B: Condensed Matter, 2007. **401-402**(0): p. 188-191.
2. Lauwaert, J., et al., *Electronic properties of titanium and chromium impurity centers in germanium.* Journal of Applied Physics, 2009. **105**(7): p. 073707-6.
3. Lauwaert, J., J. Van Gheluwe, and P. Clauws, *An accurate analytical approximation to the capacitance transient amplitude in deep level transient spectroscopy for fitting carrier capture data.* Review of Scientific Instruments, 2008. **79**(9): p. 093902-4.
4. Lauwaert, J. and P. Clauws, *Majority carrier capture rates for transition metal impurities in germanium.* Thin Solid Films, 2010. **518**(9): p. 2330-2333.
5. Clauws, P. and J. Lauwaert, *Electronic Properties of Transition Metal related Defects in Germanium*, in *The 5th International Symposium on Advanced Science and Technology of Silicon Materials (JSPS Si Symposium)*. 2008: Kona, Hawa.
6. Simoen, E. and C. Claeys, *Chapter 5 - Metals in germanium*, in *Germanium-Based Technologies*. 2007, Elsevier: Oxford. p. 131-185.
7. Simoen, E., et al., *DLTS of gold impurities in germanium.* Semiconductor Science and Technology, 1987. **2**(8): p. 507.
8. Huylebroeck, G., et al., *DLTS of nickel impurities in germanium.* Solid State Communications, 1992. **82**(5): p. 367-369.
9. Markevich, V.P., et al., *Electronic properties of antimony-vacancy complex in Ge crystals.* Journal of Applied Physics, 2004. **95**(8): p. 4078-4083.
10. Kotina, I.M., et al., *Capacitance spectroscopy of deep Cu, Au, Ag, and Ni centers in germanium.* Soviet physics semiconductors, 1987. **21**(6): p. 635.
11. Simoen, E., et al., *Signature and capture cross section of copper-related hole traps in p-type high-purity germanium.* Semiconductor Science and Technology, 1986. **1**(1): p. 55-57.
12. Markevich, V.P., et al., *Vacancy-group-V-impurity atom pairs in Ge crystals doped with P, As, Sb, and Bi.* Physical Review B, 2004. **70**(23): p. 235213.
13. Markevich, A.V., et al., *Phonon-assisted changes in charge states of deep level defects in germanium.* Physica B: Condensed Matter, 2006. **376–377**(0): p. 61-65.
14. Henry, C.H. and D.V. Lang, *Nonradiative capture and recombination by multiphonon emission in GaAs and GaP.* Physical Review B, 1977. **15**(2): p. 989-1016.
15. Clauws, P. and E. Simoen, *Metals in germanium.* Materials Science in Semiconductor Processing, 2006. **9**(4-5): p. 546-553.
16. Woodbury, H.H. and W.W. Tyler, *Triple Acceptors in Germanium.* Physical Review, 1957. **105**(1): p. 84-92.
17. Forment, S., et al., *A deep-level transient spectroscopy study of transition metals in n-type germanium.* Materials Science in Semiconductor Processing, 2006. **9**(4-5): p. 559-563.

18. Pankove, J.I. and N.M. Johnson, *Chapter 1 Introduction to Hydrogen in Semiconductors*, in *Semiconductors and Semimetals*, I.P. Jacques and M.J. Noble, Editors. 1991, Elsevier. p. 1-15.

19. Feklisova, O.V., et al., *Dissociation of iron-related centers in Si stimulated by hydrogen.* Materials Science and Engineering: B, 2000. **71**(1–3): p. 268-271.

20. Sadoh, T., et al., *Deep levels of chromium-hydrogen complexes in silicon.* Journal of Applied Physics, 1994. **75**(8): p. 3978-3981.

21. Dobaczewski, L., et al., *Donor level of bond-center hydrogen in germanium.* Physical Review B, 2004. **69**(24): p. 245207.

22. Bollmann, J., et al., *Hydrogen ion drift in Sb-doped Ge Schottky diodes.* Physica B: Condensed Matter, 2009. **404**(23–24): p. 5099-5101.

23. Sachse, J.U., J. Weber, and H. Lemke, *Deep-level transient spectroscopy of Pd-H complexes in silicon.* Physical Review B, 2000. **61**(3): p. 1924-1934.

24. Hamilton, B., A.R. Peaker, and D.R. Wight, *Deep-state-controlled minority-carrier lifetime in n-type gallium phosphide.* Journal of Applied Physics, 1979. **50**(10): p. 6373-6385.

25. Mesli, A., P. Kringhøj, and A. Nylandsted Larsen, *Pinning behavior of gold-related levels in Si using Si_{1-x}Ge_{x} alloy layers.* Physical Review B, 1997. **56**(20): p. 13202-13217.

26. Frenkel, J., *On Pre-Breakdown Phenomena in Insulators and Electronic Semi-Conductors.* Physical Review, 1938. **54**(8): p. 647-648.

27. Continenza, A., G. Profeta, and S. Picozzi, *Transition metal impurities in Ge: Chemical trends and codoping studied by electronic structure calculations.* Physical Review B, 2006. **73**(3): p. 035212.

28. Milnes, A.G., *Deep impurities in semiconductors*. 1973, New York: Wiley.

29. Zach, F.X., Hermann G. Grimmeiss, and E.E. Haller, *Nickel Related Deep Levels in Germanium.* Materials Science Forum (Volumes 83 - 87), 1992. **Defects in Semiconductors 16**: p. 245-250.

30. S.J, P., *Deep metal-related centres in germanium.* Solid-State Electronics, 1982. **25**(4): p. 305-311.

31. S.J, P., *A study of deep metal-related centres in germanium by capacitance spectroscopy.* Solid-State Electronics, 1982. **25**(6): p. 499-503.

32. Tyler, W.W., *Deep level impurities in germanium.* Journal of Physics and Chemistry of Solids, 1959. **8**(0): p. 59-65.

33. Tyler, W.W., R. Newman, and H.H. Woodbury, *Properties of Germanium Doped with Nickel.* Physical Review, 1955. **98**(2): p. 461-465.

34. Silva, E.L., et al., *Electronic structure of Zn, Cu and Ni impurities in germanium.* Journal of Physics: Condensed Matter, 2011. **23**(6): p. 065802.

35. Weber, J., M. Hiller, and E.V. Lavrov, *Hydrogen in germanium.* Materials Science in Semiconductor Processing, 2006. **9**(4–5): p. 564-570.

CONCLUSIONS AND PERSPECTIVES

The study of TM impurities in Ge is an example of device-driven basic research. Due to the dominant technological importance of Si, defect research shifted to this host material. The renewed interest in high-mobility Ge layers brings back this material into the focus of actual research. Electronic properties of metallic species are very different in Ge and Si. The collected data in germanium are by far much less complete than in silicon, and still exhibit some scattering.

This work is an attempt to examine some peculiar features related to metallic species of Fe, Cr, Ni and Au in *n*-type germanium studied, using conventional and Laplace DLTS techniques. Schottky barriers usage restricts the studies to levels located in the upper half of the band gap. In **Chapter IV** a study of the electronic properties of Fe, Ni, Au and Cr in *n*-type Ge as well as Ni in *p*-type Ge was presented.

The n^+p junctions, which turned out to be very helpful in studying irradiation induced hole traps located in the lower half of the bandgap, turned out to be inefficient in the present study. The necessity of annealing the samples at 500 °C after implanting the metallic impurities seems to be harmful to the device characteristics. Only the case of Ni-doped n^+p mesa diode preparation turned out to be prosperous. This gives us possibility to characterize minority carrier trap by means of high sensitive Laplace DLTS method for the first time. However, by applying external optical excitation to generate minority carriers the investigation is extended to the lower half of the band gap.

Major findings already published by other authors are in several cases confirmed. A summary of the deep level parameters obtained in this work is given in **Table S.1**. Based on these data the effect of different metals on the minority carrier lifetime may be calculated.

However, new insight is revealed on the microscopic behavior of these four chemical species such as their interactions with hydrogen giving rise to the generation of complex-related levels in the band gap. **Table S.2** reports first of the activation enthalpy E_{na}, pre-exponential factor K_T and extrapolated capture cross sections σ_{na} derived from Arrhenius diagram in Laplace DLTS spectrum of Cr-contaminated *n*-type Ge samples before and after a significant annealing, following a dip during 2 min in nitric acid. We believe that described in **Chapter 4.5** procedure and results demonstrate the interactions of mentioned impurity with hydrogen, giving rise to the generation of complex-related levels in the band gap.

In case of Au new levels attributed to conjectural AuH_n and AuSb complexes are observed. In addition development of both majority and minority carriers in MCTS analysis is still under consideration.

Level label	K_T ($s^{-1}K^{-2}$)	ΔE_n(eV)	$\sigma_{na/pa}$ (cm²)	σ_∞ (cm²)	E_σ(eV)	$\Delta S_n/k_B$	ΔH_n(eV)
Fe-E1	7.1×10^{6}	0.327±0.002	$(2.3\pm0.4)\times10^{-16}$	$(4.98\pm0.39)\times10^{-15}$	0.043	3.08	0.284
Cr-E1	4.2×10^{6}	0.325±0.005	$(1.4\pm0.5)\times10^{-16}$	$(4.59\pm0.36)\times10^{-15}$	0.046	3.49	0.279
Ni-E1	5.5×10^{6}	0.321±0.005	$(1.8\pm0.6)\times10^{-16}$	$(4.09\pm0.32)\times10^{-15}$	0.035	3.12	0.286
Au-E1	3.3×10^{5}	0.047±0.002	$(1.1\pm0.9)\times10^{-17}$	$(3.37\pm0.54)\times10^{-14}$	0.019	8.03	0.028
Au-E2	1.3×10^{6}	0.212±0.001	$(4.2\pm1.6)\times10^{-15}$	$(2.99\pm0.34)\times10^{-13}$	0.033	4.27	0.179
CrX-E	1.5×10^{7}	0.305±0.002	$(4.7\pm0.7)\times10^{-16}$				
FeX-E	4.1×10^{6}	0.287±0.006	$(1.3\pm0.6)\times10^{-16}$				
NiX-E	1.4×10^{5}	0.233±0.009	$(1.2\pm2.2)\times10^{-17}$				
AuX-E1	3.1×10^{8}	0.359±0.006	$(1.0\pm0.5)\times10^{-14}$				
AuX-E2	6.5×10^{5}	0.169±0.004	$(2.1\pm0.6)\times10^{-17}$				
Ni- H1*	2.4×10^{6}	0.354±0.006	$(2.1\pm0.4)\times10^{-15}$				
Cr-H4	4.2×10^{8}	0.294±0.008	$(3.7\pm0.3)\times10^{-12}$				
Fe-H1	2.8×10^{8}	0.310±0.008	$(3.3\pm0.3)\times10^{-12}$				0.374
Ni-H1	3.6×10^{9}	0.336±0.020	$(4.2\pm0.8)\times10^{-12}$				0.378
Au- H2	1.3×10^{7}	0.280±0.005	$(1.1\pm0.8)\times10^{-13}$				

Table S.1: Overview of deep-level parameters obtained in this work for TM impurity traps in Ge.

Level label	K_T ($s^{-1}K^{-2}$)	E_T (eV)	σ_{na} (cm²)
Cr-E1 (annealed)	1.1×10^{7}	0.336±0.002	$(3.6\pm0.2)\times10^{-14}$
CrX-E1 (not annealed)	4.1×10^{8}	0.350±0.010	$(1.3\pm1.0)\times10^{-14}$
Cr-E1 (not annealed)	1.1×10^{7}	0.337±0.007	$(3.6\pm0.5)\times10^{-14}$

Table S.2: The signatures (E_{na}, K_T) and extrapolated capture cross sections σ_{na} derived from Arrhenius diagram in Laplace DLTS spectrum of Cr-contaminated *n*-type Ge, demonstrating the hydrogen presence.

For the Fe case, the small difference in energy of its two levels raises the question of the possibility of *negative-U* character. The single and double acceptors induced by Fe being very close to each other raises the legitimate and challenging question of their ordering at about room temperature, with a possible inversion if they are both pinned to their respective allowed bands. These mentioned points should be treated more thoroughly in a future work.

APPENDIX 1

The usual method to study the carrier capture rate using standard capacitance DLTS or Laplace DLTS consists on a record of the amplitude as a function of filling pulse duration. This procedure is described below.

As mentioned previously (see **Chapter II**, **Section 2.1**) a defect requiring less carriers injection times – shorter voltage pulses – to saturate, has a large capture cross section.

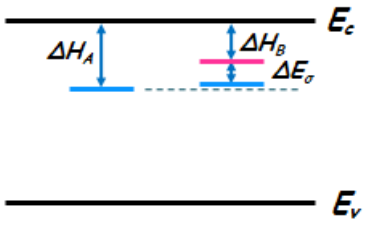

Fig. A.1. Energy levels and energy barrier in semiconductor bandgap.

If we consider a deep level with an enthalpy ΔH_B and a barrier for capture ΔE_σ, the emmision rate can be written as

$$e_B = CT^2 \sigma_{B\infty} \exp\left(\frac{\Delta S_B}{k}\right) \exp\left(-\frac{\Delta H_B + \Delta E_\sigma}{kT}\right), \tag{A.1}$$

where the capture cross section and the relation between the energies can be written as

$$\begin{cases} \Delta H = \Delta H_B + \Delta E_\sigma \\ \sigma_B = \sigma_{B\infty}\left(-\frac{\Delta E_\sigma}{kT}\right) \end{cases} \tag{A.2}$$

We determine the barrier for capture ΔE_σ from the dependence between the pulse width and the height of Laplace DLTS peak

$$h(t_F) = h_\infty[1 - \exp(-\sigma_B n \langle v_n \rangle t_F)], \tag{A.3}$$

where t_F is the voltage pulse width, h – height of Laplace DLTS peak, n – doping concentration and $\langle v_n \rangle$ is the average thermal velocity of carriers.

Equation A.3 can be modified as

$$log\left[1 - \frac{h_{t_F}}{h_\infty}\right] = -\frac{\sigma_B n \langle v_n \rangle t_F}{ln10}. \tag{A.4}$$

A plot of the left part of this equation as a function of t_F allows getting the capture cross section easily. Such plot is shown in **Figure A.2**.

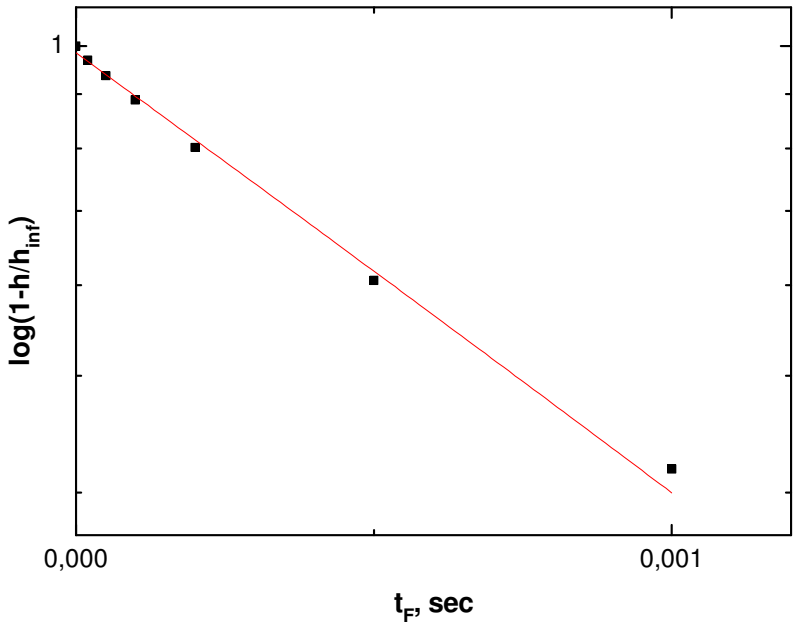

Fig. A.2. Experimental data and fitting of *(1-h/h∞)* as a function of t_F for Ni-diffused *n*-type Ge sample at 164 K.

The slope of the linear part is given by

$$slope = \left(-\frac{\sigma_n n \langle v_n \rangle}{ln10}\right), \tag{A.5}$$

which might be temperature dependent via the possible temperature of the capture cross section but also via the temperature dependence of thermal velocity given by

$$\langle v_n \rangle = \sqrt{\frac{3kT}{m^*}} = 0.9 \times 10^4 \sqrt{T}. \tag{A.6}$$

n can be found from CV-profile as doping concentration. In our case $n = 2\times10^{14}$ cm^{-3}. Substituting all these parameters in **Equation A.5** allows extracting capture cross section at different temperatures were obtained.

As a last step of the procedure we plot the capture cross section as a function of the temperature as shown in **Figure A.3** in the case of Ni, from which we extracted the data displayed in **Table 4.3**.

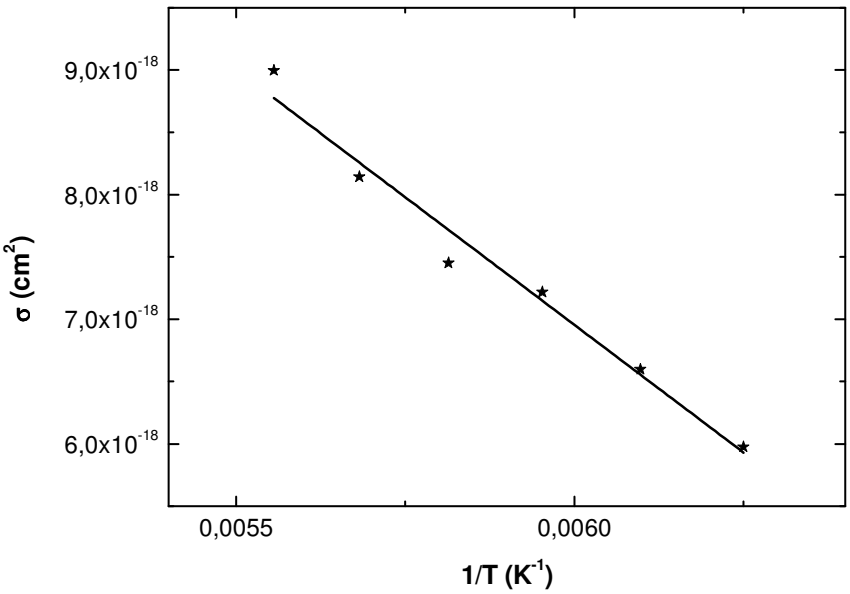

Fig. A.3. The temperature-dependent capture cross sections of Ni-diffused *n*-type Ge.